

# **Development of Surface Wave Dispersion and Attenuation Maps and Improved Methods for Measuring Surface Waves**

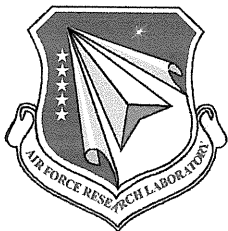
**Jeffry L. Stevens  
Heming Xu  
Jeffrey W. Given  
G. Eli Baker**

**Science Applications International Corporation  
10260 Campus Point Drive  
San Diego, CA 92121**

**Final Report**

**30 May 2008**

|   |
|---|
| <b>APPROVED FOR PUBLIC RELEASE; DISTRIBUTION UNLIMITED.</b> |
|---|



**AIR FORCE RESEARCH LABORATORY  
Space Vehicles Directorate  
29 Randolph Road  
AIR FORCE MATERIEL COMMAND  
Hanscom AFB, MA 01731-3010**

---

## NOTICE AND SIGNATURE PAGE

Using Government drawings, specifications, or other data included in this document for any purpose other than Government procurement does not in any way obligate the U.S. Government. The fact that the Government formulated or supplied the drawings, specifications, or other data does not license the holder or any other person or corporation; or convey any rights or permission to manufacture, use, or sell any patented invention that may relate to them.

This report was cleared for public release and is available to the general public, including foreign nationals. Qualified requestors may obtain additional copies from the Defense Technical Information Center (DTIC) (<http://www.dtic.mil>). All others should apply to the National Technical Information Service.

AFRL-RV-HA-TR-2008-1106 HAS BEEN REVIEWED AND IS APPROVED FOR  
PUBLICATION IN ACCORDANCE WITH ASSIGNED DISTRIBUTION STATEMENT.

//Signature//

---

ROBERT RAISTRICK  
Contract Manager

//Signature//

---

PAUL TRACY, Acting Chief  
Battlespace Surveillance Innovation Center

This report is published in the interest of scientific and technical information exchange, and its publication does not constitute the Government's approval or disapproval of its ideas or findings.

**REPORT DOCUMENTATION PAGE**Form Approved  
OMB No. 0704-0188

Public reporting burden for this collection of information is estimated to average 1 hour per response, including the time for reviewing instructions, searching existing data sources, gathering and maintaining the data needed, and completing and reviewing this collection of information. Send comments regarding this burden estimate or any other aspect of this collection of information, including suggestions for reducing this burden to Department of Defense, Washington Headquarters Services, Directorate for Information Operations and Reports (0704-0188), 1215 Jefferson Davis Highway, Suite 1204, Arlington, VA 22202-4302. Respondents should be aware that notwithstanding any other provision of law, no person shall be subject to any penalty for failing to comply with a collection of information if it does not display a currently valid OMB control number. **PLEASE DO NOT RETURN YOUR FORM TO THE ABOVE ADDRESS.**

**1. REPORT DATE (DD-MM-YYYY)**

30-05-2008

**2. REPORT TYPE**

Final Report

**3. DATES COVERED (From - To)**

20-04-2005 to 30-04-2008

**4. TITLE AND SUBTITLE**Development of Surface Wave Dispersion and Attenuation Maps  
Improved Methods for Measuring Surface Waves**5a. CONTRACT NUMBER**

FA8718-05-C-0023

**5b. GRANT NUMBER****5c. PROGRAM ELEMENT NUMBER**

62601F

**6. AUTHOR(S)**Jeffrey L. Stevens, Heming Xu, Jeffrey W. Given and  
G. Eli Baker**5d. PROJECT NUMBER**

1010

**5e. TASK NUMBER**

SM

**5f. WORK UNIT NUMBER**

A1

**7. PERFORMING ORGANIZATION NAME(S) AND ADDRESS(ES)**Science Applications International Corporation  
10260 Campus Point Drive  
San Diego, CA 92121**8. PERFORMING ORGANIZATION REPORT NUMBER****9. SPONSORING / MONITORING AGENCY NAME(S) AND ADDRESS(ES)**Air Force Research Laboratory  
29 Randolph Rd.  
Hanscom AFB, MA 01731-3010**10. SPONSOR/MONITOR'S ACRONYM(S)**

AFRL/RVBYE

**11. SPONSOR/MONITOR'S REPORT NUMBER(S)**

AFRL-RV-HA-TR-2008-1106

**12. DISTRIBUTION / AVAILABILITY STATEMENT**

Approved for Public Release; Distribution Unlimited.

**13. SUPPLEMENTARY NOTES****14. ABSTRACT**

The objective of this project is to optimize surface wave measurements, particularly at regional and local distances, and over the high frequency period band of 8-15 seconds. There are three main parts to this study: 1) We collect and then invert Eurasian surface wave amplitude data for attenuation and Q structure; 2) we develop amplitude corrections using the Born approximation and then compare them with observations and with the results of finite difference calculations; 3) we develop a time domain path corrected surface wave magnitude and compare it with other surface wave magnitudes. In addition, we analyze the surface waves from the North Korean nuclear test of October 9, 2006. The path corrected surface wave magnitude is similar to the Butterworth filtered magnitude developed by Russell, but regionalized to take into account variations in earth structure and attenuation. We conclude that the Born approximation is of marginal value for attenuation studies because it is a small perturbation approximation and the observed amplitude variations are too large and complicated to be predicted by the Born approximation. We find that the average surface wave Q of Eurasia is lower than our previous background model, particularly along a band running through the Middle East. We develop attenuation maps that predict attenuation along any path in Eurasia for frequencies below 0.15 Hz for distribution to AFRL, the DOE Knowledge Base and other researchers.

**15. SUBJECT TERMS**

Nuclear explosion, Surface wave, Surface wave magnitude, Attenuation

**16. SECURITY CLASSIFICATION OF:****a. REPORT**  
U**b. ABSTRACT**  
U**c. THIS PAGE**  
U**17. LIMITATION OF ABSTRACT**

SAR

**18. NUMBER OF PAGES**

63

**19a. NAME OF RESPONSIBLE PERSON**  
Robert Raistrick**19b. TELEPHONE NUMBER (include area code)**  
781-377-3726



## Table of Contents

|  |    |
|--|----|
| 1.0 Introduction and Summary .....   | 1  |
| 1.1 Attenuation.....   | 1  |
| 1.2 Born approximation .....   | 2  |
| 1.3 Path corrected magnitude.....  | 2  |
| 1.4 Korea.....   | 3  |
| 1.5 Recommendations.....   | 4  |
| 2.0 Path Corrected and Frequency Dependent Surface Wave Magnitudes .....                           | 5  |
| 2.1 Comparison of Butterworth filtered and regionalized surface wave magnitudes .....              | 5  |
| 2.2 Analysis of surface waves from the North Korean nuclear test.....                              | 9  |
| 2.3 Yield estimation, earthquake/explosion discrimination and the North Korean test .....          | 14 |
| 3.0 Amplitude Corrections Using the Born Approximation.....  | 18 |
| 3.1 Surface wave amplitude predictability.....   | 18 |
| 3.2 Surface wave propagation in simple structures .....  | 19 |
| 3.3 Surface wave propagation in complex structures .....   | 19 |
| 3.4 Application of corrections to surface wave amplitudes.....                                     | 21 |
| 3.4 Analysis of surface waves at KNET propagating through and near the Tarim<br>Basin .....        | 24 |
| 3.5 Analysis of surface waves at KNET stations due to Lop Nor explosions .....                     | 26 |
| 3.6. 3D Calculations of Lop Nor to KNET and comparison with the Born<br>approximation .....        | 28 |
| 4.0 Inversion for Earth Structure and Attenuation.....   | 31 |
| 4.1 The inversion procedure for a 3D earth model .....   | 31 |
| 4.2 Correction for scattering and diffraction due to a realistic heterogeneous earth<br>model..... | 31 |
| 4.3 Application of corrections to inversion for earth structure.....                               | 32 |
| 4.4 Inversion of attenuation data for Q structure .....  | 32 |
| 4.5 Data used in the Q Inversion.....  | 34 |
| 4.6 Q Inversion Results.....   | 35 |
| 5.0 Conclusions and Recommendations .....  | 45 |
| 6.0 Data Deliverable .....   | 47 |
| 7.0 Acknowledgment .....   | 47 |
| 8.0 References.....  | 48 |
| Appendix A. Events processed for Q inversion.....  | 50 |



## List of Figures

|   |    |
|---|----|
| Figure 1.1. Attenuation coefficients at 10 seconds period in Eurasia derived by inversion of surface wave amplitude measurements (left), average data and average data fit (right). Blue curve shows the inversion results, the red curve the average of the data, and the green line the starting model, averaged over all paths longer than 5000 km. Dashed lines show one standard deviation above and below each curve.....   | 1  |
| Figure 1.2. Comparison of Born approximation (left) with finite difference calculation (right) of amplitude perturbations at 10 seconds. The rectangular inclusion is modeled after the Tarim Basin structure, and the external structure after a Eurasian shield earth structure. The source is on the horizontal axis at the right edge of the plot. The amplitude is increased in a band above and to the left of the inclusion in both cases, and decreased above that. However, there are some interference effects in the finite difference calculation that are not reproduced in the Born calculation. .... | 2  |
| Figure 1.3. Path corrected surface wave magnitudes for the North Korean nuclear test, and fit to three $M_s$ :Yield curves for an estimated yield of 1 kiloton, together with historical $M_s$ :Yield data. ....  | 4  |
| Figure 2.1 Left: Mean $\log(S1*S2)$ and $\pm 1$ standard deviation (blue). Red line shows the Russell approximation for the source function. Right: Mean attenuation and $\pm 1$ standard deviation (blue) derived from earth models, Russell approximation for attenuation (red), and Rezapour and Pearce global estimate at 20 seconds (black). In both, green marks show values for individual Eurasian structures. ....   | 8  |
| Figure 2.2. 20 second magnitude correction vs. distance for Rezapour/Pearce (dashed blue), $M_{s(b)}$ (dot-dash black), $M_{s(bp)}$ with model-based gamma (solid red), and $M_{s(bp)}$ with Rezapour and Pearce gamma (solid maroon) (left). 10 second magnitude correction vs. distance $M_{s(b)}$ (dot-dash black), and $M_{s(bp)}$ with model-based gamma (solid red) (right). ....   | 8  |
| Figure 2.3. Location of the North Korean nuclear test and recording stations. ....  | 9  |
| Figure 2.4. Data from the North Korean explosion filtered from 0.01-0.1 Hz. Surface waves are clearly visible at all stations. HIA has a glitch or interfering arrival after the explosion arrival. The explosion arrival is visible just after the BJT arrival. ....   | 10 |
| Figure 2.5. Path corrections for the 7 stations that recorded surface waves from the North Korean nuclear test using model based corrections (left) and differences between the model-based and Russell path corrections for the 7 stations recording the North Korean event.....   | 10 |
| Figure 2.6. Calculation of path-corrected Butterworth filtered magnitude for 6 filter widths (left) at station BJT. Butterworth filtered, path corrected, and spectral magnitudes at BJT (right). ....  | 11 |
| Figure 2.7. Butterworth filtered (left) and path corrected (right) magnitudes for the North Korean nuclear test with varying filter widths. ....  | 11 |
| Figure 2.8. Amplitude corrections due to structure predicted using the Born approximation.....  | 12 |
| Figure 2.9. Path corrected spectra for an explosion and for earthquakes calculated for several depths. The path corrected explosion spectrum is flat over the entire frequency band (for perfect data and path correction), while the path corrected earthquake spectrum is flattened, but has some variation due to source mechanism and source depth and generally decreases with increasing frequency. ....  | 14 |

|   |    |
|---|----|
| Figure 2.10. $M_s$ : $m_b$ curves for Mueller Murphy granite using formulas from Stevens and Day (1985) and with 0.4 mb bias correction. Data from Stevens and Murphy (2001), plus the North Korea data point.....  | 15 |
| Figure 2.11. $m_b$ :yield curves for Mueller Murphy granite at normal containment depth and at 800 m depth using formulas from Stevens and Day (1985), and nominal Eurasian $m_b$ :yield curve (Murphy, 1996). Data from Stevens and Murphy (2001), plus North Korea $m_b$ and yield estimate. ....   | 16 |
| Figure 2.12. $M_s$ :yield curves for Mueller Murphy granite using formulas from Stevens and Day (1985) for normal containment depth and 800 meter depth, and $M_s$ :yield curve and data from Stevens and Murphy (2001), plus North Korea $M_s$ and yield estimate. ....  | 16 |
| Figure 3.1. Overview of surface wave dispersion and attenuation analysis. We derive earth structure from a large number of dispersion curves, then use the Born approximation to derive amplitude corrections using this structure prior to Q inversion. The Q structures are then used to predict attenuation along any path.....  | 18 |
| Figure 3.2. 12 second phase velocity (left) and amplitude (right) kernels across central Asia. ...  | 20 |
| Figure 3.3. Eurasian phase velocity model at 10 seconds from Stevens et al. (2005).....   | 21 |
| Figure 3.4. Left - predicted amplitude variations at 10 seconds through the phase velocity model of Figure 2 on paths out of Lop Nor. Right – same, but the velocity model has been smoothed by modeling it as a bilinear rather than piecewise discontinuous function.....   | 21 |
| Figure 3.5. Comparison of Born approximation (left) with finite difference calculation (right) of amplitude perturbations at 20 seconds (top) and 10 seconds (bottom). The rectangular inclusion is modeled after the Tarim Basin structure, and the external structure after a Eurasian shield earth structure. The source is on the horizontal axis at the right edge of the plot. There is general agreement in the features of the two calculations. The amplitude is increased in a band above and to the left of the inclusion in both cases, and decreased above that. However, there are some interference effects in the finite difference calculation that are not reproduced in the Born calculation, and the patterns of high and low amplitudes to not match exactly. .... | 22 |
| Figure 3.6. Vertical component velocity after propagation across the low velocity basin (left). There is a strong diffracted wave that interferes with the direct wave. The right figure shows two observed waveforms that passed through the Tarim Basin and have two distinct surface wave arrivals.....  | 23 |
| Figure 3.7. Events within green circle (lower right) propagate at various distances in from the southern edge of the Tarim Basin to a KNET station (red lines). The northernmost event proved to have a complex source. All other events are shown, ordered by azimuth (northernmost path topmost), in the next two images. Scale indicates sediment thickness in km. ....  | 24 |
| Figure 3.8 KNET seismograms of the events with paths through the Tarim Basin. All records are normalized by the 40-50 second period surface wave amplitude. Amplitudes vary at higher frequency, as predicted by the simulations. The amplitude of the 10-20 second period surface wave from the event with the most glancing path becomes very large (bottom trace). ....  | 25 |
| Figure 3.9. Seismograms from the same events as the previous figure, in the same order and normalized by the 40-50 second surface wave amplitudes, but recorded at KMI (~130° azimuth, away from the Tarim Basin). The amplitudes are more consistent and waveforms   |    |

|   |    |
|---|----|
| much less complex, indicating that the amplitude variation and complexity observed at KNET can be attributed to the effects of the propagation near the basin boundary. ....  | 25 |
| Figure 3.10. Paths (top) and data (bottom) for the Lop Nor explosion of June 8, 1996. Data is filtered from 0.01 to 0.1 Hz. ....  | 26 |
| Figure 3.11. Raw (upper left) and Path Corrected (upper right) Spectra for the Lop Nor explosion of June 8, 1996, and Born corrections (bottom) calculated for the same paths. Perfectly corrected spectra should be flat.....  | 27 |
| Figure 3.12. Synthetic surface wave seismograms without (left) and with (right) Born corrections.....   | 27 |
| Figure 3.13. Homogeneous layered model. Numbers show $V_p$ , $V_s$ and density. Trailing zeros indicate infinite $Q$ . ....   | 28 |
| Figure 3.14. Heterogeneous model vertical profile of $V_p$ (left) and $V_s$ (right) at about 42N. ....  | 28 |
| Figure 3.15. Amplitude perturbations $\ln(A/A_0)$ at 20 seconds for finite difference calculation (left) and Born approximation (right). The star is at the source location. ....   | 29 |
| Figure 3.16. Amplitude perturbations $\ln(A/A_0)$ at 10 seconds for finite difference calculation (left) and Born approximation (right). The star is at the source location. ....   | 29 |
| Figure 3.17. Snapshots of vertical velocity propagating from Lop Nor to KNET for 3D finite difference calculation. Figures show snapshots at multiples of 60 seconds from 60 to 360 seconds. Amplitude scale range is proportional to $1/t^{1/2}$ , which approximately corrects for surface wave geometric spreading.....  | 30 |
| Figure 4.1 Maps showing events processed (left) and stations recording data from these events (right). ....   | 34 |
| Figure 4.2. Histogram of distances of all rays in the data set. Each frequency is considered distinct in this plot.....   | 34 |
| Figure 4.3. Change in moment for each event processed. “All Data” refers to inversion of the SAIC and CU data simultaneously while the other data sets were inverted independently. Inversion of all data together gives very similar results to inversion of individual data sets. Application of Born corrections also makes little difference to the moment corrections. ... | 35 |
| Figure 4.4 Comparison of inversion results with base model for one central Asian structure. In this case, all data sets show lower $Q$ , with the Born adjusted data set showing a larger change. ....  | 35 |
| Figure 4.5. Data fits for four paths of different ranges for the same event. The red line is the starting model and the green line the final gamma model. The blue line corresponds to the data fit and is the green line shifted by an amount corresponding to the moment adjustment. This adjustment is larger at closer distances. The red marks are the data points. ....   | 36 |
| Figure 4.6. Average gamma for all paths after inversion (blue), in original data set (red) and starting model (green). Dashed lines are $\pm 1$ standard deviation. For paths between 5000 and 10,000 km. ....  | 37 |
| Figure 4.7. Average gamma for all paths after inversion (blue), in original data set (red) and starting model (green). Dashed lines are $\pm 1$ standard deviation. For paths between 1000 and 5,000 km. ....   | 37 |
| Figure 4.8. Average gamma for all paths after inversion (blue), in starting model (green), and as determined by amplitude decay along all paths for each event (red). Dashed lines are $\pm 1$ standard deviation. Average gamma and starting model are for paths in the data set longer than 1000 km (top) and longer than 5000 km (bottom). ....                              | 38 |

|  |    |
|--|----|
| Figure 4.9. Attenuation inversion results at 20 seconds – left: gamma map, right: gamma histogram. Inversion data sets from top to bottom: All data, SAIC data, SAIC data Born Corrected, CU. .... | 39 |
| Figure 4.10 Attenuation inversion results at 15 seconds – left: gamma map, right: gamma histogram.....   | 40 |
| Figure 4.11. Attenuation inversion results at 12.5 seconds – left: gamma map, right: gamma histogram.....  | 41 |
| Figure 4.12. Attenuation inversion results at 10 seconds – left: gamma map, right: gamma histogram.....  | 42 |
| Figure 4.13. Attenuation inversion results at 8 seconds – left: gamma map, right: gamma histogram.....   | 43 |
| Figure 4.14. Attenuation inversion results at 6.6 seconds – left: gamma map, right: gamma histogram.....   | 44 |

## List of Tables

|  |    |
|--|----|
| Table 2.1. Comparison of time domain and spectral magnitude measurement and correction terms.....                  | 7  |
| Table 2.2. Station and network mean values for $M_s$ calculated using the mean values over the frequency band..... | 13 |
| Table 2.3. Station and network mean values for $M_s$ calculated using peak values within the frequency band.....   | 13 |
| Table A1. List of events processed for Q inversion.....  | 50 |



## 1.0 Introduction and Summary

The objective of this project is to optimize surface wave measurements, particularly at regional and local distances, and over the high frequency period band of 8-15 seconds. There are three main parts to this study: 1) We collect and then invert Eurasian surface wave amplitude data for attenuation and Q structure; 2) we develop amplitude corrections using the Born approximation and then compare them with observations and with the results of finite difference calculations; 3) we develop a time domain path corrected surface wave magnitude and compare it with other surface wave magnitudes. In addition, we analyze the surface waves from the North Korean nuclear test of October 9, 2006. The path corrected surface wave magnitude is similar to the Butterworth filtered magnitude developed by Russell, but regionalized to take into account variations in earth structure and attenuation. We conclude that the Born approximation is of marginal value for attenuation studies because it is a small perturbation approximation and the observed amplitude variations are too large and complicated to be predicted by the Born approximation. We find that the average surface wave Q of Eurasia is lower than our previous background model, particularly along a band running through the Middle East. We develop attenuation maps that predict attenuation along any path in Eurasia for frequencies below 0.15 Hz for distribution to AFRL, the DOE Knowledge Base and other researchers.

### 1.1 Attenuation

We inverted surface wave amplitude data for attenuation and corrections to source moment for data from about 300 Eurasian earthquakes. We used two data sets: one our own measurements and one set from Anatoli Levshin at the University of Colorado. The data sets are fairly consistent and both indicate higher attenuation than our initial background model. There is a large amount of scatter in both data sets, likely the result of structural variations and interference. Nevertheless, there is enough redundancy in the data that we were able to perform Q inversions for the Eurasian continent. Figure 1.1 shows a map of the attenuation coefficients determined by the inversion at 10 seconds period, and the data fit averaged over all paths.

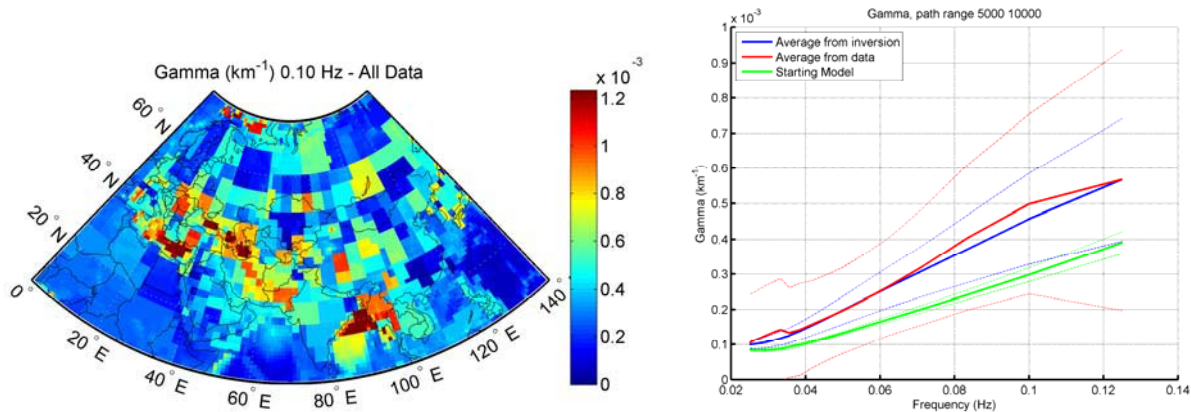
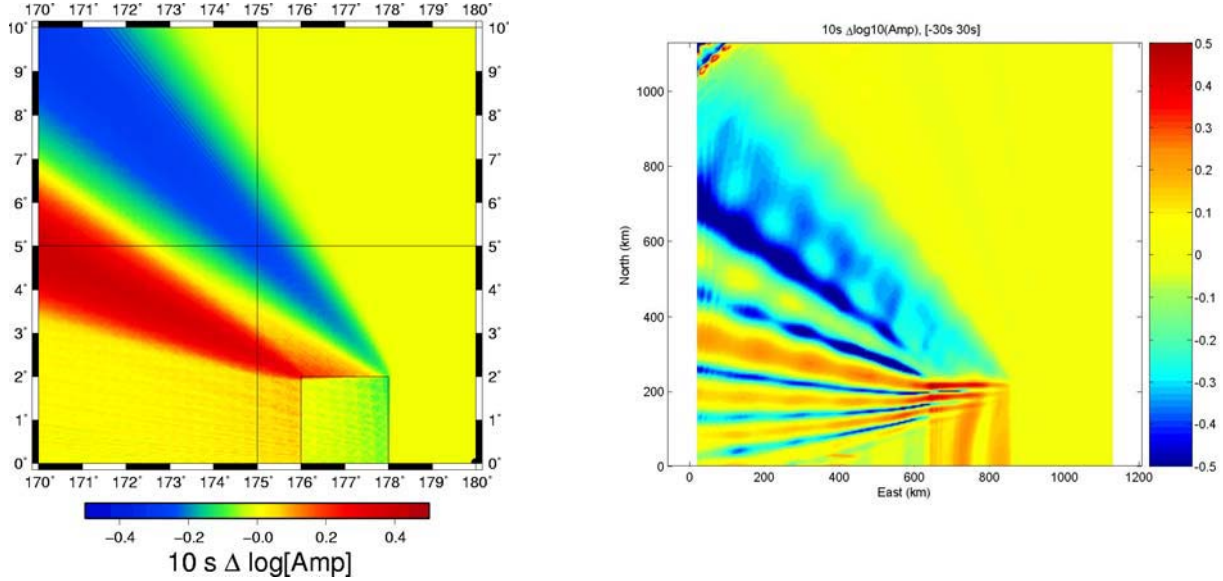


Figure 1.1. Attenuation coefficients at 10 seconds period in Eurasia derived by inversion of surface wave amplitude measurements (left), average data and average data fit (right). Blue curve shows the inversion results, the red curve the average of the data, and the green line the starting model, averaged over all paths longer than 5000 km. Dashed lines show one standard deviation above and below each curve.

## 1.2 Born approximation

We modeled the effect of heterogeneous structure using the Born approximation. We performed both data analysis and large 3-dimensional finite difference calculations to assess the performance of the Born approximation. Our goal was to use the Born approximation to correct for scattering and diffraction caused by heterogeneous structure prior to performing Q inversions. However, the structural complexity appears to exceed the limits of the Born approximation, and application of the Born corrections do not improve inversion results at these high frequencies. Figure 1.2 shows a comparison of the Born approximation with the results of a 3D finite difference calculation at 10 seconds period. Both model an explosion near the right side of the grid in a background medium typical of Eurasian shield regions, with an inclusion of low velocity material modeled after the Tarim Basin. Although there is similarity between the two calculations, the Born approximation does not reproduce the fine structure of the numerical calculations, and the disagreement is large enough that the Born corrections are inadequate for the purposes of correcting surface wave amplitudes at individual receiver points.



**Figure 1.2.** Comparison of Born approximation (left) with finite difference calculation (right) of amplitude perturbations at 10 seconds. The rectangular inclusion is modeled after the Tarim Basin structure, and the external structure after a Eurasian shield earth structure. The source is on the horizontal axis at the right edge of the plot. The amplitude is increased in a band above and to the left of the inclusion in both cases, and decreased above that. However, there are some interference effects in the finite difference calculation that are not reproduced in the Born calculation.

## 1.3 Path corrected magnitude

Russell (2006) proposed a new type of surface wave magnitude  $M_{s(b)}$  that uses a Butterworth filter to measure a time domain amplitude in a narrow band around any desired frequency, and then applies a correction for the frequency dependence of an explosion source function. The main purpose of  $M_{s(b)}$  is to allow surface waves to be measured at regional distances at higher frequencies than traditional 20 second  $M_s$ . The magnitude is defined by

$$M_{s(b)} = \log(A_b) + \frac{1}{2} \log(\sin \Delta) + 0.0031 \left( \frac{20}{T} \right)^{1.8} \Delta - 0.66 \log \left( \frac{20}{T} \right) - \log(f_c) - 0.43 \quad (1.1)$$

where  $A_b$  is the filtered amplitude,  $T$  is the measured period, and  $f_c$  is the Butterworth filter width.

A regionalizeable path corrected time domain magnitude can be derived by combining the path corrected spectral magnitude (Stevens and McLaughlin, 2001) with  $M_{s(b)}$ , using the source and path corrections from earth models to replace the empirical corrections. We define the path corrected time domain magnitude  $M_{s(bp)}$  as:

$$M_{s(bp)} = \log(A_b) + \frac{1}{2} \log(\sin \Delta) + \gamma_p \Delta \log e - \log(S_1) - \log(S_2) - \log(f_c) + C_{bp} \quad (1.2)$$

Where  $S_1$  and  $S_2$  are source and path excitation functions,  $\gamma_p$  is the attenuation function between the source and receiver, and  $C_{bp}$  is a constant chosen to make  $M_{s(bp)}$  consistent with historical magnitude, which is shown to be  $C_{bp} = -17.96$ .

The Russell Butterworth filtered magnitude and the path corrected time and frequency domain magnitudes have a similar purpose, specifically to allow surface waves to be measured at regional and local distances and at higher frequencies than 20 seconds. These magnitudes give similar results when applied to data and are consistent in value with traditional 20 second magnitudes. The path corrected magnitudes have the advantage that they can be regionalized to take into account differences in earth structure and attenuation, while the Butterworth filtered magnitude uses a good representative average value for these quantities. An issue with all of the magnitudes is how to determine which frequency(ies) to measure. The path corrected spectral magnitude, for example, performs a robust average over all frequencies, while the Bonner et al. implementation of the Butterworth filtered magnitude uses the maximum value. Using the maximum value may give better discrimination but at the cost of more variability in the magnitude.

#### 1.4 Korea

The North Korean nuclear test of October 9, 2006 generated larger than expected surface waves, nearly a magnitude unit higher than would be expected based on larger events assuming a  $M_s:\log(\text{yield})$  slope of one. Some of this difference can be explained by the absence of tectonic release and high velocity source medium for this event. However, the results also suggest that the  $M_s:\log(\text{yield})$  slope may be less than one, which has implications for discrimination of small events as well as yield estimation. Figure 1.3 shows path corrected magnitudes for 7 stations that recorded the North Korean explosion. Although there is some variation due to earth structure, they clearly show an  $M_s$  of about 2.9. The right side of Figure 1.3 shows a fit to the  $M_s:\text{yield}$  data for all other explosions with known, unclassified yield and  $M_s$ , showing that the predicted  $M_s$  for this event is approximately 2.0. However, this is based on a slope of 1 in the  $M_s:\log(\text{yield})$  curve, which is expected from cube root scaling, but may not be right. The other curves show Mueller-Murphy source predictions for standard containment depth and for an overburied explosion (believed to be the case here), and those curves are much more consistent with the North Korean data point.

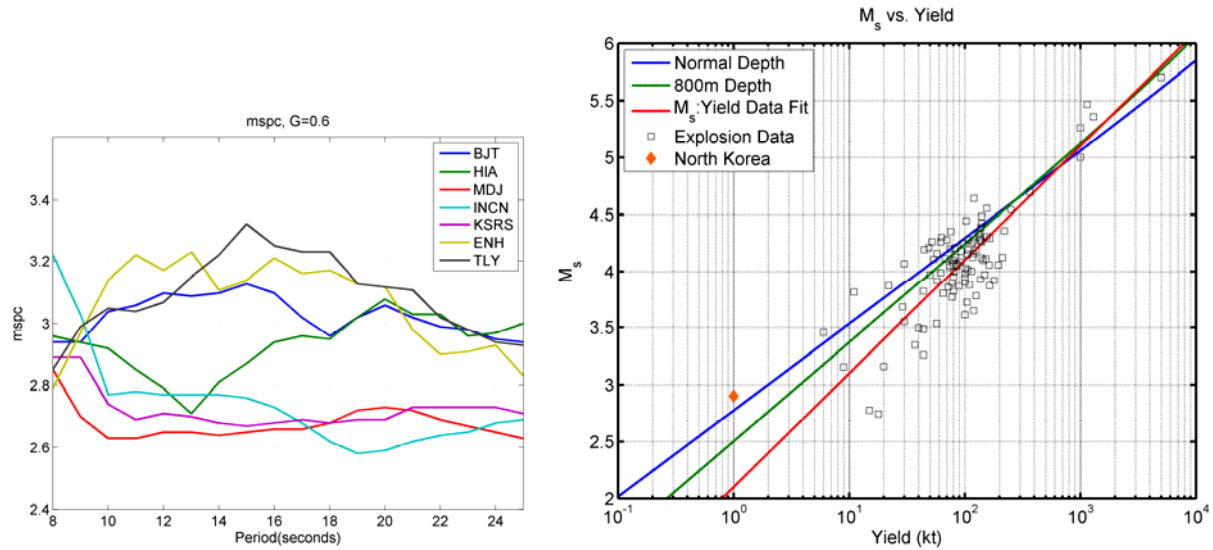


**Figure 1.3. Path corrected surface wave magnitudes for the North Korean nuclear test, and fit to three  $M_s$ :Yield curves for an estimated yield of 1 kiloton, together with historical  $M_s$ :Yield data.**

## 1.5 Recommendations

Additional research is needed in the following areas:

1. The high  $M_s$  of the North Korean earthquake suggests that the  $M_s$ :log yield slope may be less than one, which has implications for discrimination of small events as well as yield estimation. More research is needed to analyze surface waves from small events of known yield in high velocity media to see if the North Korean event is an anomaly or the norm.
2. The Butterworth filtered magnitudes and spectral magnitudes are all sensitive to how the frequency for measurement is picked. As discussed above, using the maximum value may give better discrimination but at the cost of more variability in the magnitude, and that advantage may go away for small events. More research is needed to determine the optimum frequency strategy.
3. A method for correcting surface wave amplitudes for path structure is needed. As discussed above, the Born approximation is not adequate for structures as complex as Eurasia at frequencies of 8-15 seconds. Other approximation methods have similar problems, and a new procedure may be required.
4. The robustness of the Q models for Eurasia depend on the amount of data that goes into the inversion. That is particularly true in the absence of an adequate method for correcting for earth structure. So we recommend that a much larger data set be processed and included in the Q inversion.

## 2.0 Path Corrected and Frequency Dependent Surface Wave Magnitudes

Surface wave magnitudes play an important role in earthquake/explosion discrimination. Three main problems exist with traditional surface wave magnitudes: 1) surface wave dispersion causes amplitude variations unrelated to the source; 2) it is not possible to reliably measure a traditional 20 second surface wave magnitude at local and regional distances because the surface wave is not dispersed enough; and 3) differences in earth structure and attenuation cause variations in surface wave amplitudes that are unrelated to the source. Several surface wave magnitude measurements have been proposed to address these limitations, and we propose some further improvements in the form of a regionalized path corrected surface wave magnitude. In the following section we compare these magnitude types in detail, and then apply them to the North Korean nuclear test. We also use this as an example of separating the surface waves into their component source, receiver and path parts, and examine the residual to show the effect of structural variations.

### 2.1 Comparison of Butterworth filtered and regionalized surface wave magnitudes

Russell (2006) proposed a new type of surface wave magnitude  $M_{s(b)}$  that uses a Butterworth filter to measure a time domain amplitude in a narrow band around any desired frequency, and then applies a correction for the frequency dependence of an explosion source function. The main purpose of  $M_{s(b)}$  is to allow surface waves to be measured at regional distances at shorter periods than traditional 20 second  $M_s$ . The magnitude is defined by

$$M_{s(b)} = \log(A_b) + \frac{1}{2} \log(\sin \Delta) + 0.0031 \left( \frac{20}{T} \right)^{1.8} \Delta - 0.66 \log \left( \frac{20}{T} \right) - \log(f_c) - 0.43 \quad (2.1)$$

where  $A_b$  is the filtered amplitude,  $T$  is the measured period, and  $f_c$  is the Butterworth filter width. This magnitude also requires that the frequency band be less than a minimum value defined by  $f_c \leq \frac{G_{\min}}{T\sqrt{\Delta}}$ . Russell (2006) finds  $G_{\min}=0.6$  for continental structures at periods between 8 and 40 seconds, with smaller values required for deep sediment structures. Russell (2006) also shows that  $A_b = \frac{f_c T \sqrt{\Delta}}{G} A$  where  $G$  is a constant which for typical continental paths is approximately 0.93, and  $A$  is the equivalent time domain amplitude. Note that if  $G_{\min}$  is fixed, then the filter correction corresponds to a distance correction for a normally dispersed (non-Airy phase) surface wave of  $\frac{1}{2} \log \Delta$ .

Stevens and McLaughlin (2001) defined a path corrected spectral magnitude, which similarly is intended to allow surface waves to be measured at all distances and frequencies, and in addition is regionalizeable since it is derived from earth models. The path corrected spectral magnitude,  $\log M_0'$ , is calculated by dividing the observed surface wave spectrum by the Green's function for an explosion of unit moment and taking the logarithm of this ratio, averaged over any desired frequency band. The path corrected spectral magnitude is defined as the logarithm of:

$$M_0' = \left| U_z(\omega, r, \theta) / \left( \frac{S_1^x(\omega, h_x) S_2(\omega) \exp[-\gamma_p(\omega)r]}{\sqrt{a_e} \sin(r/a_e)} \right) \right| \quad (2.2)$$

where  $U_z$  is the observed vertical component surface wave spectrum,  $S_1^x$  depends on the source region elastic structure and the explosion source depth,  $S_2$  depends on the receiver region elastic structure, and  $\gamma_p$  is the attenuation coefficient that depends on the attenuation integrated over the path between the source and receiver. All of the functions in equation 2.2 can be derived from plane-layered earth models (see Stevens and McLaughlin, 2001), and allow the measurement to be regionalized to account for differences in earth structure at the source and receiver, and due to attenuation along the path. Since  $M_0'$  is a physical quantity, equation 2.2 is assumed to be in SI units and  $\log M_0'$  is in  $\log(\text{nt-m})$ , however in the following comparison we express  $U_z$  in nm-s for consistency with the other amplitude measurements. This adds a constant value of -9 to the normalization constant for  $\log M_0'$ .

Since equations 2.1 and 2.2 are both intended to flatten the surface wave spectrum, in principle they can be measured over any desired frequency band. In practice, the path corrected spectral magnitude (equation 2.2) has been calculated by averaging over a frequency band designed to avoid noise contamination, with implementation of an outlier rejection scheme to minimize bias from spectral dips and noise (Stevens et al., 2005). The implementation of the Butterworth filtered magnitude (equation 2.1) by Bonner et al. (2006) has instead used the maximum value over a period band of 8-25 seconds, defined as  $M_s(\text{VMAX})$ , with analyst rejection of outliers.

A path corrected time domain magnitude can be derived by combining the path corrected spectral magnitude with  $M_{s(b)}$ , using the source and path corrections from earth models to replace the empirical corrections. We define the path corrected time domain magnitude  $M_{s(bp)}$  as:

$$M_{s(bp)} = \log(A_b) + \frac{1}{2} \log(\sin \Delta) + \gamma_p \Delta \log e - \log(S_1) - \log(S_2) - \log(f_c) + C_{bp} \quad (2.3)$$

where  $C_{bp}$  is a constant chosen to make  $M_{s(bp)}$  consistent with historical magnitudes. By defining  $M_{s(bp)}$  to be equal to Rezapour and Pearce (1998)  $M_s$  at  $50^\circ$ , and simultaneously using the Rezapour and Pearce attenuation rate, and using the mean 20 second value of  $S_1$  and  $S_2$  for Central Asian continental structures ( $\log(S_1) + \log(S_2) = -17.41$ ), we find  $C_{bp} = -17.96$ . We can also define a spectral magnitude directly from equation 2.2, using the relation (again from Russell, 2006)  $A_b = \frac{4\pi}{3} f_c U_z$ . This gives  $\log M_0' - M_{s(bp)} = 11.74$ , which is identical to the mean

difference between  $\log M_0'$  and Rezapour and Pearce  $M_s$  found through measurement of a large data set by Stevens and McLaughlin (2001). We can therefore define an equivalent spectral  $M_s$ , which we define as  $M_{s(sp)} = \log M_0' - 11.74$ , which adding the  $\log M_0'$  normalization constant  $\frac{1}{2} \log(a_e) - 9$  gives an  $M_{s(sp)}$  normalization constant of -17.34. Table 2.1 shows a comparison of the terms in each of these magnitudes, and in the Rezapour and Pearce  $M_s$ .

**Table 2.1. Comparison of time domain and spectral magnitude measurement and correction terms**

| <b>Magnitude Type</b> | <b>Amplitude Measure</b> | <b>Source</b>                         | <b>Receiver</b> | <b>Geometric Spreading</b>      | <b>Attenuation</b>                            | <b>Dispersion</b>         | <b>Filter</b> | <b>Norm</b>                |
|-----------------------|--------------------------|---------------------------------------|-----------------|---------------------------------|---|---------------------------|---------------|----------------------------|
| $M_s$                 | $\log(A/T)$              |                                       |                 | $\frac{1}{2} \log(\sin \Delta)$ | $0.0046\Delta$                                | $\frac{1}{3} \log \Delta$ |               | 2.37                       |
| $M_{s(b)}$            | $\log(A_b)$              | $-0.66 \log\left(\frac{20}{T}\right)$ |                 | $\frac{1}{2} \log(\sin \Delta)$ | $.0031\left(\frac{20}{T}\right)^{1.8} \Delta$ |                           | $-\log(f_c)$  | -0.43                      |
| $\log M_0'$           | $\log(U_z)$              | $-\log(S_1)$                          | $-\log(S_2)$    | $\frac{1}{2} \log(\sin \Delta)$ | $\gamma_p \Delta \log e$                      |                           |               | $\frac{1}{2} \log a_e - 9$ |
| $M_{s(sp)}$           | $\log(U_z)$              | $-\log(S_1)$                          | $-\log(S_2)$    | $\frac{1}{2} \log(\sin \Delta)$ | $\gamma_p \Delta \log e$                      |                           |               | -17.34                     |
| $M_{s(bp)}$           | $\log(A_b)$              | $-\log(S_1)$                          | $-\log(S_2)$    | $\frac{1}{2} \log(\sin \Delta)$ | $\gamma_p \Delta \log e$                      |                           | $-\log(f_c)$  | -17.96                     |

In this table  $A$  is the traditional time domain 20 second amplitude in nm,  $A_b$  is the Butterworth filtered magnitude (using a 3 pole two pass phaseless filter) in nm, and  $U_z$  is the Fourier spectral amplitude in nm-s. Figure 2.1 (left) shows a comparison of Russell's approximation to the explosion excitation function with  $\log(S_1)+\log(S_2)$  (plus a constant to normalize to zero at 20 seconds). As the figure shows, this is a good approximation to the average excitation function across the frequency band, however there is substantial regional variation in the function that is accounted for in the path corrected magnitudes.

Figure 2.1 (right) shows that attenuation calculated from earth models is somewhat higher than the Rezapour and Pearce attenuation, and both are higher than the Russell attenuation, which is based on the earlier model of von Seggern (1977). The model-based attenuation corresponds to a Rayleigh wave  $Q$  of about 400, while the Rezapour/Pearce and von Seggern/Russell attenuation correspond to Rayleigh wave  $Q$  of about 550 and 800, respectively. The  $Q$  value of 400 is more consistent with empirical Rayleigh wave  $Q$  studies than the higher values of the other magnitudes, and later in this report we find that  $Q$  values for much of Eurasia are still lower. The higher  $Q$  values in the Rezapour and Pearce and von Seggern studies may be because those magnitudes were based on Rayleigh wave amplitudes covering a large distance range, and Rayleigh waves along lower  $Q$  paths have attenuated away at the larger distances, biasing the attenuation estimates to higher  $Q$  values.

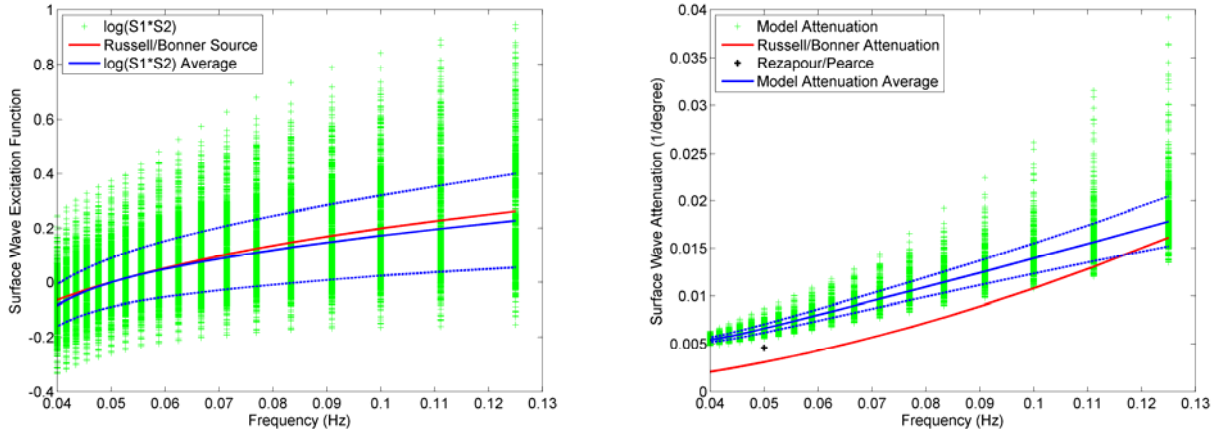


Figure 2.1 Left: Mean  $\log(S1*S2)$  and  $\pm 1$  standard deviation (blue). Red line shows the Russell approximation for the source function. Right: Mean attenuation and  $\pm 1$  standard deviation (blue) derived from earth models, Russell approximation for attenuation (red), and Rezapour and Pearce global estimate at 20 seconds (black). In both, green marks show values for individual Eurasian structures.

Figure 2.2 compares the magnitude distance corrections, which are the equations listed in Table

2.1 calculated with  $A=1$ ,  $G_{\min}=0.6$ ,  $f_c = \frac{G_{\min}}{T\sqrt{\Delta}}$  and  $A_b = \frac{f_c T \sqrt{\Delta}}{G} A$ , for periods of 20 and 10 seconds, respectively.

Differences between the distance corrections are generally small. The main differences are the larger correction at close distances for the Rezapour and Pearce magnitude, and the larger correction for the path corrected magnitude with model-based attenuation at large distances.  $M_{s(bp)}$  will, of course, vary for each source and receiver location corresponding to the particular earth structure and path attenuation. The magnitude correction at close distances is also larger for  $M_{s(b)}$  than for  $M_{s(bp)}$  because the difference in attenuation causes a small difference in the normalization constant which is calculated at 50 degrees.

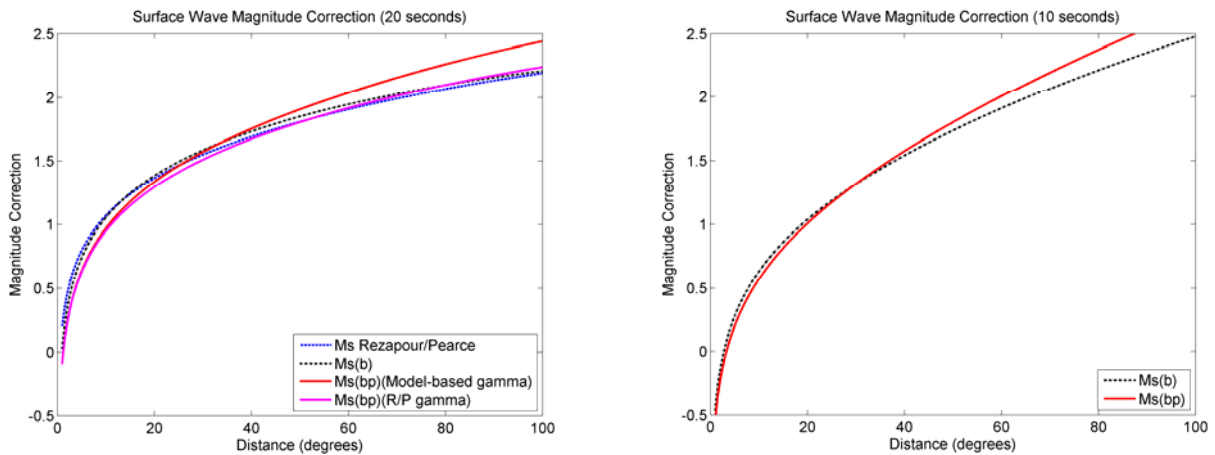


Figure 2.2. 20 second magnitude correction vs. distance for Rezapour/Pearce (dashed blue),  $M_{s(b)}$  (dot-dash black),  $M_{s(bp)}$  with model-based gamma (solid red), and  $M_{s(bp)}$  with Rezapour and Pearce gamma (solid maroon) (left). 10 second magnitude correction vs. distance  $M_{s(b)}$  (dot-dash black), and  $M_{s(bp)}$  with model-based gamma (solid red) (right).

## 2.2 Analysis of surface waves from the North Korean nuclear test

To examine the differences between magnitudes in more detail and illustrate some potential problems, we apply the magnitude methods to surface waves from the North Korean nuclear test of October 9, 2006. This is a good test case because the surface waves are small – above noise level at only 7 of the closest stations (Figure 2.3), difficult to see at all in the unfiltered records, but visible at these stations when low pass filtered (Figure 2.4).

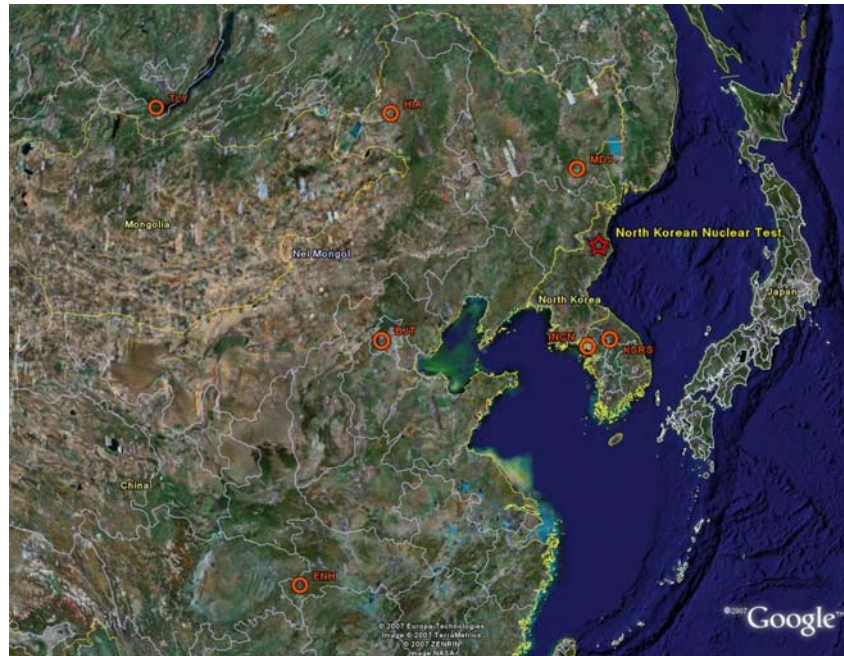
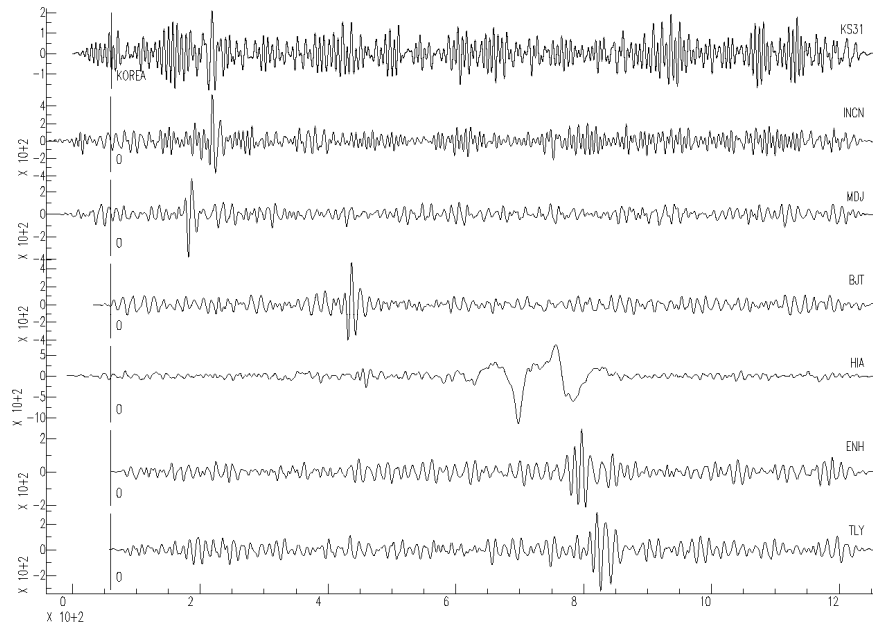
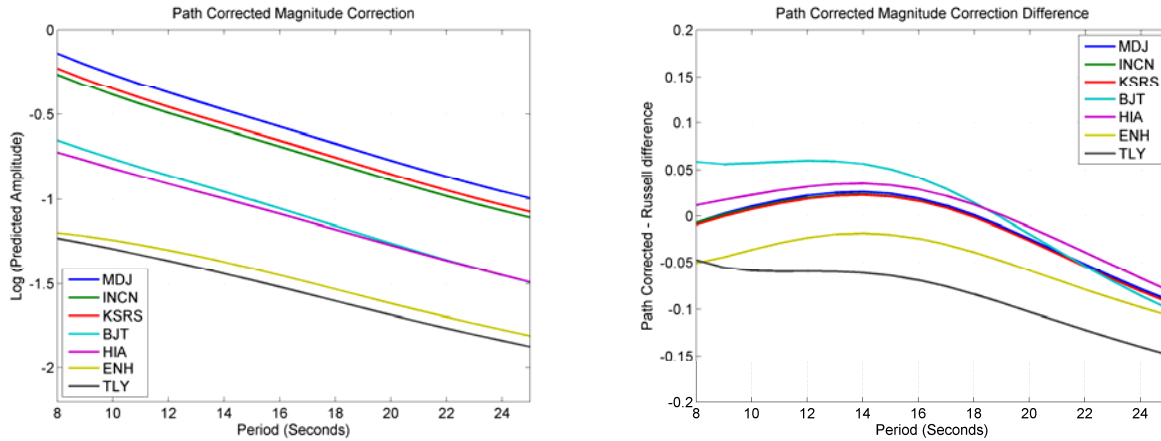


Figure 2.3. Location of the North Korean nuclear test and recording stations.



**Figure 2.4. Data from the North Korean explosion filtered from 0.01-0.1 Hz. Surface waves are clearly visible at all stations. HIA has a glitch or interfering arrival after the explosion arrival. The explosion arrival is visible just after the BJT arrival.**

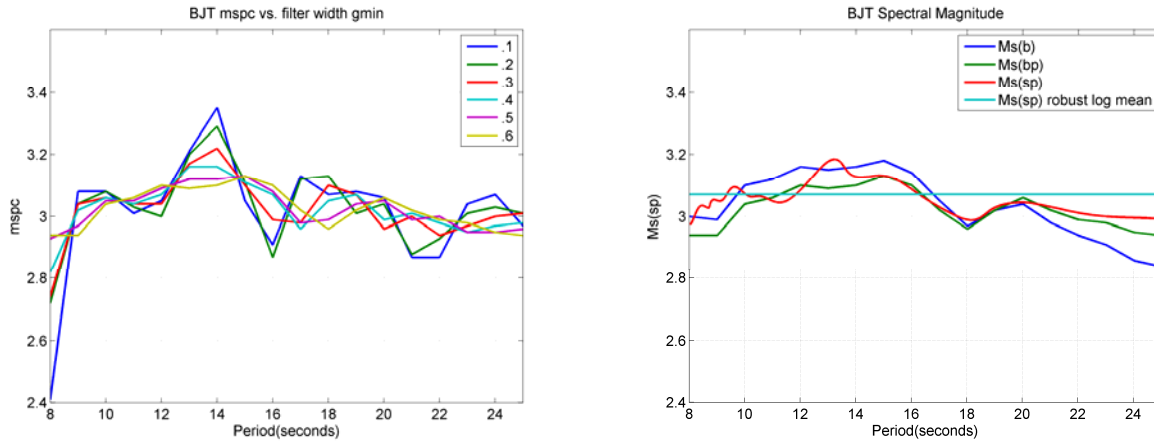
Figure 2.5 shows the predicted spectra at each of the 7 stations based on the model based source and path corrections – these are the negative of the sum of corrections in row 5 of Table 2.1, and are equivalent to predicted, normalized explosion-generated surface wave spectra at each location. Differences between the model-based and Russell sets of corrections (Figure 2.5, right) range from -0.15 to 0.05 magnitude units.



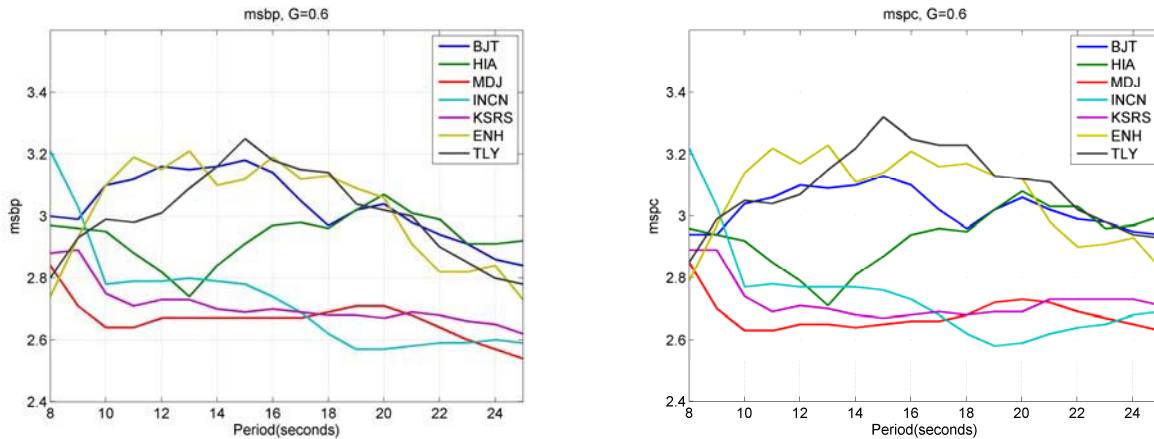
**Figure 2.5. Path corrections for the 7 stations that recorded surface waves from the North Korean nuclear test using model based corrections (left) and differences between the model-based and Russell path corrections for the 7 stations recording the North Korean event.**

Figure 2.6 (left) shows the calculated Butterworth filtered and path corrected spectral magnitudes for station BJT for 6 values of filter width, as specified by  $G_{\min}$  ranging from 0.1 to 0.6. The higher values correspond to wider filter widths which has the effect of smoothing the spectrum and giving more consistent values between frequencies. A disadvantage of the larger values,

however, is that the frequency band extends farther outside of the band of interest, possibly allowing contamination by noise or other phases. Figure 2.6 (right) shows the Butterworth filtered magnitude for  $G_{\min}=0.6$ , the path corrected magnitude, the path corrected spectral magnitude, and the best value of the path corrected spectral magnitude calculated using a robust mean (Stevens et al., 2005). Figure 2.7 shows a comparison of Butterworth filtered magnitudes with and without path corrections. If the procedure were working perfectly and the surface wave spectra were just like synthetics, then all of the curves in Figures 2.6 and 2.7 would be flat lines. The path corrected spectra are slightly flatter than the Butterworth filtered spectra, but it is clear that unmodeled variations are significantly larger than the differences between the individual magnitude curves.



**Figure 2.6. Calculation of path-corrected Butterworth filtered magnitude for 6 filter widths (left) at station BJT. Butterworth filtered, path corrected, and spectral magnitudes at BJT (right).**



**Figure 2.7. Butterworth filtered (left) and path corrected (right) magnitudes for the North Korean nuclear test with varying filter widths.**

The spectra divide into two distinct groups – lower values at INCN, KSRS and MDJ, and higher values at BJT, ENH and TLY. HIA is more complicated, but generally higher. Furthermore, the three lower amplitude stations, which are also the closest stations, have much flatter corrected spectra than the three higher amplitude stations, suggesting a possible frequency dependent amplification of these surface waves. Also, the lower amplitude stations are located due north

and south of the event, while the other stations are located to the west (and northwest/southwest). Since we have corrected for source and receiver structure, and attenuation differences could not be responsible for differences this large on paths this short, there are two remaining likely causes for the amplitude variations: tectonic release (or other azimuth dependent source component), and focusing due to path structure.

The effect of path structure calculated using the Born approximation (Zhou et al., 2004) and the earth models of Stevens et al. (2005) is shown in Figure 2.8. Although there are clearly some big differences between the predictions and observations, there are also some interesting similarities. First, the corrections for the three closest stations are almost flat and separated by approximately the same amount as the observations. Second, the amplitude correction for ENH is similar to what is observed for ENH and also similar to the observations at TLY and BJT. That is, the data show a peak in the spectrum in the middle periods, dropping back close to the level of the closer stations at the longest and shortest periods. On the other hand a very large amplification, which is not observed, is predicted for BJT due to a grazing path along the north end of the Yellow Sea, and a big decrease, also not observed, is predicted for TLY. There are two likely explanations for this: 1) the one degree structural resolution is not sufficient for these short paths; and/or 2) the structural complexity exceeds the limits of the Born approximation. The amplification predicted for BJT by the Born approximation, for example, is very strongly dependent on exactly where the station is with respect to the low velocity zone. The Born approximation and an analysis of the effectiveness of its amplitude correction are discussed in detail in the next section of this report.

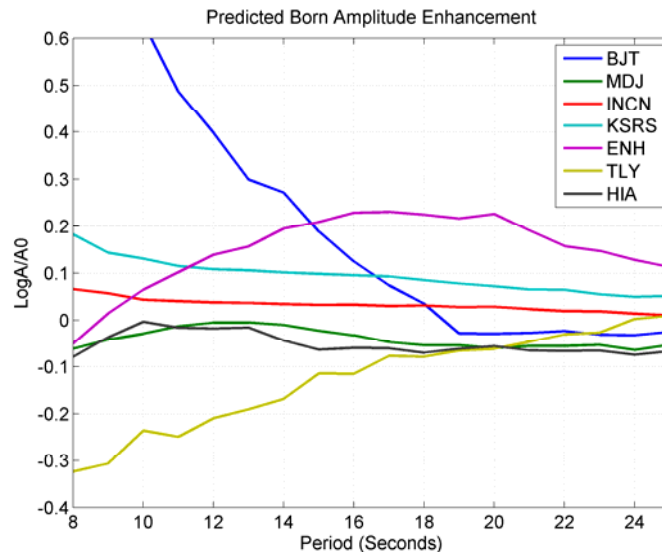


**Figure 2.8. Amplitude corrections due to structure predicted using the Born approximation.**

Tectonic release could cause the observed ~factor of 2 offset between the two station sets. If, for example, tectonic release had the mechanism of a normal fault with tension in the east-west direction, it would amplify stations to the west more than to the north. However, to cause a factor of 2 difference would require a secondary source large enough that large Love waves would also be expected. No Love waves are apparent in any of the data. In any case, path structure seems a more likely cause of the variability, and it is possible that the variations would be predictable

with higher resolution earth models, and/or a more accurate method for accounting for structural variations.

One final issue is the most appropriate measurement of  $M_s$  derived from spectra. In our previous work, and in the discussion above of the path corrected spectral magnitude, we have used a robust mean value as the best estimate. Bonner et al., however, have instead used the maximum value of the Butterworth filtered  $M_s$ . This has some advantage in discrimination, because although the corrections flatten explosion spectra, they do not quite flatten earthquake spectra, which tend to be larger at lower frequencies (Figure 2.9). So in principle the  $M_s$  value for explosions is frequency independent, while the earthquake  $M_s$  can choose a higher value, improving the  $M_s:m_b$  discriminant. As the explosion spectra above demonstrate, however, there are variations in the explosion spectra also, and choosing the maximum point can lead to an  $M_s$  that is too high, degrading discrimination. We made one modification to Bonner et al.'s  $M_s(VMAX)$  procedure by implementing a simple outlier rejection test – we calculate the mean and standard deviation of the magnitudes and reject outliers greater than two standard deviations from the mean. We then recalculate the mean and repeat the outlier rejection, using the remaining points to calculate either the mean or maximum magnitude. Tables 2.2 and 2.3 show a comparison of magnitudes for this event using the different methods (defined in Table 2.1). The results show that the mean value estimates are more consistent than the peak value estimates.

**Table 2.2. Station and network mean values for  $M_s$  calculated using the mean values over the frequency band.**

| Station   | Distance (km) | $M_s(b)$ Mean | $M_s(bp)$ Mean | $M_s(sp)$ Mean |
|-----------|---------------|---------------|----------------|----------------|
| MDJ       | 369           | 2.65          | 2.67           | 2.69           |
| KSRS      | 440           | 2.69          | 2.70           | 2.76           |
| INCN      | 476           | 2.68          | 2.69           | 2.81           |
| BJT       | 1103          | 3.03          | 3.02           | 3.07           |
| HIA       | 1148          | 2.93          | 2.93           | 3.00           |
| ENH       | 2147          | 3.01          | 3.06           | 3.20           |
| TLY       | 2252          | 3.00          | 3.09           | 3.16           |
| Mean (SD) |               | 2.86 (0.18)   | 2.88 (0.19)    | 2.96 (0.20)    |

**Table 2.3. Station and network mean values for  $M_s$  calculated using peak values within the frequency band.**

| Station   | Distance (km) | $M_s(b)$ Peak | $M_s(bp)$ Peak |
|-----------|---------------|---------------|----------------|
| MDJ       | 369           | 2.71          | 2.73           |
| KSRS      | 440           | 2.75          | 2.74           |
| INCN      | 476           | 2.80          | 2.78           |
| BJT       | 1103          | 3.18          | 3.13           |
| HIA       | 1148          | 3.07          | 3.08           |
| ENH       | 2147          | 3.21          | 3.23           |
| TLY       | 2252          | 3.25          | 3.32           |
| Mean (SD) |               | 3.00 (0.23)   | 3.00 (0.25)    |

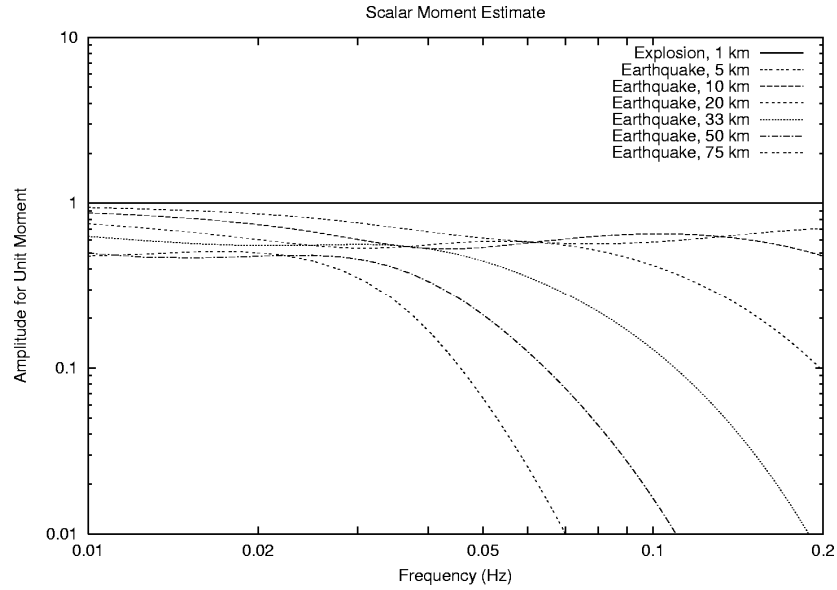


**Figure 2.9.** Path corrected spectra for an explosion and for earthquakes calculated for several depths. The path corrected explosion spectrum is flat over the entire frequency band (for perfect data and path correction), while the path corrected earthquake spectrum is flattened, but has some variation due to source mechanism and source depth and generally decreases with increasing frequency.

### 2.3 Yield estimation, earthquake/explosion discrimination and the North Korean test

The  $M_s$  measurements for this event are larger than expected for an explosion with  $m_b$  4.1. Based on typical  $m_b$ :yield curves for hard rock, an event of that size would have a yield of less than one kiloton. However, Stevens and Murphy (2001) show that  $M_s$ :yield data are fit well with a relation  $M_s = \log(Y) + 2.1$ , which for  $M_s$  2.9 gives an estimated yield of about 6 kilotons. On the other hand, the  $M_s$ : $m_b$  curve for granite from Stevens and Day (1985) comes quite close to the  $M_s$  and  $m_b$  for the North Korean event. The yield estimate for this event and corresponding magnitudes are also affected by the relatively deep source depth. Bennett et al (2006) estimate the source depth between 200 and 800 meters based on the tunnel location and topography. They estimate a yield of about one kiloton using a comparison of P-wave spectra with a source depth of 800 meters. In this section we examine the differences between these estimates.

Figure 2.10 shows  $M_s$ : $m_b$  data from historical explosions together with theoretical curves for  $M_s$  and  $m_b$  from Stevens and Day (1985) for Mueller-Murphy granite (Murphy, 1977). Curves are shown for normal containment depth of  $122Y^{1/3}$  meters and for the estimated 800 meter depth of this event. Although the Korean data point appears to agree quite well with the estimate, this is somewhat misleading because the Stevens and Day magnitudes were normalized to an NTS magnitude yield curve, and so the  $m_b$  estimates are biased low compared to Eurasian  $m_b$  values. Figure 2.10 also shows an  $M_s$ : $m_b$  curve shifted by 0.4 in  $m_b$ , which is more appropriate for the North Korean location. So the  $M_s$  for this event is still high relative to predictions, but consistent with the upper part of the distribution of other explosions.

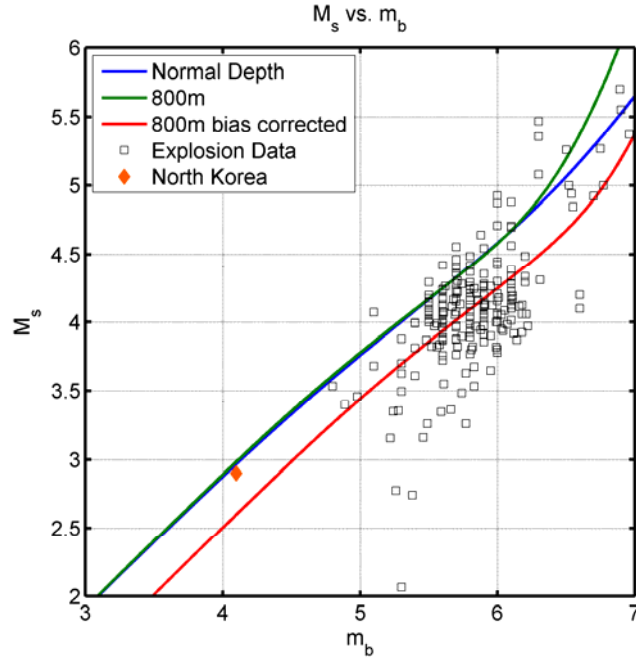


**Figure 2.10.  $M_s:m_b$  curves for Mueller Murphy granite using formulas from Stevens and Day (1985) and with 0.4 mb bias correction. Data from Stevens and Murphy (2001), plus the North Korea data point.**

The nominal  $m_b$ :yield relation for Eurasian hardrock is  $m_b = 0.75 \log_{10} Y + 4.45$  (Murphy, 1996), which would imply a yield of less than  $\frac{1}{2}$  kiloton for this event. Figure 2.11 shows a comparison of the nominal  $m_b$ :yield relation and the granite Mueller-Murphy  $m_b$ :yield curve using standard depth and the 800 meter depth with the bias adjusted Stevens and Day (1985) relations. One kiloton is in good agreement with these curves for overburied depths.

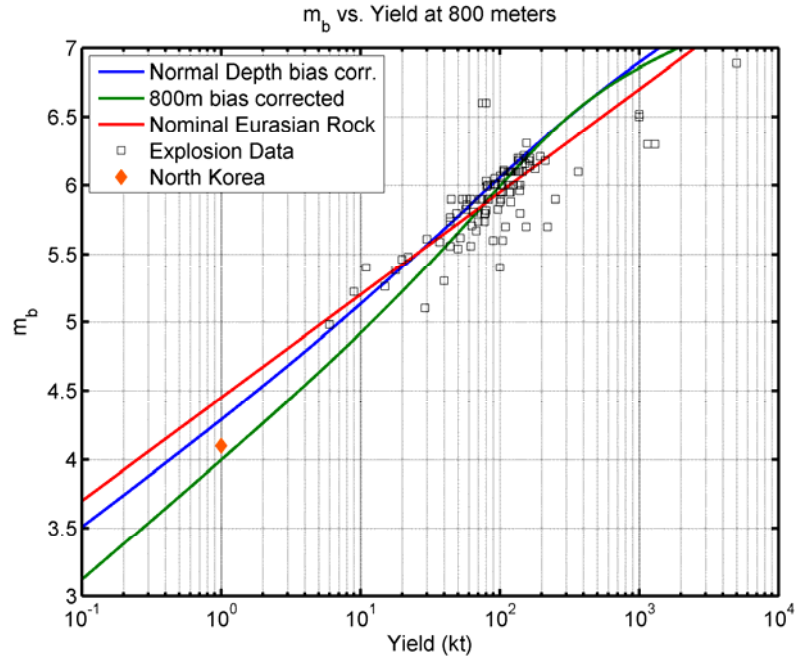


Figure 2.11.  $m_b$ :yield curves for Mueller Murphy granite at normal containment depth and at 800 m depth using formulas from Stevens and Day (1985), and nominal Eurasian  $m_b$ :yield curve (Murphy, 1996). Data from Stevens and Murphy (2001), plus North Korea  $m_b$  and yield estimate.

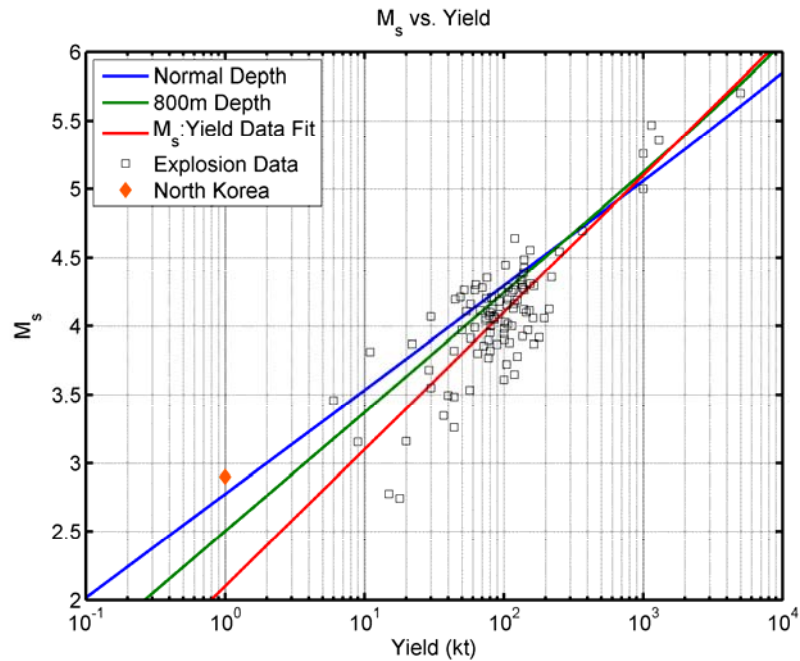


Figure 2.12.  $M_s$ :yield curves for Mueller Murphy granite using formulas from Stevens and Day (1985) for normal containment depth and 800 meter depth, and  $M_s$ :yield curve and data from Stevens and Murphy (2001), plus North Korea  $M_s$  and yield estimate.

Figure 2.12 shows three  $M_s$ :Yield curves: the best fit  $M_s$ :Yield curve with unit slope from Stevens and Murphy (2001), and  $M_s$ :Yield using Mueller-Murphy granite and the Stevens and Day (1985) relations with normal scaled depth and a depth of 800 meters. Although the  $M_s$

appears to agree well with the normal containment depth curve, as discussed above it is very likely that the explosion was overburied. The main difference between the three curves in Figure 2.12 is the slope of the lines. The Stevens and Murphy curve assumed a unit slope, which is expected for varying yield at fixed depth. The Mueller-Murphy model has an empirically determined slope of 0.87 at fixed depth, and a slope of 0.76 when normal containment depth is assumed. The smaller slope occurs because lower overburden pressure at shallower depths increases the source size.

While the North Korean data point is more consistent with the Mueller-Murphy curves, the  $M_s$  is still high by about 0.4 magnitude units relative to the Mueller-Murphy curve for an overburied explosion, and it isn't clear whether the North Korean data point indicates a slope less than one in general, or whether this particular data point is at the high end of the  $M_s$ :Yield distribution. There are two factors that could contribute to the apparently high  $M_s$  relative to the historical data set. The historical data is dominated by events at NTS and Balapan and so 1) the lower material velocities at NTS increase the  $M_s$ : $m_b$  separation as discussed by Stevens and Day, 1985; and 2) many of the events at Balapan exhibit compressive tectonic release, reducing  $M_s$  for those events (Day and Stevens, 1986). The combination of these two effects causes  $M_s$  for a small event in hard rock with no tectonic release to be higher than predicted from a curve with slope 1 derived from a data set with a mixture of source media velocities and a substantial number of events with  $M_s$  reduced by tectonic release.

### 3.0 Amplitude Corrections Using the Born Approximation

Surface wave amplitudes are affected by both attenuation and earth structure. The effect on surface wave amplitudes of propagation normal to variations in earth structure is predicted fairly well by conservation of energy. Propagation along paths at grazing incidence to large structure variations, however, are much more difficult to predict. Our main interest in this project is on understanding amplitude variations in 8-15 second surface waves. In this frequency band, surface waves may be affected as strongly or more strongly by earth structure than by intrinsic attenuation, particularly along shorter paths. Our goal is therefore to be able to model and correct for both of these effects. Our approach is illustrated in Figure 3.1.

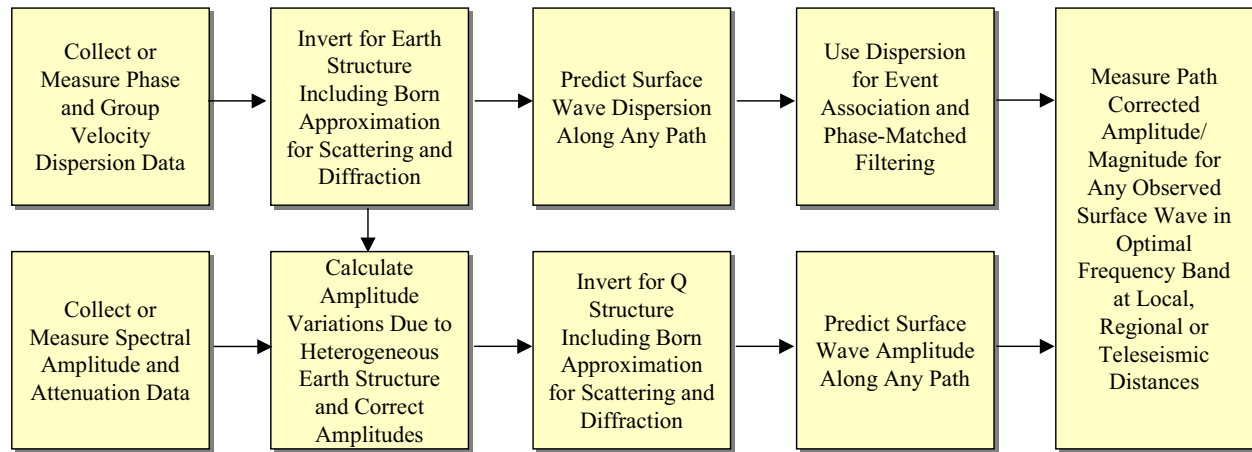


**Figure 3.1. Overview of surface wave dispersion and attenuation analysis. We derive earth structure from a large number of dispersion curves, then use the Born approximation to derive amplitude corrections using this structure prior to Q inversion. The Q structures are then used to predict attenuation along any path.**

In an earlier project (Stevens et al., 2005) we developed global, regionalized dispersion models that allow the phase and group velocity to be calculated between any two points on the earth. We did this by accumulating a large data set consisting of more than 1 million dispersion measurements derived by a number of researchers, and then inverting this data set to determine earth structure, which in turn was used to generate dispersion maps at all frequencies. In that project, we modeled surface waves in a heterogeneous earth using the following approximations: 1) surface waves propagate along great circle paths, 2) surface wave phase and group velocities and anelastic attenuation can be modeled using a path integral between source and receiver, and 3) energy is conserved with no mode conversion across material boundaries. This approximation is quite good for large parts of the world, particularly at lower frequencies, but the unmodeled variations become important in regions of structural complexity.

#### 3.1 Surface wave amplitude predictability

An important goal of this project is to be able to predict surface wave amplitudes in both simple and complex structures, to determine under what conditions the more complicated calculations required for laterally heterogeneous structure are required, and under what conditions the approximations generally used for calculating surface waves in complex structures become inadequate. In the following, we discuss calculations of surface waves in simple and complex structures.

### 3.2 Surface wave propagation in simple structures

We define “simple structures” to mean those structures in which the surface wave propagation is normal to all changes in structure, and lateral changes in structure are negligible. In that case we can predict surface wave amplitude and phase using an approximation originally due to McGarr (1969) that uses propagation of surface waves along great circle paths with conservation of energy across material interfaces and no mode conversion. With these approximations, surface wave propagation in a heterogeneous, anelastic structure takes the following form, separating source, path and receiver (notation follows Harkrider et al, 1994):

$$u_z(\omega, r, \varphi) = \frac{1}{\sqrt{a_e \sin(r/a_e)}} \sqrt{\frac{2A_{R_1}}{\pi\omega c_1^2}} \sqrt{c_2 A_{R_2}} \exp\left[i\left(\pi/4 - \omega r / c_p - \gamma_p r\right)\right] F_s(\omega, \varphi, h) \quad (3.1)$$

where  $\omega$  is angular frequency,  $r$  is source to receiver distance,  $h$  is source depth,  $a_e$  is the radius of the earth,  $\varphi$  is azimuth,  $A_R$  is the Rayleigh wave amplitude function,  $c$  is phase velocity,  $\gamma$  is the attenuation coefficient, and the subscripts 1, 2, and  $p$  refer to parameters derived from the source region structure, parameters derived from the receiver region structure, and parameters which are defined by path averages, respectively. All source properties are contained in the function  $F_s$ . For an isotropic explosion source, the Rayleigh wave spectrum can be written:

$$u_z(\omega, r) = M'_0 \frac{S_1^x(\omega, h_x) S_2(\omega) \exp[-\gamma_p(\omega)r + i(\varphi_0 - \omega r / c_p(\omega))]}{\sqrt{a_e \sin(r/a_e)}} \quad (3.2)$$

where  $\varphi_0$  is the initial phase equal to  $-3\pi/4$ ,  $S_1^x$  depends on the source region elastic structure and the explosion source depth,  $S_2$  depends on the receiver region elastic structure.  $M'_0 = \frac{3\beta^2}{\alpha^2} M_0$  where  $M_0$  is the explosion isotropic moment.  $M'_0$  is defined this way so that the function  $S_1^x$  does not depend explicitly on the material properties at the source depth. (More details are given in Stevens and McLaughlin (2001) and Stevens and Murphy (2001)).

### 3.3 Surface wave propagation in complex structures

In more complex structures, equations 3.1 and 3.2 may be inadequate to describe surface waves. In our experience, these approximations work very well for modeling surface wave dispersion and fairly well for modeling surface wave amplitude over most of the world. In this project, however, we are performing a more complete analysis including an approximation for the effects of scattering and diffraction. This is important for two reasons:

- 1) Some of the remaining residual in the global dispersion models is due to scattering and diffraction, and incorporation of these effects into our analysis may allow us to correct for them; and
- 2) To perform inversion of attenuation data for Q structure as described in the following section, we want to correct the amplitude for the effects of heterogeneous structure. The effect of heterogeneous structure on amplitude is stronger than on dispersion.

Modeling of scattering and diffraction is an active area of current research. Most of the research relevant to this project use variants of the single-scattering Born approximation to model the scattered wave field (Snieder, 1986). Zhou et al. (2004) summarize this work and derive

sensitivity kernels for phase, amplitude and arrival angle. The Born approximation models the observed surface wave at a receiver as a sum of a direct wave plus waves scattered from material inhomogeneities throughout the region.

Ritzwoller et al. (2002) used a simplified version of the Born approximation to include diffraction in surface wave tomography. They modeled the sensitivity kernel with a boxcar function the width of the Fresnel zone normal to the source to receiver path, then used an area integral over this region in place of the ray theory path integral for performing tomographic inversion. Yoshizawa and Kennett (2004) and Kennett and Yoshizawa (2002) use a similar technique with a narrower kernel that they believe to be more representative of realistic surface waves. Spetzler et al. (2001, 2002) discuss the implications of scattering and diffraction for surface wave tomography. Friedrich et al. (1993), Friedrich (1999) and Maupin (2001) extend the Born approximation to incorporate multiple scattering.

We implemented the algorithms of Zhou et al. (2004) for calculating finite frequency sensitivity kernels for dispersion and amplitude variations. Using the forward scattering, forward propagating approximation, the phase and amplitude corrections are:

$$\delta\phi = \iint K_{\phi}^c (\delta c/c) d\Omega, \text{ where } K_{\phi}^c = -\frac{2k^{3/2} \sin[k(\Delta' + \Delta'' - \Delta) + \pi/4]}{\sqrt{8\pi \sin \Delta' \sin \Delta'' / \sin \Delta}} \quad (3.3)$$

$$\delta \ln A = \iint K_A^c (\delta c/c) d\Omega, \text{ where } K_A^c = -\frac{2k^{3/2} \cos[k(\Delta' + \Delta'' - \Delta) + \pi/4]}{\sqrt{8\pi \sin \Delta' \sin \Delta'' / \sin \Delta}} \quad (3.4)$$

where distance is in radians,  $k$  is wavenumber, and  $\Delta'$ ,  $\Delta''$  and  $\Delta$  refer to the source to scatterer, scatterer to receiver, and source to receiver distances, respectively. The integrals run over the entire earth's surface, although in practice (and in this report) are limited to the first Fresnel zone, which is defined by  $k(\Delta' + \Delta'' - \Delta) < 3\pi/4$ . Phase and amplitude kernels at 12 seconds are shown in Figure 3.2. Dahlen and Zhou (2006) extend these equations to derive group delay and intrinsic attenuation kernels.

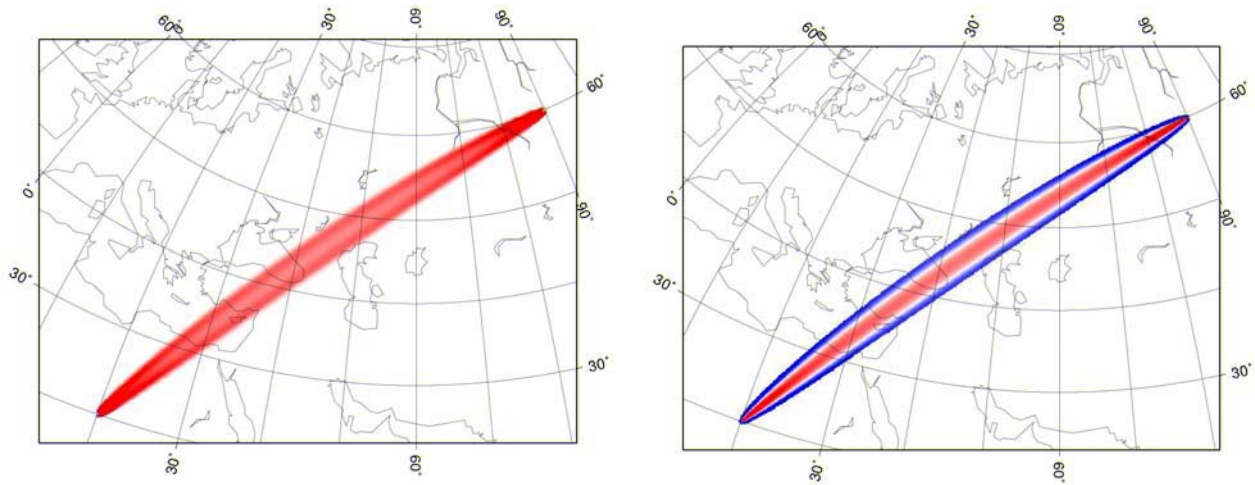


**Figure 3.2. 12 second phase velocity (left) and amplitude (right) kernels across central Asia.**

### 3.4 Application of corrections to surface wave amplitudes

We tested the algorithms described above using the one degree dispersion maps of Stevens et al. (2005). While the results are reasonable for prediction of dispersion variations, the predicted amplitude corrections seem unreasonably large, particularly on long paths. Consequently, we have performed some additional calculations and analysis to investigate how model roughness affects amplitudes. Figure 3.3 shows the 10 second phase velocity model for Eurasia; Figure 3.4 shows the predicted amplitude variation for paths through this region from the Lop Nor test site using the model shown in Figure 3.3 directly, and using a “smoothed” version of the amplitude variation in which the phase slowness was modeled with a bilinear function instead of discrete blocks. For both of the amplitude figures, the anomalies have been truncated where they exceed  $\log_{10}(\text{amplitude}) = 0.6$ . The amplitude variations become quite large on longer paths, and it does not appear that the Born approximation is giving reasonable answers on these paths.

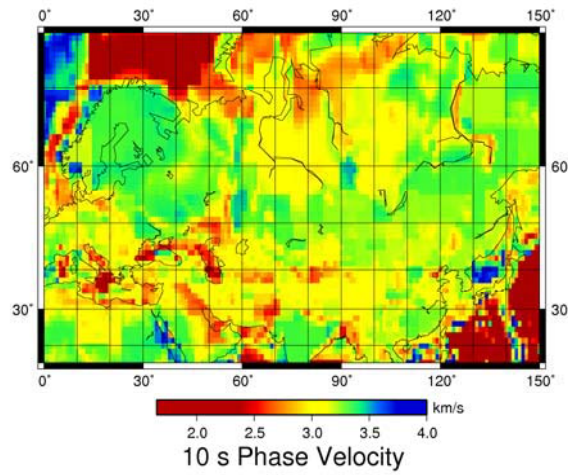


Figure 3.3. Eurasian phase velocity model at 10 seconds from Stevens et al. (2005).

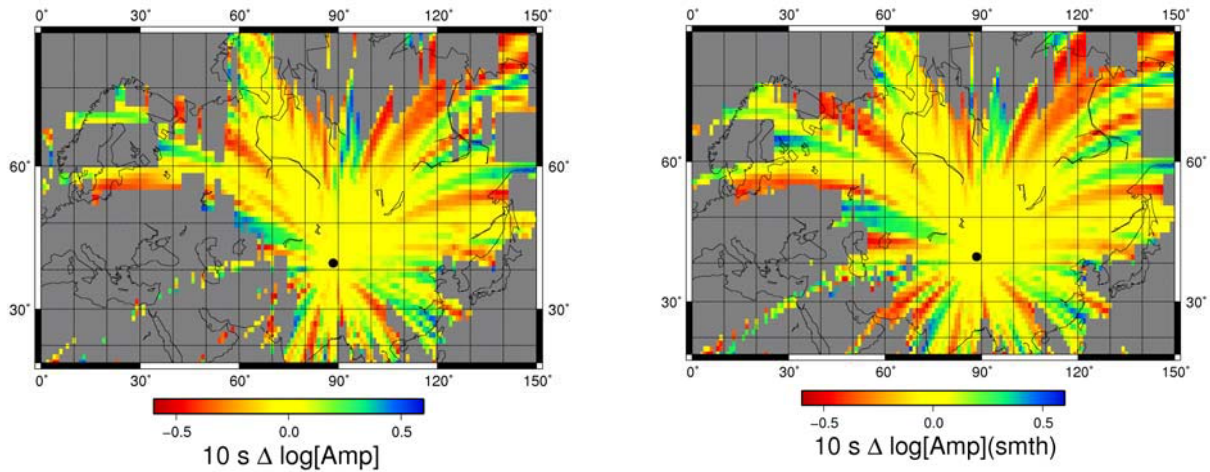
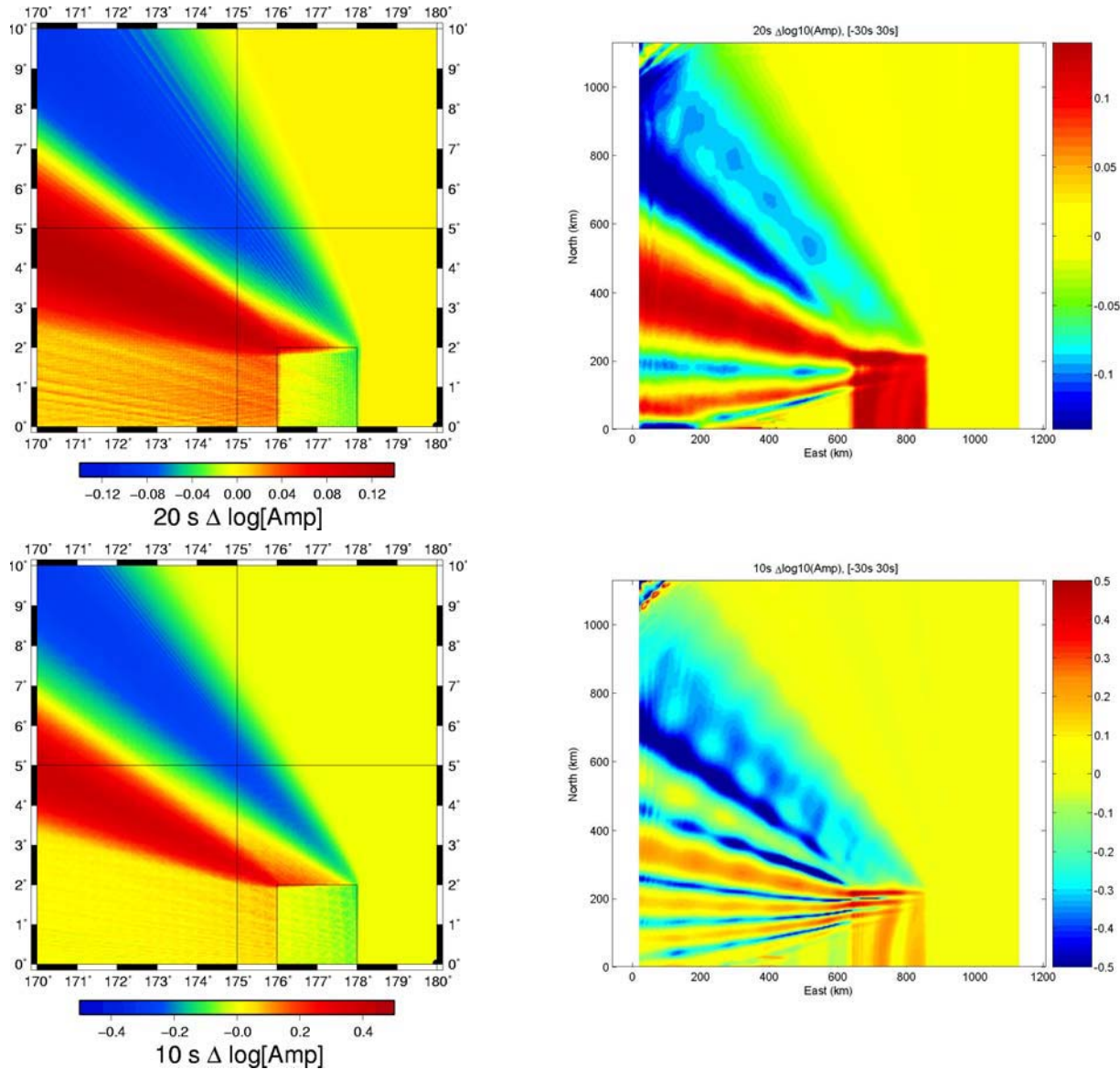


Figure 3.4. Left - predicted amplitude variations at 10 seconds through the phase velocity model of Figure 2 on paths out of Lop Nor. Right – same, but the velocity model has been smoothed by modeling it as a bilinear rather than piecewise discontinuous function.

In order to validate/correct the results, we need to determine whether the Born approximation is giving correct results for structural variations of the magnitude present in the Stevens et al. (2005) models, and at the frequencies of interest. To do this, we performed a test case of a structure for the Tarim Basin embedded in a uniform structure typical of shield regions of Eurasia, such as those that surround the Tarim Basin (Figure 3.5). We performed a Born approximation calculation and a 3D finite difference calculation for a source located just east of the Tarim Basin and examined the wavefield for several hundred km west of the Tarim Basin.



**Figure 3.5.** Comparison of Born approximation (left) with finite difference calculation (right) of amplitude perturbations at 20 seconds (top) and 10 seconds (bottom). The rectangular inclusion is modeled after the Tarim Basin structure, and the external structure after a Eurasian shield earth structure. The source is on the horizontal axis at the right edge of the plot. There is general agreement in the features of the two calculations. The amplitude is increased in a band above and to the left of the inclusion in both cases, and decreased above that. However, there are some interference effects in the finite difference calculation that are not reproduced in the Born calculation, and the patterns of high and low amplitudes do not match exactly.

The results showed that although the Born approximation is generally consistent with the finite difference results, there are noticeable interference effects leading to high and low amplitudes in the finite difference calculation that are not present in the Born approximation. The differences are significantly larger at 10 seconds than at 20 seconds.

One reason for this increase in complexity is illustrated in Figure 3.6. Propagation of the cylindrical wave leaving the source through the Tarim Basin model leads to a strong diffracted wave generated by the wavefront passing along the top of the Basin. This secondary wave interferes with the direct wave and complicates analysis, particularly in the interpretation of spectra. Since the first order Born approximation only models the direct wave, it cannot reproduce this strongly diffracted secondary wave, although it may do an adequate job of predicting the primary arrival. Also shown in Figure 3.6 are two observed waveforms that traveled through the Tarim Basin. There are two distinct surface wave arrivals similar to the figure on the left. Although we have not done sufficient analysis to say that the split in these seismograms was due to the effect illustrated in the left figure, it does suggest that strong diffraction may be responsible.

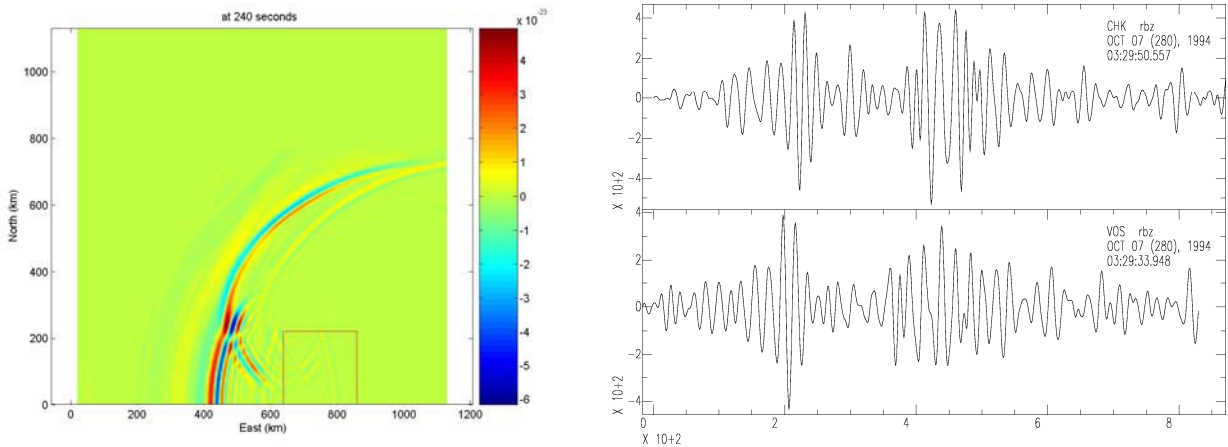


**Figure 3.6. Vertical component velocity after propagation across the low velocity basin (left). There is a strong diffracted wave that interferes with the direct wave. The right figure shows two observed waveforms that passed through the Tarim Basin and have two distinct surface wave arrivals.**

### 3.4 Analysis of surface waves at KNET propagating through and near the Tarim Basin

The Tarim Basin is a particularly troublesome region for surface wave propagation because of the presence of deep sediments with variable thickness (Figure 3.7). We examined surface waves in this region specifically to see if the kind of amplitude variations predicted by the Born approximation are observable here. Figure 3.7 shows the paths between events southeast of the Tarim Basin that were recorded at KNET. Figure 3.8 shows the seismograms recorded along these paths over three frequency bands, and Figure 3.9 shows the seismograms from the same events recorded along a northerly path that is much less complex. The seismograms do in fact show what we would expect: the paths through and near the Tarim Basin show much more complexity than the seismograms along the simpler paths. There is more variability at high frequency (10-20 seconds) and a strong amplification along the southernmost grazing path, similar to what we would expect from a seismogram in the red bands of amplification in Figure 3.5. So the seismograms are qualitatively similar to what is predicted by the Born approximation (or finite difference calculations) for a complex region. In the next section we examine the predictability of these amplitude variations.

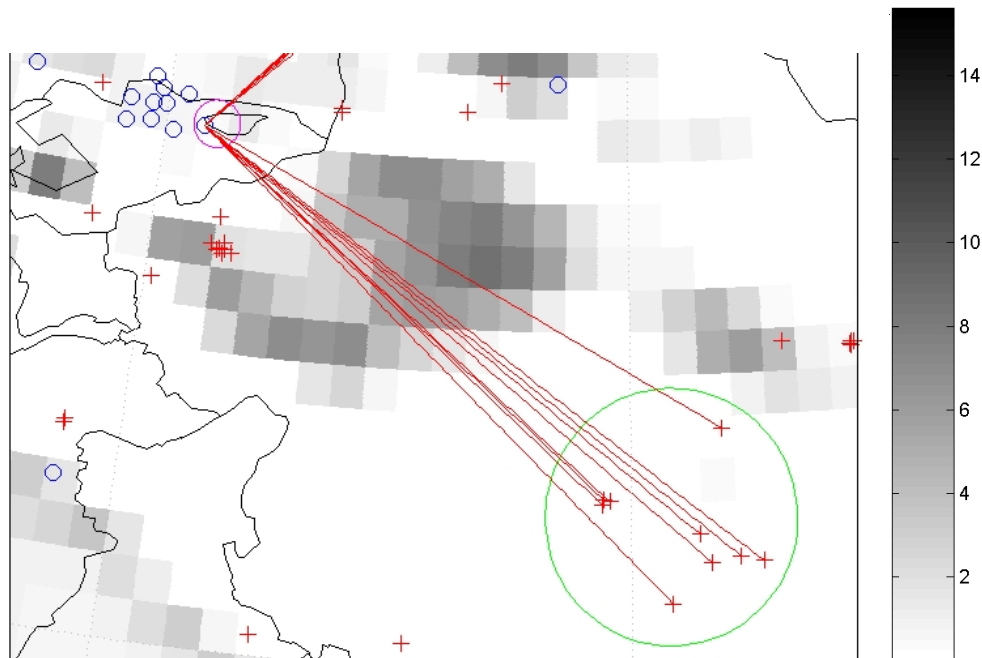


**Figure 3.7. Events within green circle (lower right) propagate at various distances in from the southern edge of the Tarim Basin to a KNET station (red lines). The northernmost event proved to have a complex source. All other events are shown, ordered by azimuth (northernmost path topmost), in the next two images. Scale indicates sediment thickness in km.**

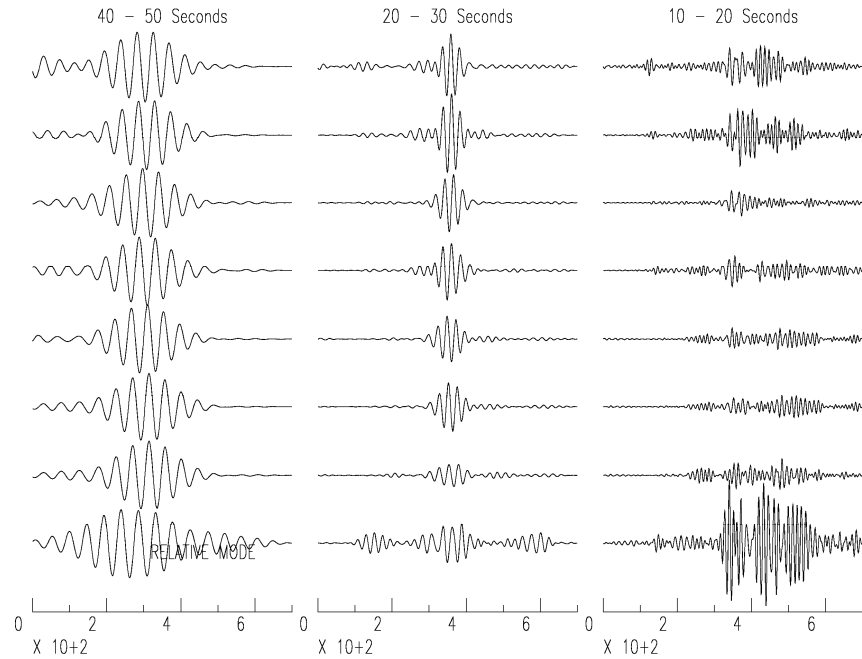


**Figure 3.8 KNET seismograms of the events with paths through the Tarim Basin. All records are normalized by the 40-50 second period surface wave amplitude. Amplitudes vary at higher frequency, as predicted by the simulations. The amplitude of the 10-20 second period surface wave from the event with the most glancing path becomes very large (bottom trace).**

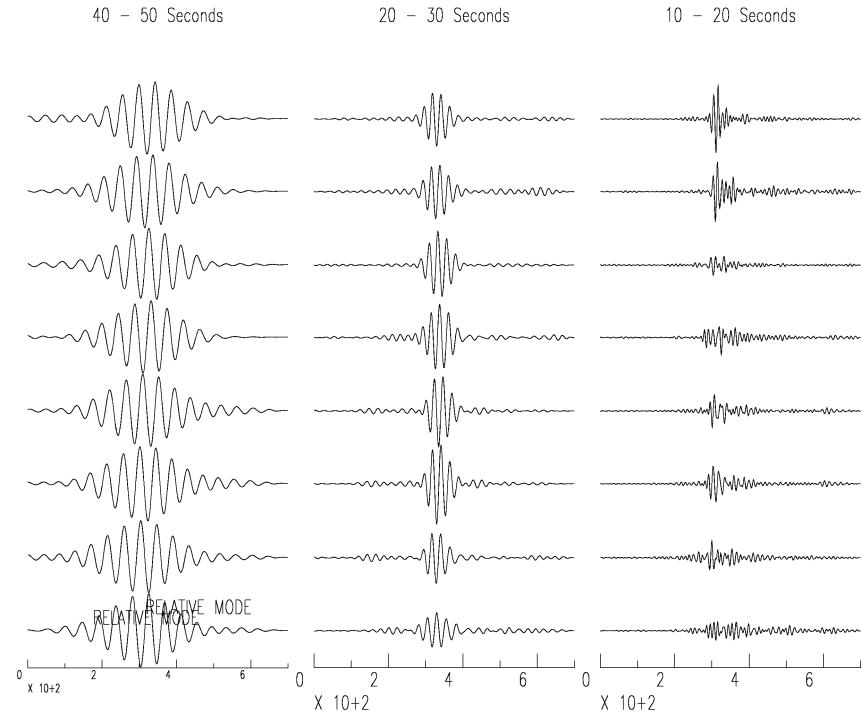


**Figure 3.9. Seismograms from the same events as the previous figure, in the same order and normalized by the 40-50 second surface wave amplitudes, but recorded at KMI (~130° azimuth, away from the Tarim Basin). The amplitudes are more consistent and waveforms much less complex, indicating that the amplitude variation and complexity observed at KNET can be attributed to the effects of the propagation near the basin boundary.**

### 3.5 Analysis of surface waves at KNET stations due to Lop Nor explosions

To assess the predictability of amplitude variations using the Born approximation, we calculated surface waves from several Lop Nor nuclear tests recorded at KNET with and without the Born approximation, and then also performed a large 3D finite difference calculation of the path between Lop Nor and KNET for comparison. The results for all of the Lop Nor tests are similar and we show one example in detail.

Figure 3.10 shows seismograms from the  $m_b$  5.94 June 8, 1996 explosion filtered from 0.01 to 0.1 Hz together with the paths taken between Lop Nor and KNET. Figure 3.11 shows uncorrected and path corrected spectra (see section 2) together with the predicted Born corrections for each path calculated using the earth models of Stevens et al. (2005). The path corrections do a fairly good job of flattening the spectra, and the Born corrections predict substantial variations in amplitude at higher frequencies that are not apparent in the data (note that the scales are different, however – the maximum Born correction is about a factor of 2, although since the corrections are additive, the negative corrections would be a more substantial change). Figure 3.12 shows synthetic seismograms calculated for the same paths with and without Born corrections. Although the Born corrections cause amplitude variations comparable to those observed, they do not cause them at the same stations. USP for example is predicted to be reduced substantially while the observed amplitude is relatively large. UCH is predicted to be large and observed to be small. Furthermore, none of the synthetics match the complexity of the observed waveforms. The predictive capability of the Born approximation does not appear to be very good for these complex paths.

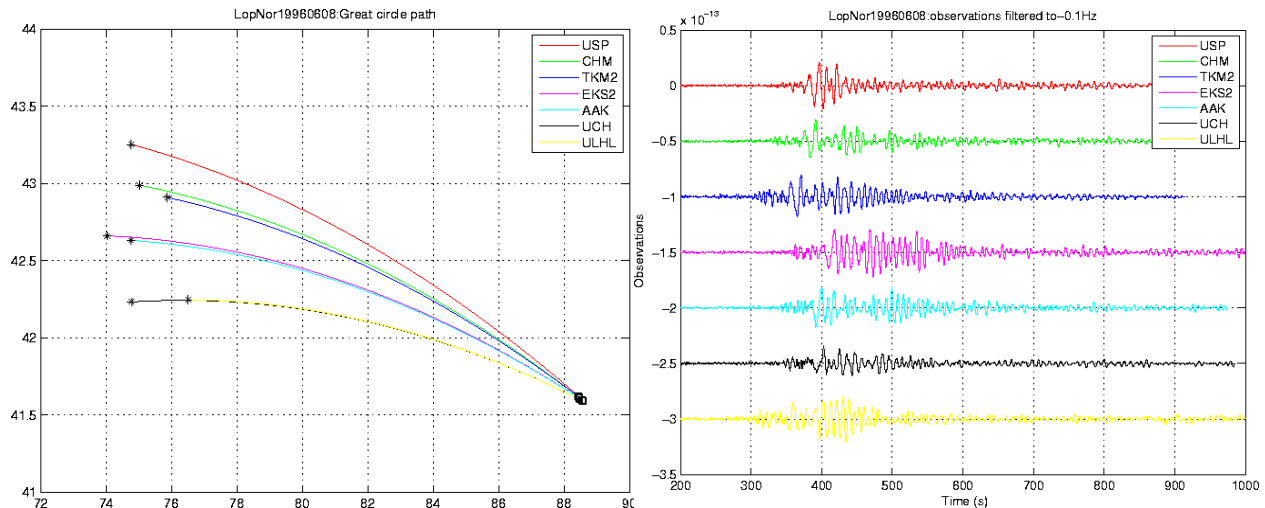


**Figure 3.10. Paths (top) and data (bottom) for the Lop Nor explosion of June 8, 1996. Data is filtered from 0.01 to 0.1 Hz.**

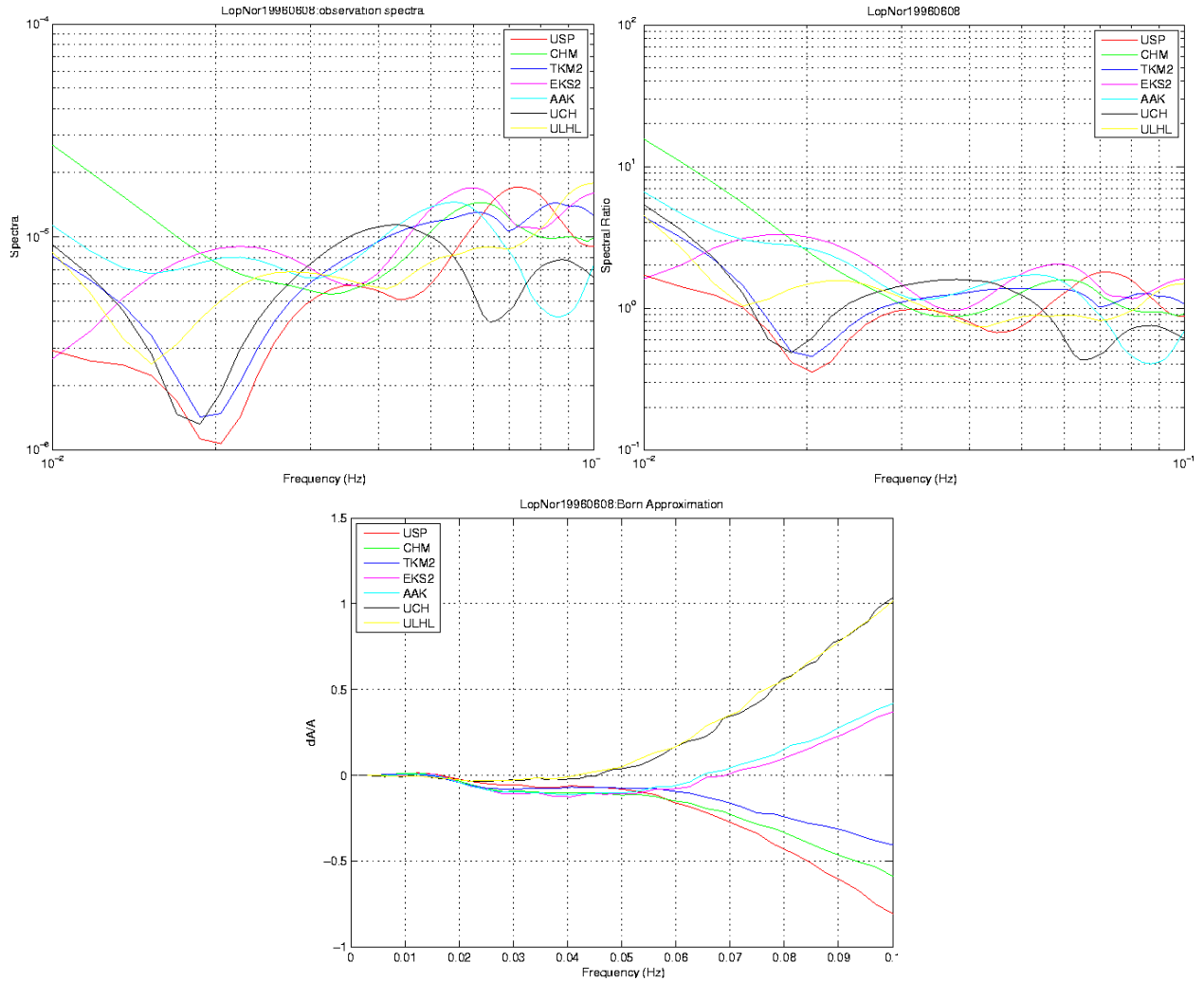


**Figure 3.11. Raw (upper left) and Path Corrected (upper right) Spectra for the Lop Nor explosion of June 8, 1996, and Born corrections (bottom) calculated for the same paths. Perfectly corrected spectra should be flat.**

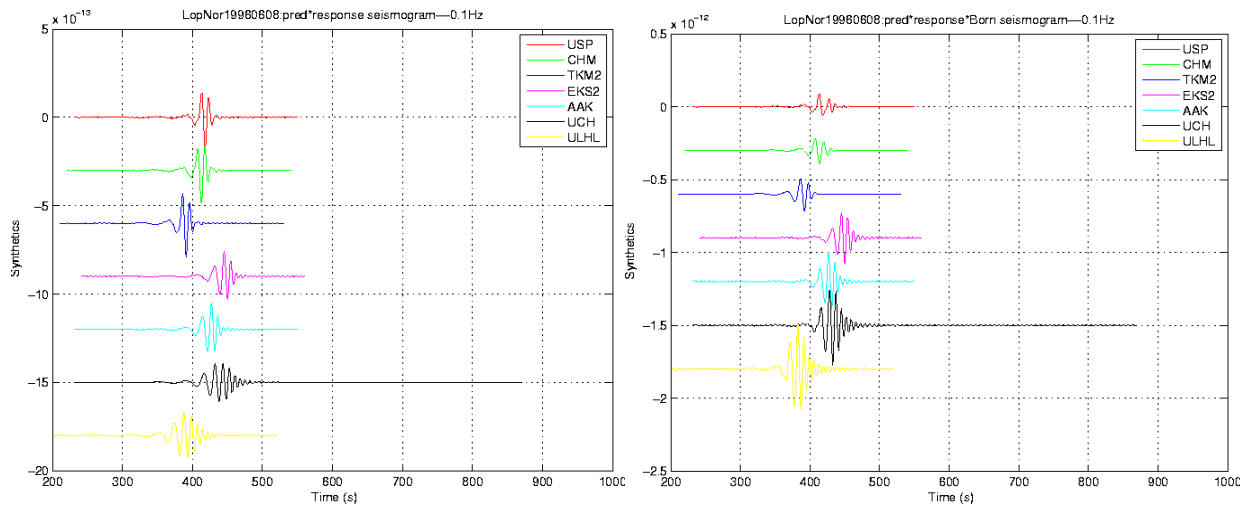


**Figure 3.12. Synthetic surface wave seismograms without (left) and with (right) Born corrections.**

### 3.6. 3D Calculations of Lop Nor to KNET and comparison with the Born approximation

We use the 3D elastic finite difference code TRES3D to calculate wave propagation in an earth model corresponding to the region between Lop Nor and KNET. We measured surface wave spectral amplitudes from the calculations using the same techniques used to measure observed surface waves: narrow-band filtering to construct a phase-matched filter followed by phase-matched filtering to isolate the surface wave (Stevens and McLaughlin, 2001). The numerical grid size is 678 (North) X 858 (East) X 202 (Depth) covering an area of approximately (36-48N) and (71.5-92.5E). The grid spacing in each dimension is 2km and time step is 0.12s.

The heterogeneous grid model is generated from the  $1^\circ \times 1^\circ$  global model of Stevens et al. (2005) and the homogeneous model is obtained at the LopNor (41.55N,88.70E) source site. No attenuation is included in the numerical calculations. The homogenous model is shown in Figure 3.13 and a slice through the heterogeneous model is shown in Figure 3.14.

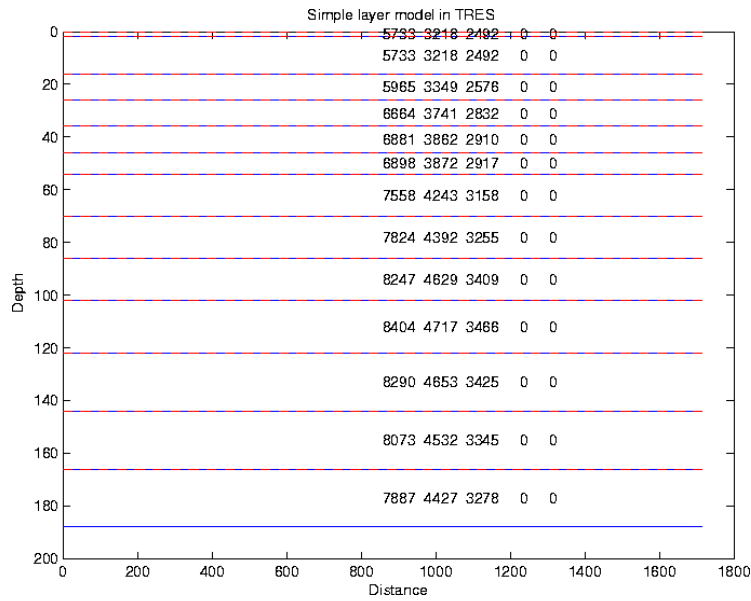


Figure 3.13. Homogeneous layered model. Numbers show Vp, Vs and density. Trailing zeros indicate infinite Q.

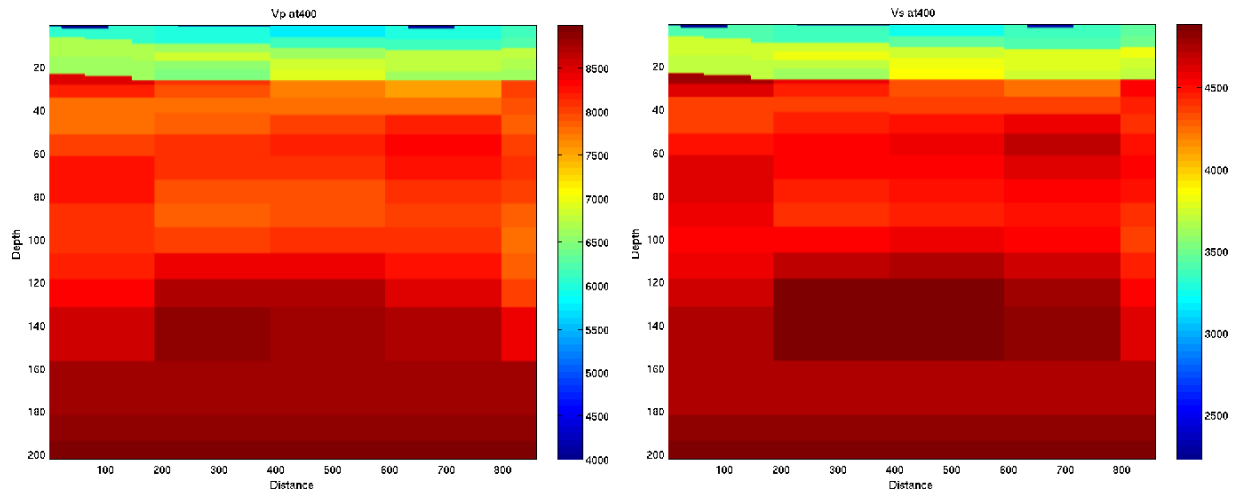
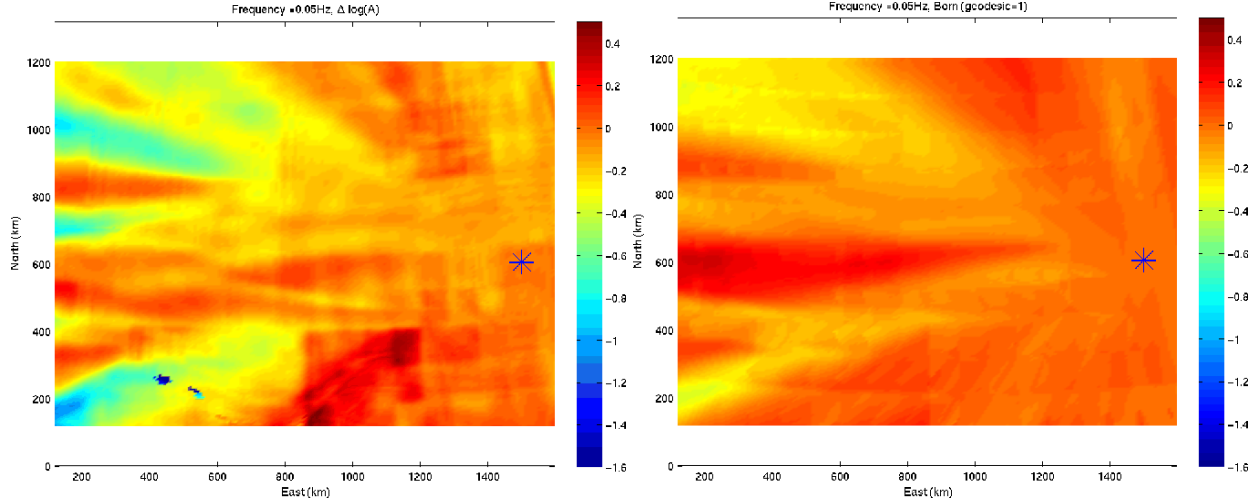
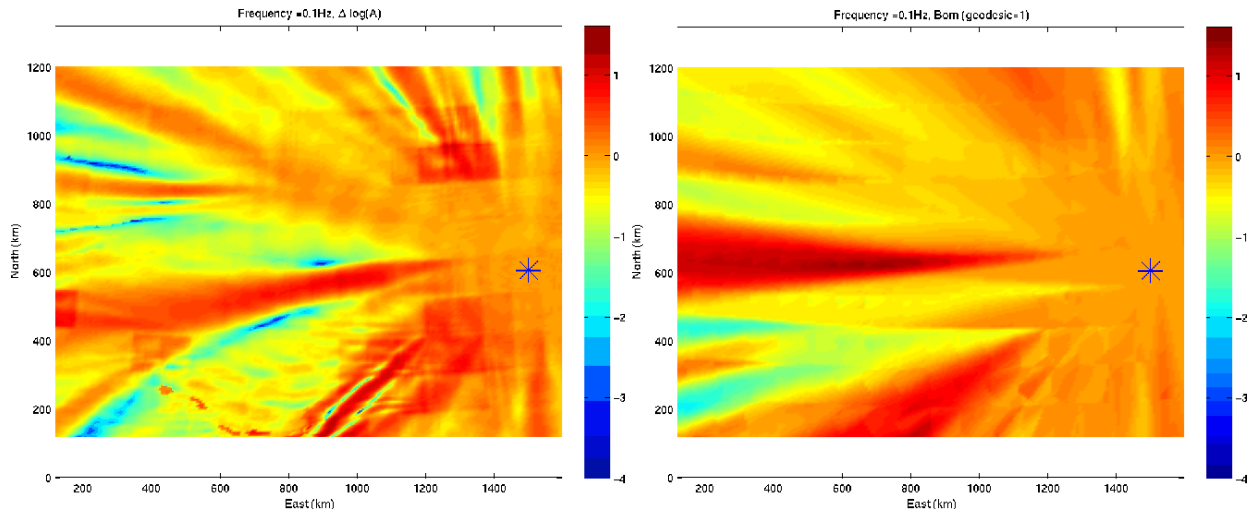


Figure 3.14. Heterogeneous model vertical profile of Vp (left) and Vs (right) at about 42N.

The calculated amplitude variations for an explosion at Lop Nor are shown in Figure 3.15 (20s) and Figure 3.16 (10s). The perturbation for the numerical calculations is  $\ln(A/A_0)$ ,  $A$  is the heterogeneous solution and  $A_0$  is the homogeneous solution. Both the numerical predictions and the theoretical predictions show complex variation patterns in comparison with those in a simple Tarim Basin model.



**Figure 3.15. Amplitude perturbations  $\ln(A/A_0)$  at 20 seconds for finite difference calculation (left) and Born approximation (right). The star is at the source location.**



**Figure 3.16. Amplitude perturbations  $\ln(A/A_0)$  at 10 seconds for finite difference calculation (left) and Born approximation (right). The star is at the source location.**

Although there are similarities between the finite difference solution and Born approximation, they clearly do not agree in detail, and so correcting the amplitude at a particular point may not give a more accurate result than an uncorrected amplitude, particularly at higher frequencies. For example, between 600 and 800 km north near the left edge of the grid, the Born approximation predicts strong signal enhancement, while the finite difference calculation shows amplitude reduction. Figure 3.17 shows snapshots of the vertical motion at 6 times, showing clearly how the wavefront bends irregularly and interferes with itself as it propagates. The dominant period band in the snapshots is 10-20 seconds.

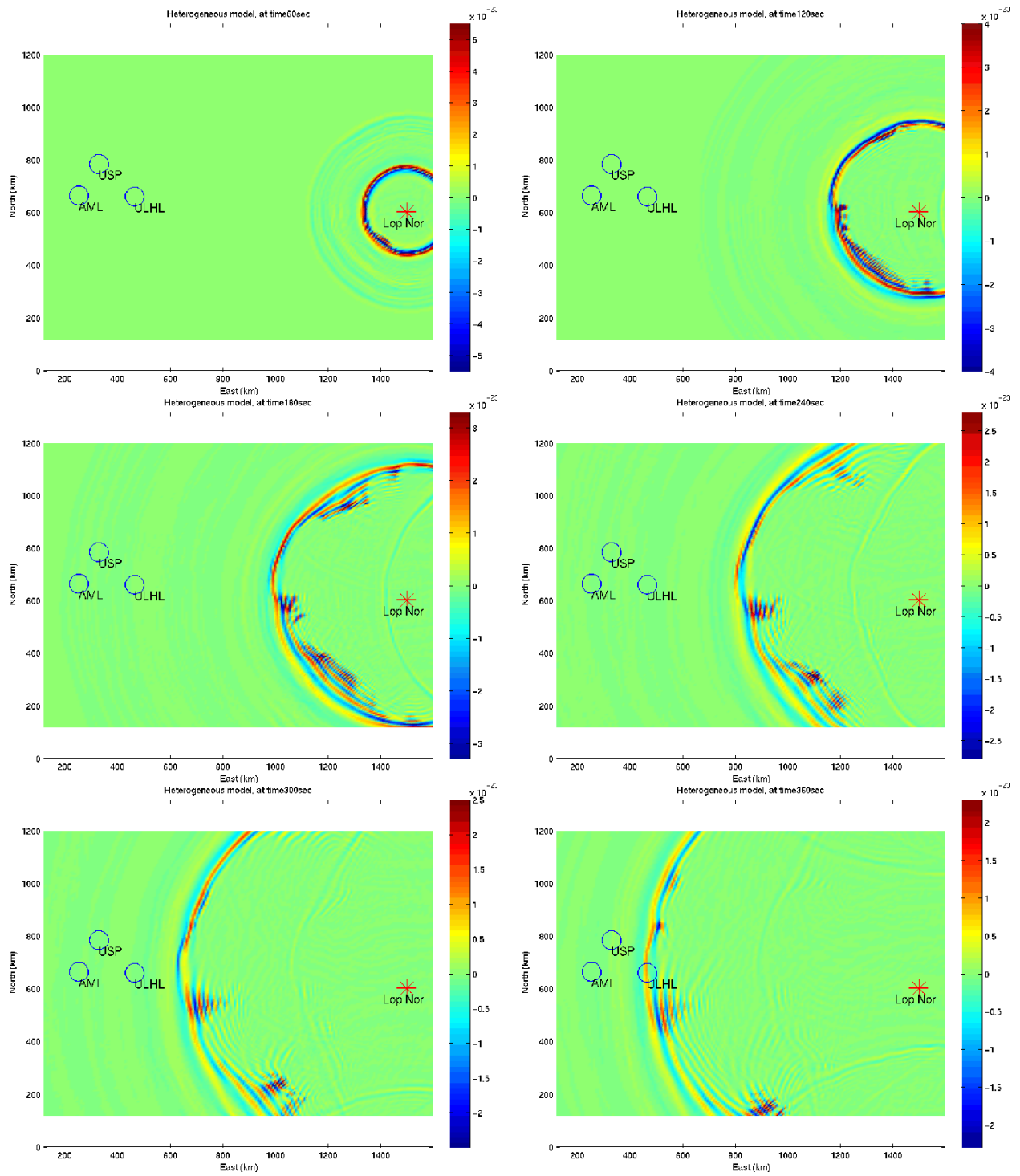


**Figure 3.17. Snapshots of vertical velocity propagating from Lop Nor to KNET for 3D finite difference calculation. Figures show snapshots at multiples of 60 seconds from 60 to 360 seconds. Amplitude scale range is proportional to  $1/t^{1/2}$ , which approximately corrects for surface wave geometric spreading.**

## 4.0 Inversion for Earth Structure and Attenuation

### 4.1 The inversion procedure for a 3D earth model

In our previous projects, we inverted a large volume of dispersion data for global earth structure. Global earth structure refers to a set of vertically layered earth models defined for each cell of a one-degree by one-degree grid of the earth. This procedure is summarized here, and in the following sections we show how it is modified to include scattering and diffraction and modified to invert attenuation data for global Q structure. The relationship between dispersion and the shear wave velocities of the layers in the earth model is non-linear, so the shear velocities are estimated by an iterative least squares inversion procedure. At each step a system of equations is formed, augmented by additional equations of constraint, and then solved by the LSQR algorithm (Nolet, 1987). The equations solved are

$$\begin{pmatrix} A \\ sH \\ \lambda I \end{pmatrix} \overrightarrow{\Delta x} = \begin{pmatrix} \overrightarrow{\Delta d} \\ -sH\bar{x} \\ \lambda(\bar{x}_c - \bar{x}) \end{pmatrix} + \bar{\epsilon} \quad , \quad (4.1)$$

where  $\Delta \mathbf{x}$  is the vector of adjustments to the shear wave slownesses of layers in each of the 577 model types.  $\Delta \mathbf{d}$  is the vector of slowness differences between predicted and observed dispersion measurements.  $\bar{\epsilon}$  is the vector of residuals that remain after inversion (the inversion minimizes  $|\bar{\epsilon}|$ ).  $\bar{\mathbf{x}}$  is the vector of slownesses estimated in the previous iteration. The elements of the matrix  $\mathbf{A}$  consist of partial derivatives of dispersion predictions with respect to shear wave slownesses in each layer.  $\mathbf{H}$  is a difference operator that applies to vertically neighboring layers and has the effect of constraining the vertical smoothness of velocity profile.  $\mathbf{H}$  applies to layers in the crust and upper mantle, but has explicit discontinuities at the crust/mantle boundary and at the base of surface sediments.  $s$  is the weighting of the smoothness constraint and can be a diagonal matrix (for variably weighted smoothing) or a scalar (constant smoothing).  $\mathbf{I}$  is the identity matrix and  $\lambda$  weights the damping which constrains the norm of the difference between final slownesses and constraining model slownesses  $\mathbf{x}_c$  (in this case a variant of the Crust 2.0 values).  $\lambda$  can be a scalar for constant damping, or a diagonal matrix for variable damping.

### 4.2 Correction for scattering and diffraction due to a realistic heterogeneous earth model

The Born approximation techniques discussed in section 3 provide a straightforward, but approximate, way to incorporate scattering and diffraction into the inversion procedure. As described above, the matrix  $\mathbf{A}$  in equation 4.1 is calculated using a path integral to calculate the phase velocity, with each element of the matrix corresponding to a piece of the path weighted according to the fraction of the path crossing a grid block and the sensitivity of the observable to the model velocity. This can be replaced by integration over the Fresnel zone area, which changes the weighting of each element and increases the number of elements corresponding to each ray. The matrix requires more time to calculate, but the inversion procedure is the same as in the ray-based tomographic inversion. We use this approach for inversion of dispersion data for earth structure. For amplitudes, we use the earth model determined by inversion of dispersion data to calculate amplitude corrections using the Born approximation and then apply these to the data prior to inverting for Q structure, which is then done using path integrals.

### 4.3 Application of corrections to inversion for earth structure

We ran our earth structure inversion using Born corrections for scattering and diffraction by incorporating the finite frequency sensitivity kernel (equation 3.3) into the inversion code. We then reran the entire global tomographic inversion of approximately one million dispersion measurements (Stevens et al., 2005) to generate a new set of earth structures. We found that the changes from the previous inversion are small in most areas, and there is no significant improvement in data fit, so it is not clear that the results represent an improvement over the inversion using great circle paths. Because the differences were so small, we used the existing structures as the base models for Q inversion.

### 4.4 Inversion of attenuation data for Q structure

Inversion of attenuation data for Q structure can be accomplished using equation 4.2, which has the same form as equation 4.1 above:

$$\begin{pmatrix} A \\ sH \\ \lambda I \end{pmatrix} \overline{\Delta x} = \begin{pmatrix} \overline{\Delta d} \\ -sH\bar{x} \\ \lambda(\bar{x}_c - \bar{x}) \end{pmatrix} + \bar{\epsilon} \quad (4.2)$$

with the following changes:

1. The data are attenuation residuals instead of dispersion residuals. Attenuation estimates are derived from an existing Q model, and the differences between those and the observations are the data used in the inversion. Amplitude measurements may be corrected for the effects of heterogeneous structure.
2. The matrix A is derived from derivatives of the attenuation coefficients with respect to model Q in each layer for the path-averaged inversion, and includes Born scattering sensitivity functions for the area integrals.
3. The starting model and constraining model are the same, and are derived from PREM for depths greater than 100 km, and Swanger's Law ( $Q=100\beta$ , with  $\beta$  in km/s) for shallower depths. The values derived from PREM are  $Q=18\beta$  for depths between 100 km and 220 km,  $Q=30\beta$  at greater depths. There are discontinuities at 100 km and 220 km and a smoothness criterion is applied to layers above and below 100 km. The inversion is performed for layers shallower than 220 km. Q is fixed to  $18\beta$  at 220 km depth and to  $30\beta$  below this depth.
4. The model vector consists of  $\beta/Q$  for each layer that is free to change in each structure, and optionally can include the change in moment of each event. That is, for attenuation residuals that were derived using spectra with a fixed model moment, the moment for each event can be corrected as part of the inversion.

Unlike inversion for shear velocity, the inversion for Q is linear, so only a single iteration is necessary, although multiple inversions are done with different damping and smoothing parameters to generate realistic models. Note that equations 3.1 and 3.2 give the equation for the predicted surface wave spectral amplitudes given a source mechanism for the event. Equation 3.4 can optionally be used to correct for structural heterogeneity using the Born approximation. Collecting the distance independent terms, equations 3.1 and 3.2 can be written in the form:

$$|u_z(\omega, r)| = M_0 \frac{S(\omega)A(\omega) \exp[-\gamma_p(\omega)r]}{\sqrt{a_e \sin(r/a_e)}} \quad (4.3)$$

where  $M_0$  is the source moment and  $S(\omega)$  the source function (important for large events),  $A(\omega)$  is a frequency dependent function that depends on source and receiver structure and focal mechanism. We assume that  $A(\omega)$  can be predicted well enough from the background earth structure and the source mechanism which is either a point explosion or CMT moment tensor. While the inversion program has the capability to allow an amplitude scale factor for each path, which would allow to variations in explosion amplitude due to tectonic release, and variations in earthquake amplitude due to errors in source mechanism, in the inversions that follow we only allowed the moment to vary, which is a constant factor for all paths for a single event. In equation 4.3,  $M_0$  and  $\gamma_p$  are derived from a starting source mechanism and background earth model, and allowed to vary in the inversion while the other factors are held fixed.  $S(\omega)$  is derived for a triangular function with rise time (half-duration)  $T$ . Since this is approximate, points where  $fT > 0.5$ , which corresponds to an amplitude reduction of 0.4, are zero weighted. The observed data can then be written:

$$|u_z^o(\omega, r)| = M_0^o \frac{S(\omega)A(\omega) \exp[-\gamma_p^o(\omega)r]}{\sqrt{a_e \sin(r/a_e)}} \quad (4.4)$$

And the log ratio of observed to predicted spectra has the form:

$$\ln \left| \frac{u_z^o(\omega, r)}{u_z(\omega, r)} \right| = \ln \frac{M_0^o}{M_0} + [\gamma_p(\omega)r - \gamma_p^o(\omega)r] = \Delta \ln M_0 + r\Delta\gamma \quad (4.5)$$

$\Delta\gamma$  can be further expanded into a sum over Q structure in each structure traversed by the ray along the source to receiver point multiplied by the fraction of ray over each structure. So we can rewrite equation 4.5 as:

$$\frac{1}{r_{ik}} \ln \left| \frac{u_z^o(\omega, r)}{u_z(\omega, r)} \right|_{ik} = \frac{1}{r_{ik}} \Delta \ln M_0^k + \sum_{l=1}^L \frac{\Delta r_{lik}}{r_{ik}} \sum_{j=1}^J G_{lj} \Delta \left( \frac{\beta}{Q} \right)_{lj} \quad (4.6)$$

The subscript k refers to an event, i refers to a single path for event k, l refers to each model type traversed by the ray and  $\Delta r_{lik}/r_{ik}$  is the fraction of the path that the ray spends in each model. The subscript j refers to layer number in each model. L is the total number of model types traversed and J is the total number of layers allowed to change in each model. So the data in the inversion is the left hand side of equation 4.6, the spectral ratio divided by the distance for multiple frequencies, and the inversion is performed for the quantities  $\Delta \ln M_0^k$ , the change in moment of each event, and  $\Delta(\beta/Q)_{lj}$ , the ratio of shear velocity to Q in each layer of each model. The function  $G_{lj}$  gives the change in  $\gamma$  with respect to change in  $\beta/Q$  and can be written assuming no bulk attenuation in terms of partial derivatives of phase velocity with respect to material velocities as:

$$G_{lj} = \frac{\partial c_l}{\partial \beta_{lj}} + \frac{4}{3} \frac{\beta_{lj}}{\alpha_{lj}} \frac{\partial c_l}{\partial \alpha_{lj}} \quad (4.7)$$

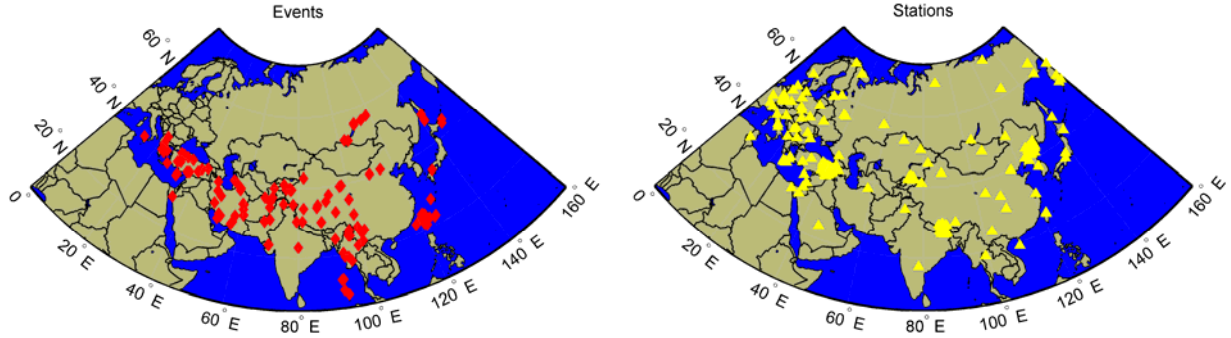
The inversions described below all invert data of the form described above. We also compare with interstation attenuation estimates. Using equation 4.5 again at two or more stations at distances  $r_n$ , we get a set of equations of the form:

$$\ln \left| \frac{u_z^o(\omega, r_n)}{u_z(\omega, r_n)} \right| = \Delta \ln M_0 + r_n \Delta \gamma \quad (4.8)$$

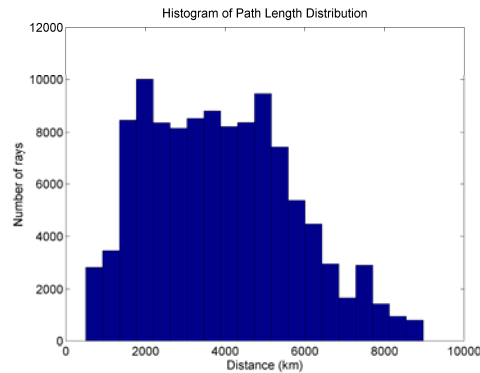
The equations define a line with slope  $\Delta \gamma$  and intercept  $\Delta \ln M_0$  so this can be used as a check on the inversion by finding the average change in attenuation over all or a subset of paths for each event, and the change in moment.

#### 4.5 Data used in the Q Inversion

We used two sets of data in our Q inversion. The first data set was provided to us by Anatoli Levshin of the University of Colorado and is described in Levshin et al. (2007). They used essentially the same procedure described above, determining gamma from equation 4.8, except that they allowed the moment, depth and fault orientation to vary in order to determine more realistic attenuation coefficients. The second set of data consisted of our own measurements on a different set of data also covering the Eurasian continent. The events processed are listed in Appendix A and the events and recording stations are shown in Figure 4.1. Figure 4.2 shows a histogram of path lengths in the complete data set. As discussed above, we determined attenuation coefficients using CMT moments, but then allowed the moments to vary as part of the inversion process. There is quite a lot of scatter in both data sets, and we rely on data redundancy to help define the attenuation model.

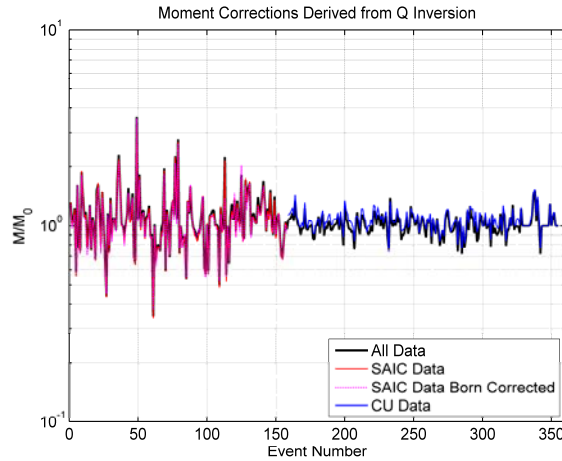


**Figure 4.1** Maps showing events processed (left) and stations recording data from these events (right).



**Figure 4.2.** Histogram of distances of all rays in the data set. Each frequency is considered distinct in this plot.

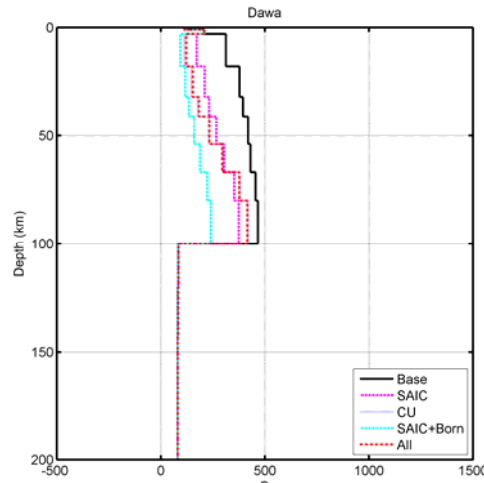
Four separate inversions were performed with the following data sets: 1) SAIC data, 2) SAIC data with Born corrections applied, 3) CU data, and 4) CU and SAIC data combined. Figure 4.3 shows the change in moment determined as part of the inversion. Since the CU data was moment corrected prior to inversion, the change in moment for that data set is quite small. The variation in moment for the SAIC data is similar to that described by Levshin et al. (2007).



**Figure 4.3.** Change in moment for each event processed. “All Data” refers to inversion of the SAIC and CU data simultaneously while the other data sets were inverted independently. Inversion of all data together gives very similar results to inversion of individual data sets. Application of Born corrections also makes little difference to the moment corrections.

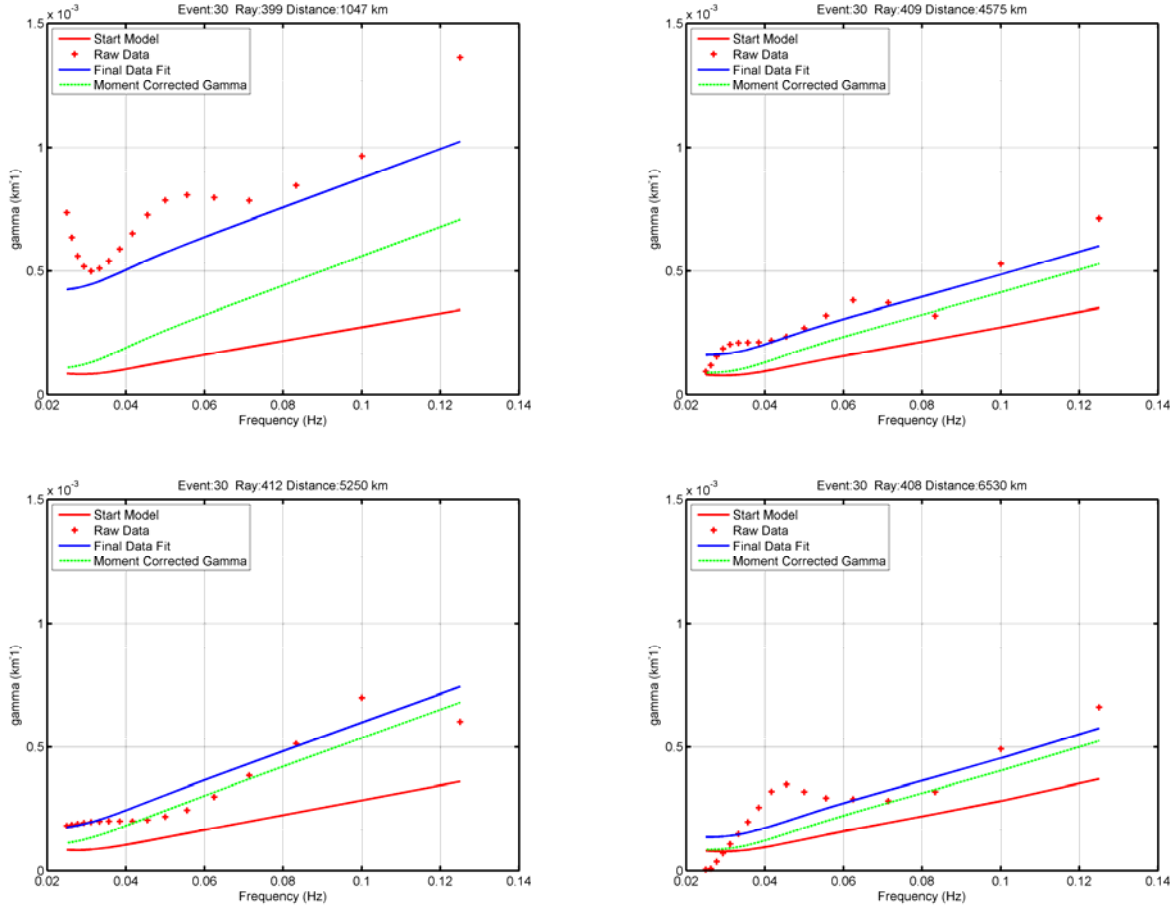
#### 4.6 Q Inversion Results

Inversion results were evaluated by examining the models and the data fit. The models were initially inverted with the same damping and smoothing factors for all models. Then the post-inversion models were examined to look for problems. The most common problem is negative Q values which are a sign of underdamping of the inversion. The damping and smoothing parameters were both increased by the same amount for these models and the inversion rerun until models were all physically reasonable. Figure 4.4 shows an example of the initial model and final models for each data set.



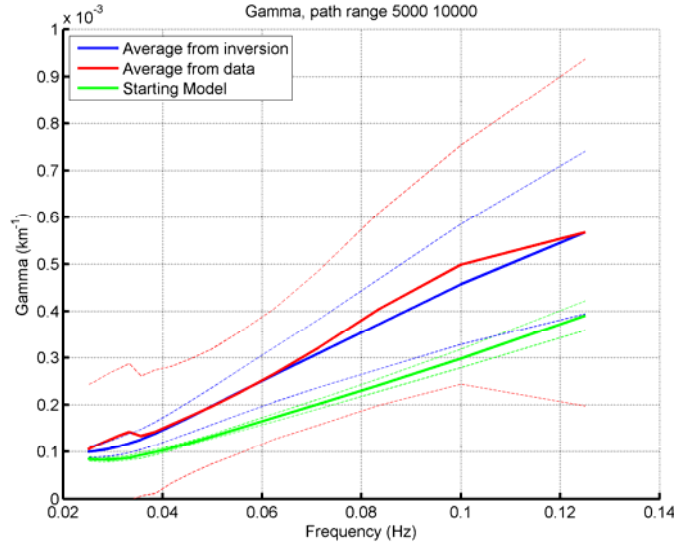
**Figure 4.4** Comparison of inversion results with base model for one central Asian structure. In this case, all data sets show lower Q, with the Born adjusted data set showing a larger change.

The second check on the inversion was examination of data fit. This was done both for individual models and for averages over all data. Because of the large variability in the data, we typically get good data fits for some paths for each event, and some that are not in good agreement with the data, however for each event we generally have good data fits for most paths. Figure 4.5 shows examples for a few paths for one event. Figure 4.6-4.8 show examples for averages along many paths.



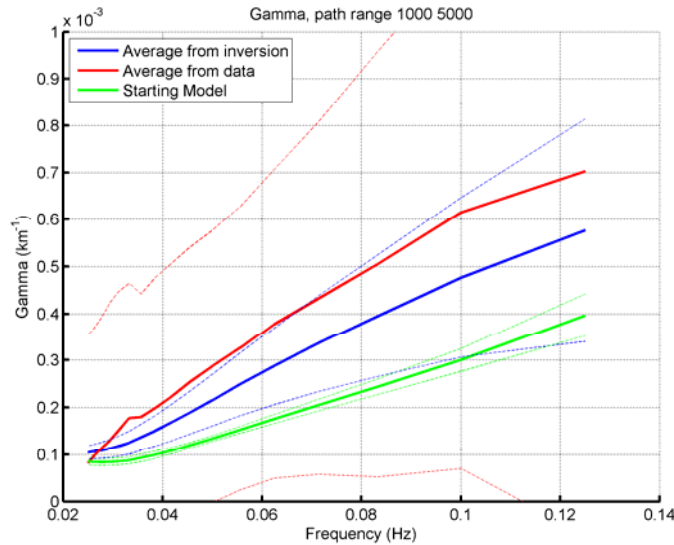
**Figure 4.5.** Data fits for four paths of different ranges for the same event. The red line is the starting model and the green line the final gamma model. The blue line corresponds to the data fit and is the green line shifted by an amount corresponding to the moment adjustment. This adjustment is larger at closer distances. The red marks are the data points.

Figure 4.6 shows the average of the data over all paths longer than 5000 km, the inversion results for the same paths, and the starting model for the same paths. Both the data and the inversion results show substantially higher attenuation than in the starting model. The average inversion results are a very good fit to the average data. The results suggest that a background model with  $Q=70\beta$  in the crust and upper mantle would be more consistent with the data than our starting model with  $Q=100\beta$ .



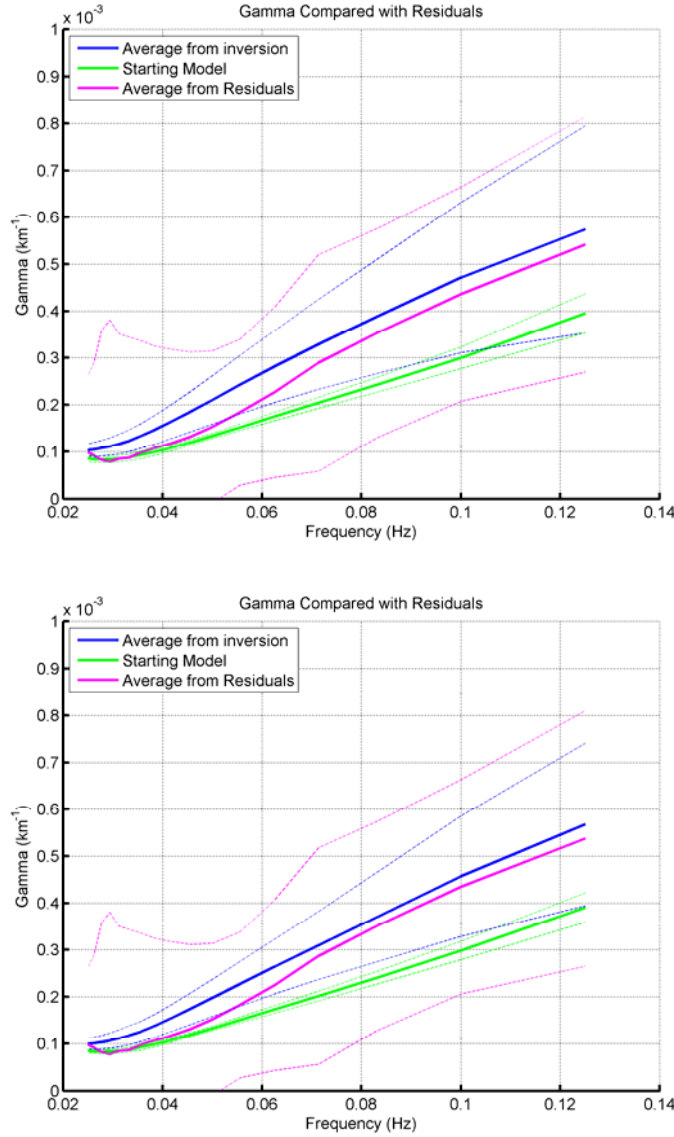
**Figure 4.6.** Average gamma for all paths after inversion (blue), in original data set (red) and starting model (green). Dashed lines are  $\pm 1$  standard deviation. For paths between 5000 and 10,000 km.

Figure 4.7 shows the average over paths shorter than 5000 km of the data, the inversion results for the same paths, and the starting model for the same paths. The attenuation is higher along these shorter paths, but the scatter in the data is also much larger, as indicated by the wide standard deviations on the plot.



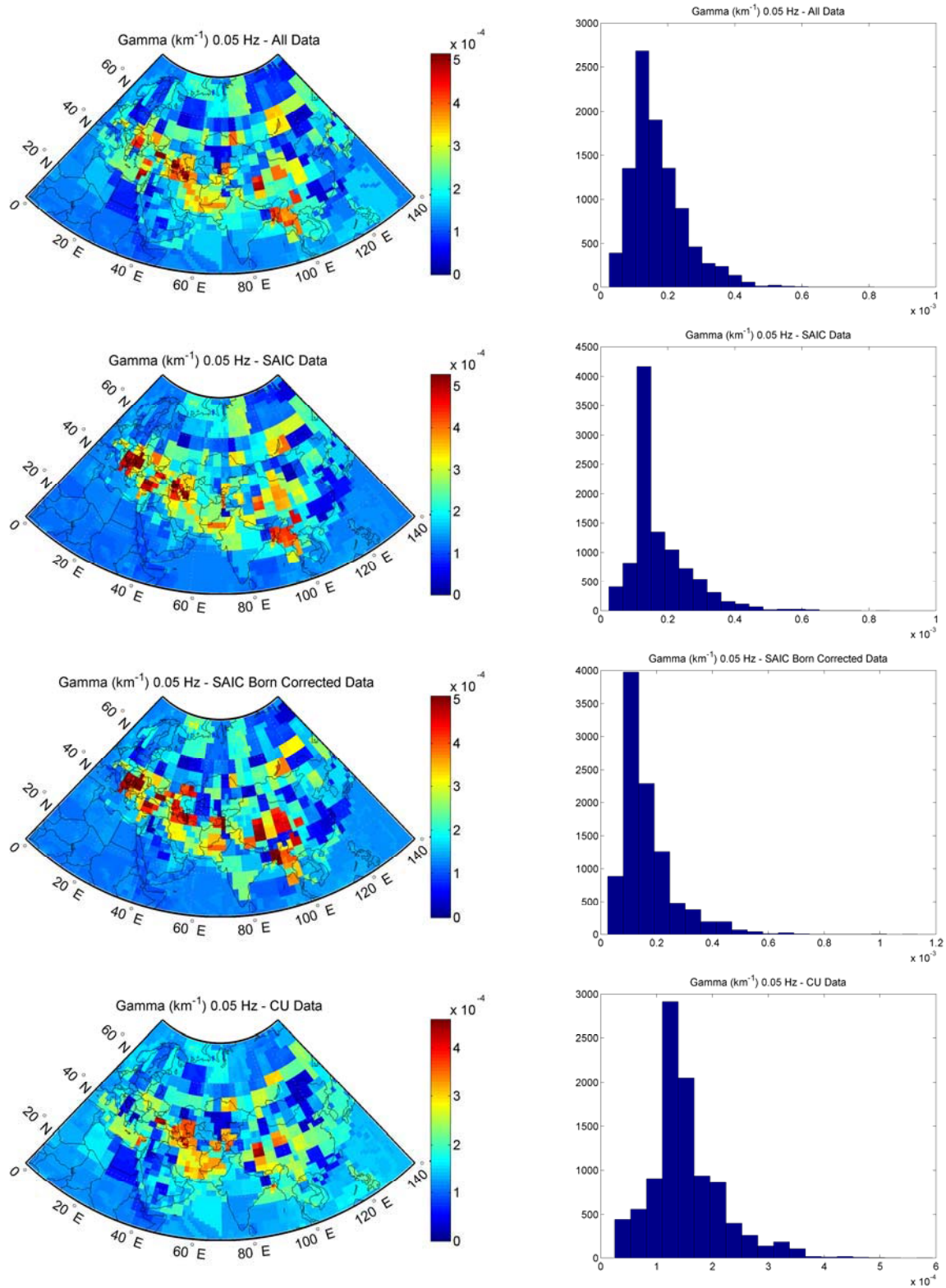
**Figure 4.7.** Average gamma for all paths after inversion (blue), in original data set (red) and starting model (green). Dashed lines are  $\pm 1$  standard deviation. For paths between 1000 and 5,000 km.

Figure 4.8 shows the average over all paths longer than 1000 km and for all paths longer than 5000 km for the inversion results and the starting model for the same paths. Now we also compare with the observed amplitude decay along all paths for each event. The attenuation determined from amplitude decay is slightly smaller than determined from the inversion results, but well within the scatter in the data, and both are substantially higher than the starting model, particularly at higher frequencies.



**Figure 4.8.** Average gamma for all paths after inversion (blue), in starting model (green), and as determined by amplitude decay along all paths for each event (red). Dashed lines are  $\pm 1$  standard deviation. Average gamma and starting model are for paths in the data set longer than 1000 km (top) and longer than 5000 km (bottom).

Figures 4.9-4.14 show the inversion results at frequencies of 0.05, 0.067, 0.08, 0.1, 0.125 and 0.15 Hz. Each plot shows a map of inversion results in Eurasia and a histogram of attenuation values for each frequency. The results from the different data sets differ in some details, but are similar in most respects. All show a band of high attenuation stretching across Asia from the Middle East through Southeast Asia.



**Figure 4.9. Attenuation inversion results at 20 seconds – left: gamma map, right: gamma histogram.**  
**Inversion data sets from top to bottom: All data, SAIC data, SAIC data Born Corrected, CU.**

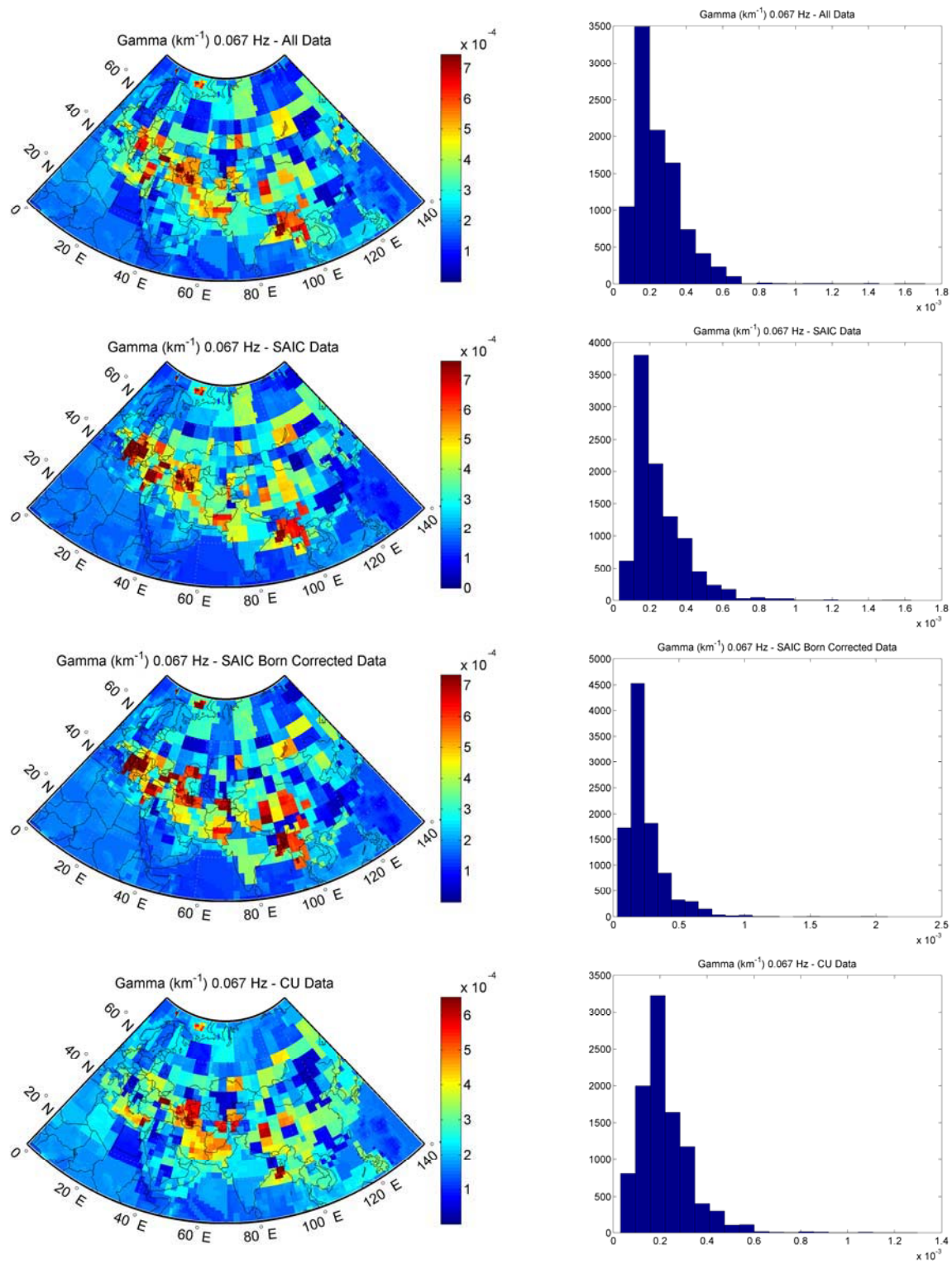


Figure 4.10 Attenuation inversion results at 15 seconds – left: gamma map, right: gamma histogram.

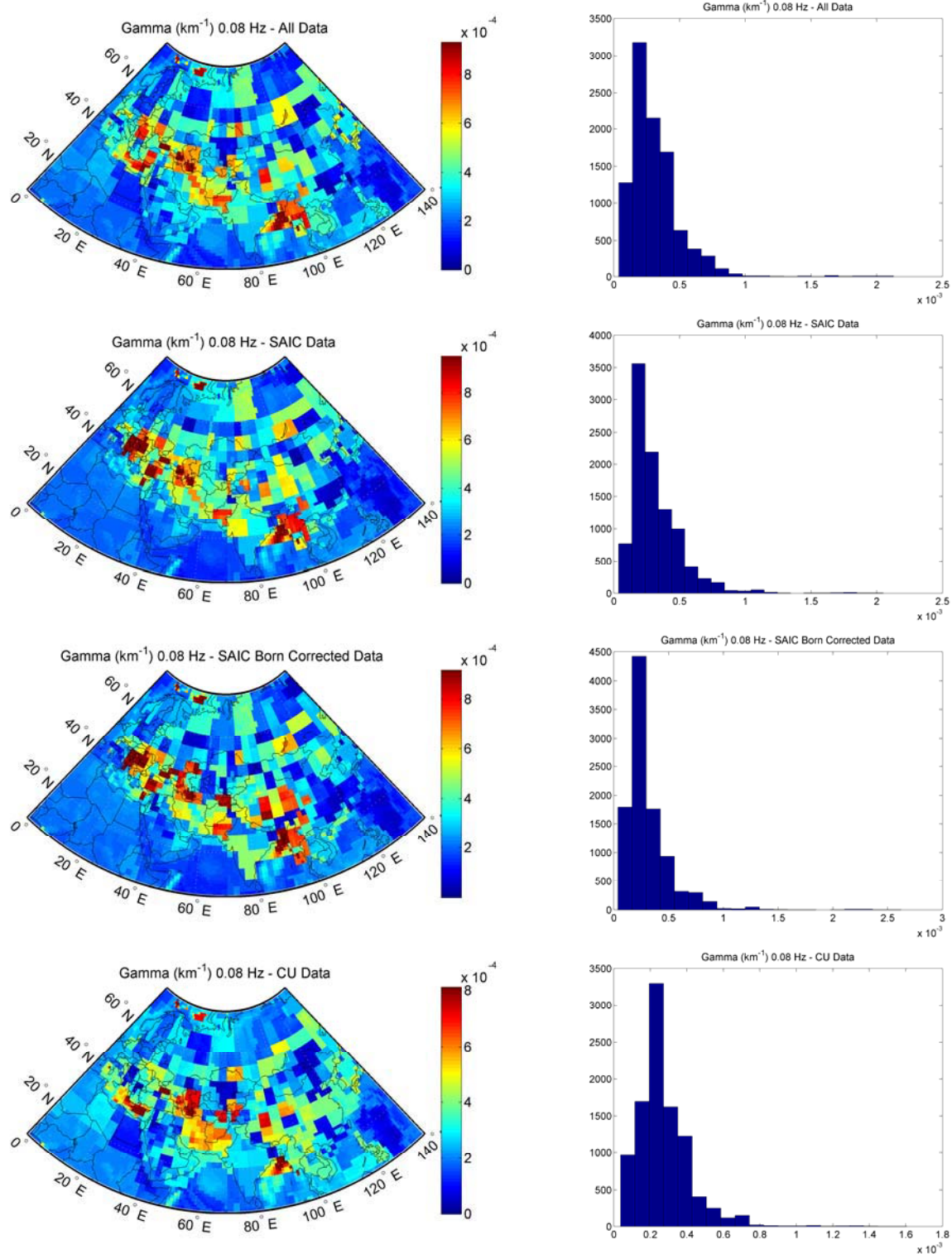


Figure 4.11. Attenuation inversion results at 12.5 seconds – left: gamma map, right: gamma histogram.

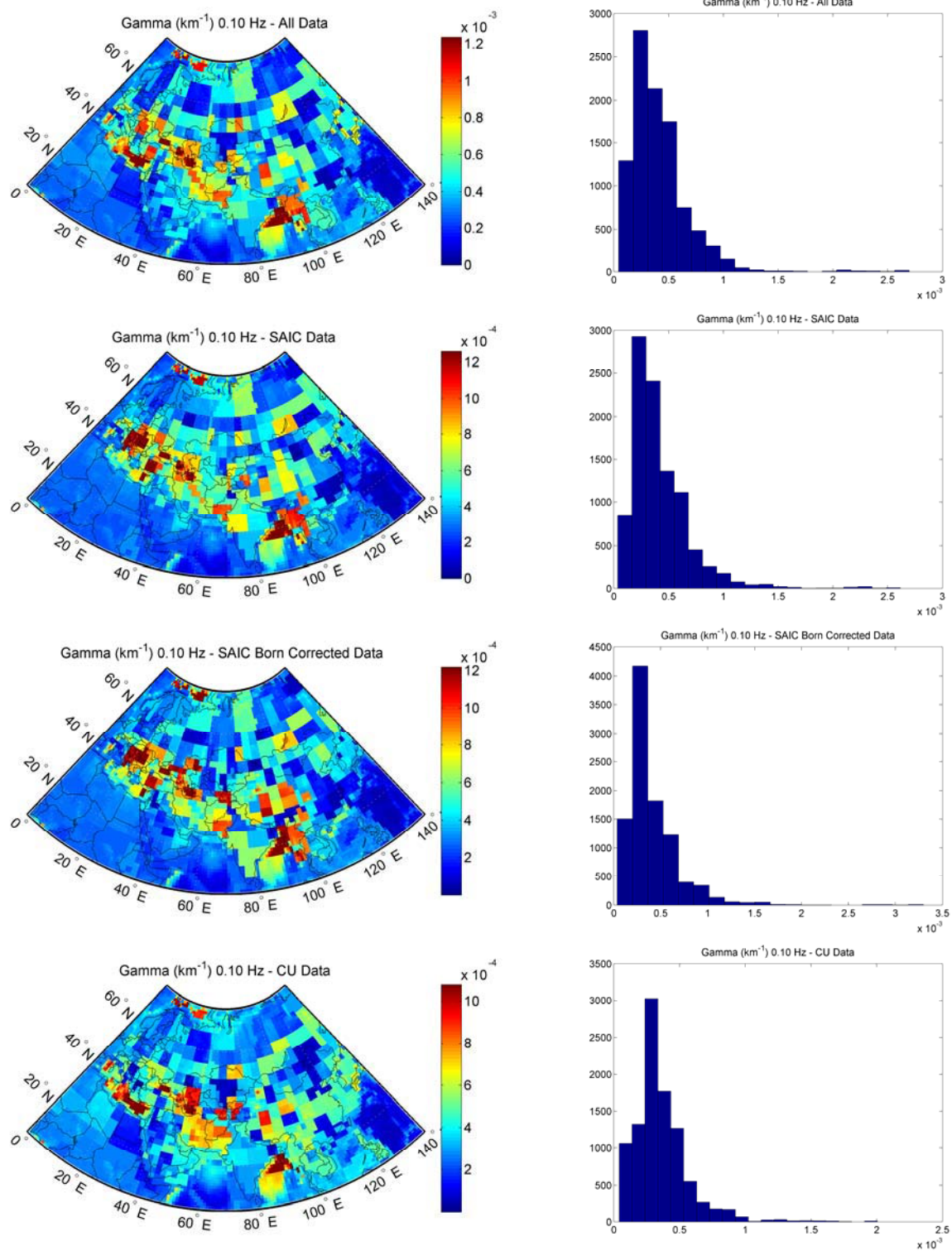


Figure 4.12. Attenuation inversion results at 10 seconds – left: gamma map, right: gamma histogram.

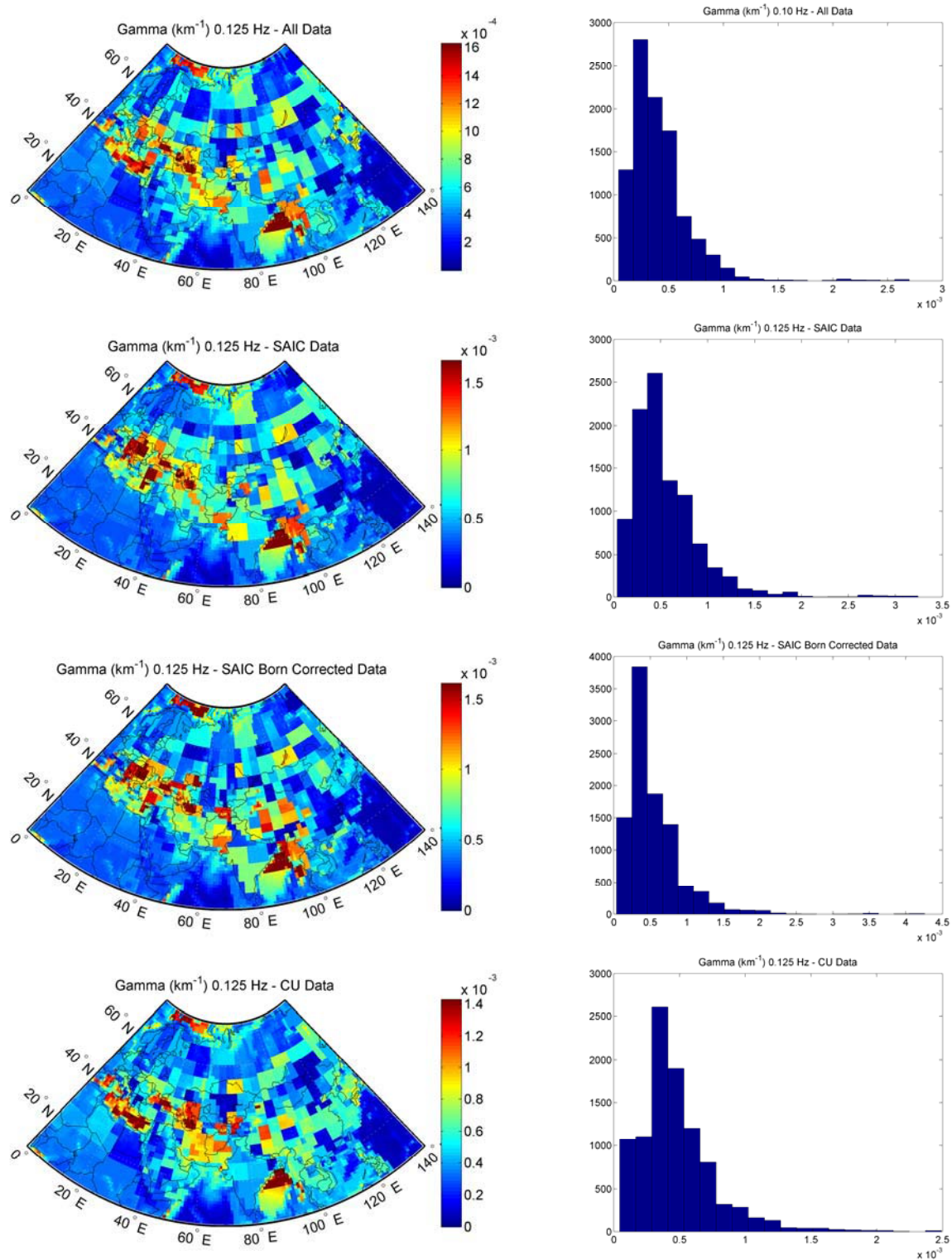


Figure 4.13. Attenuation inversion results at 8 seconds – left: gamma map, right: gamma histogram.

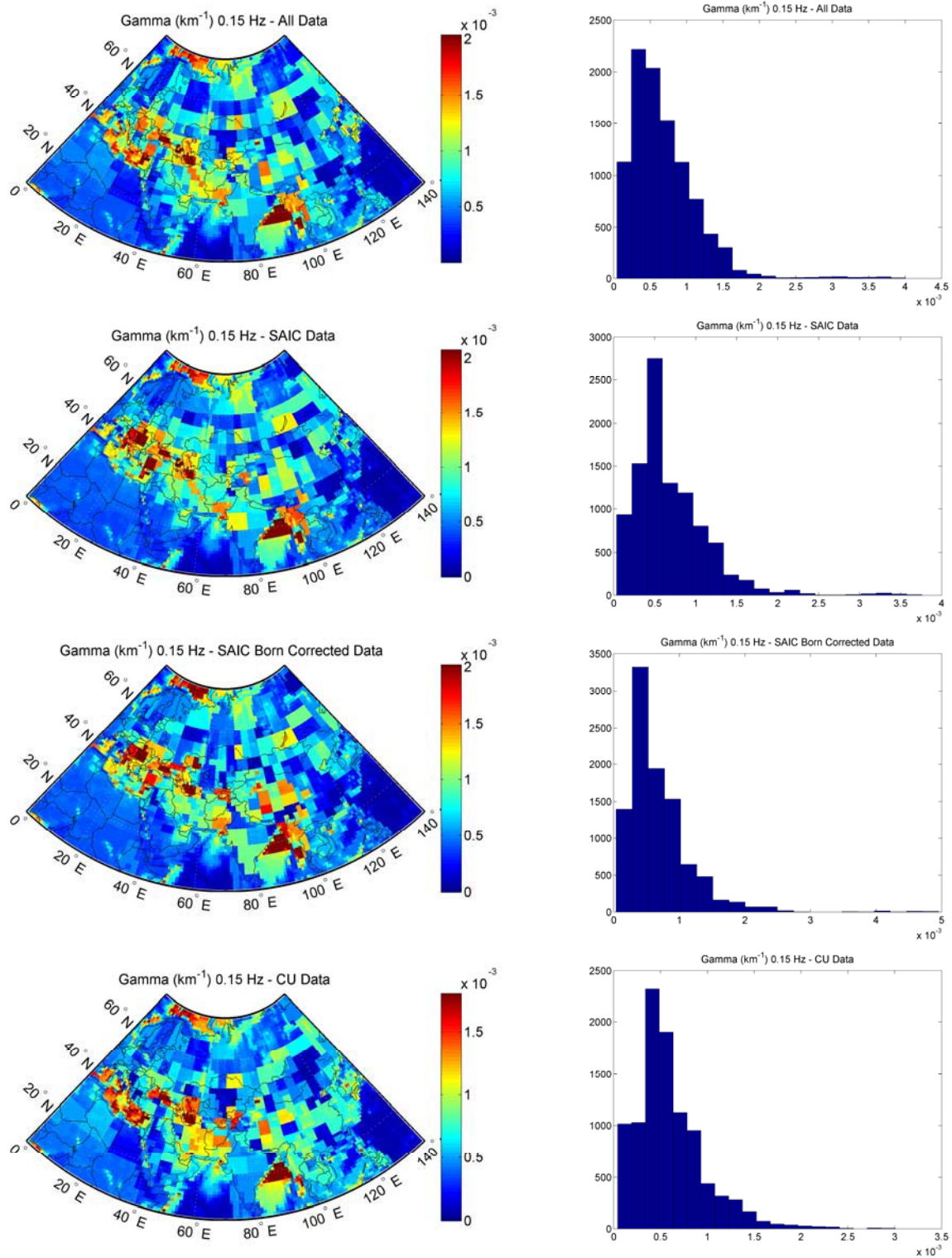


Figure 4.14. Attenuation inversion results at 6.6 seconds – left: gamma map, right: gamma histogram.

## 5.0 Conclusions and Recommendations

We have performed a detailed study of high frequency surface wave amplitudes and attenuation in Eurasia. Following are the major sections of this study with conclusions and recommendations:

1. Regionalized magnitudes – The Russell Butterworth filtered magnitude and the path corrected time and frequency domain magnitudes have a similar purpose, specifically to allow surface waves to be measured at regional and local distances and at higher frequencies than 20 seconds. These magnitudes give similar results when applied to data and are consistent in value with traditional 20 second magnitudes. The path corrected magnitudes have the advantage that they can be regionalized to take into account differences in earth structure and attenuation, while the Butterworth filtered magnitude uses a good representative average value for these quantities. An issue with all of the magnitudes is how to determine which frequency(ies) to measure. The path corrected spectral magnitude, for example, performs a robust average over all frequencies, while the Bonner et al. implementation of the Butterworth filtered magnitude uses the maximum value. Using the maximum value may give better discrimination but at the cost of more variability in the magnitude. More research is needed to determine the optimum procedure.
2. North Korean surface wave magnitude – The North Korean nuclear test had a surprisingly large surface wave magnitude, nearly a magnitude unit higher than would be expected based on larger events assuming a  $M_s$ :log yield slope of one. Some of this difference can be explained by the absence of tectonic release and high velocity source medium for this event. However, the results also suggest that the  $M_s$ :log yield slope may be less than one, which has implications for discrimination of small events as well as yield estimation. More research is needed to analyze surface waves from small events of known yield in high velocity media to see if the North Korean event is an anomaly or the norm.
3. Born approximation – We modeled the effect of heterogeneous structure using the Born approximation. We performed both data analysis and large 3 dimensional finite difference calculations to assess the performance of the Born approximation. Our goal was to use the Born approximation to correct for scattering and diffraction caused by heterogeneous structure prior to performing Q inversions. However, the structural complexity appears to exceed the limits of the Born approximation, and application of the Born corrections do not improve inversion results at these high frequencies. Amplitude variations due to structure at these high frequencies are quite large, so a better way to correct for them is needed.
4. Q inversions – We inverted surface wave amplitude data for attenuation and corrections to source moment for data from about 300 Eurasian earthquakes. We used two data sets: one our own measurements and one set from Anatoli Levshin at the University of Colorado. The data sets are fairly consistent and both indicate higher attenuation than our initial background model. There is a large amount of scatter in both data sets, likely the result of structural variations and interference as discussed above. Nevertheless, there is enough redundancy in the data that we were able to perform Q inversions for the Eurasian continent. The inversions could be significantly improved in two ways: 1) by implementing a better correction for variations due to earth structure; and 2) by

increasing the size of the data set and measuring attenuation from more events. The latter is straightforward, but the former is still troublesome. Ray tracing, for example, is another approach, but the Born approximation reduces to ray tracing in the high frequency limit, and it is subject to similar problems. A multiple scattering Born approximation as suggested by Friederich and Maupin, would be another possibility, but it is not known whether it would lead to better results. Finite difference calculations such as we did in this study are another possibility, but they take considerable computational time and require detailed knowledge of earth structure. The most promising approach is likely to be a hybrid observational/computational method that uses the data together with a numerical or semi-empirical model for surface wave propagation to match observed waveforms.

5. Data and model distribution – The attenuation models developed during this project have been incorporated into the global earth models in the format distributed earlier by Stevens et al. (2005) and are available to all researchers with the permission of AFRL.

## 6.0 Data Deliverable

This report is accompanied by a data deliverable consisting of the following files:

**LP\_2008\_May.tar.gz:** This is the complete set of global earth, dispersion and attenuation models. The contents are described in the file “README.models.” It also contains a program compiled under Linux to calculate the dispersion and attenuation between any two points at an input frequency. The attenuation models are the “All Data” models described above that were derived using both SAIC and University of Colorado attenuation measurements.

**gamma\_data:** These are all of the attenuation measurements made by SAIC during this project. The format of the file is given in the file “dataformat”.

**moments.txt:** This file gives the adjustments to CMT moments found during the Q inversion process as described in Section 4 of this report. The columns correspond to event number, natural log of the correction, and value of the correction.

Note that the data in the “gamma\_data” file are the original measurements derived using CMT moments and so they should be adjusted using the moment corrections by:

$$\Delta\gamma = -\Delta \ln M_0 / r \quad (6.1)$$

This means that if the inversion showed that the moment is larger than the CMT moment then gamma should be reduced for each data point, and if the moment was found to be smaller, then gamma should increase.

## 7.0 Acknowledgment

We thank Anatoli Levshin of the University of Colorado for the use of his data and helpful discussions.

## 8.0 References

- Bennett, Joe, Bob North, Ben Kohl, Jack Murphy, Jeff Stevens, István Bondár, Mark Fisk, Manochehr Bahavar, Brian Barker, Hans Israelsson and Victoria Oancea (2006), "Analysis of IMS Data from the North Korean (DPRK) Nuclear Test of October 9, 2006," SAIC Technical Report prepared for US Army Space and Missile Defense Command (SMDC), December.
- Bonner, J. L., D. R. Russell, D. G. Harkrider, D. T. Reiter, and R. B. Herrmann (2006), "Development of a time-domain, variable period surface-wave magnitude measurement procedure for application at regional and teleseismic distances, part II: application and  $M_s$ - $m_b$  performance," *Bull. Seism. Soc. Am.*, **96**, 678-696, doi: 10.1785/0120050056.
- Dahlen, F. A. and Y. Zhou (2006), "Surface-wave group-delay and attenuation kernels," *Geophys. J. Int.*, **165**, 545-554, doi: 10.1111/j.1365-246X.2006.02913.x.
- Day, S. M., and J. L. Stevens (1986), "An explanation for apparent time delays in phase-reversed Rayleigh waves from underground nuclear explosions," *Geophysical Research Letters*, **13**, pp. 1423-1425.
- Friederich, W., E. Wielandt and S. Stange (1993), "Multiple forward scattering of surface waves: comparison with an exact solution and Born single-scattering methods," *Geophys. J. Int.*, **112**, 264-275.
- Friederich, W. (1999), "Propagation of seismic shear and surface waves in a laterally heterogeneous mantle by multiple forward scattering," *Geophys. J. Int.*, **136**, 180-204.
- Harkrider, D. G., J. L. Stevens, and C. B. Archambeau (1994), "Theoretical Rayleigh and Love waves from an Explosion in Prestressed Source Regions," *Bull. Seism. Soc. Am.*, **84**, 1410-1442.
- Hudson, J. A. and J. R. Heritage (1981), "The use of the Born approximation in seismic scattering problems," *Geophys. J. R. astr. Soc.*, **66**, 221-240.
- Kennett, B. L. N., and K. Yoshizawa (2002), "A reappraisal of regional surface wave tomography," *Geophys. J. Int.* **150**, 37– 44.
- Levshin, A. L., M. P. Barmin, X. Yang, M. Ritzwoller, and G. Randall (2007), "Toward a Rayleigh Wave Attenuation Model for Central Asia and Surrounding Regions," Proceedings of the 29<sup>th</sup> Annual Monitoring Research Review, Denver, CO, 25-27 September 2007.
- Marshall, P. D. and P. W. Basham (1972), "Discrimination Between Earthquakes and Underground Nuclear Explosions Employing an Improved  $M_s$  Scale," *Geophys. J. R. astr. Soc.* **28**, 431-458.
- Maupin, V. (2001), "A multiple-scattering scheme for modeling surface wave propagation in isotropic and anisotropic three-dimensional structures," *Geophys. J. Int.*, **146**, 332-348.
- McGarr, A. (1969), "Amplitude Variations of Rayleigh Waves – Propagation Across A Continental Margin," *Bull. Seism. Soc. Am.*, **59**, 1281-1305.
- Murphy, J. R. (1977), "Seismic Source Functions and Magnitude Determinations for Underground Nuclear Detonations," *Bull. Seism. Soc. Am.*, **67**, 135-158.
- Murphy, J. R. (1996), "Types of Seismic Events and Their Source Descriptions," in *Monitoring a Comprehensive Test Ban Treaty*, ed. E. Husebye and A. Dainty, *Proceedings of the NATO Advanced Study Institute*, Kluwer Academic Publishers, 225-245.

- Nolet, G. (1987), "Seismic Wave Propagation and Seismic Tomography," in *Seismic Tomography with Applications In Global Seismology and Exploration Geophysics*, G. Nolet, ed., D. Reidel Publishing, Dordrecht, Holland.
- Rezapour, M. and R. G. Pearce (1998), "Bias in Surface-Wave Magnitude  $M_s$  due to Inadequate Distance Corrections," *Bull. Seism. Soc. Am.*, **88**, 43-61.
- Ritzwoller, M. H., N. M. Shapiro, M. P. Barmin, and A. L. Levshin (2002), "Global surface wave diffraction tomography," *J. Geophys. Res.*, **107**, 2335, doi:10.1029/2002JB001777.
- Russell, D. R. (2006), "Development of a time-domain, variable period surface-wave magnitude measurement procedure for application at regional and teleseismic distances, part I: theory," *Bull. Seism. Soc. Am.*, **96**, 665-677, doi: 10.1785/0120050055.
- Snieder, R. (1986), "3-D linearized scattering of surface waves and a formalism for surface wave holography," *Geophys. J. R. astr. Soc.*, **84**, 581-605.
- Spetzler, J., J. Trampert and R. Snieder (2001), "The effect of small-scale heterogeneity on the arrival time of waves," *Geophys. J. Int.*, **145**, 786-796.
- Spetzler, J., J. Trampert and R. Snieder (2002), "The effect of scattering in surface wave tomography," *Geophys. J. Int.*, **149**, 755-767.
- Stevens, J. L. and S. M. Day (1985), "The physical basis of the  $m_b$ : $M_s$  and variable frequency magnitude methods for earthquake/explosion discrimination," *J. Geophys. Res.*, **90**, 3009-3020.
- Stevens, J. L. and K. L. McLaughlin (1996), "Regionalized Maximum Likelihood Surface Wave Analysis," Maxwell Technologies Technical Report submitted to Phillips Laboratory, PL-TR-96-2273, SSS-DTR-96-15562, September.
- Stevens, J. L. and K. L. McLaughlin (2001), "Optimization of Surface Wave Identification and Measurement," *Pure and Applied Geophysics*, **158**, 1547-1582.
- Stevens, J. L. and J. R. Murphy (2001), "Yield Estimation from surface wave amplitudes," *Pure and Applied Geophysics*, **158**, 2227-2251.
- Stevens, J. L., D. A. Adams, G. E. Baker, M. G. Eneva and H. Xu (2005), "Improved Surface Wave Dispersion Models, Amplitude Measurements and Azimuth Estimates," SAIC Final Report submitted to AFRL under contract DTRA01-01-C-0082, March.
- Stevens, Jeffrey L., Jeffrey W. Given, G. Eli Baker and Heming Xu (2006), "Development of Surface Wave Dispersion and Attenuation Maps and Improved Methods for Measuring Surface Waves," Proceedings of the 28th Annual Seismic Research Review, Orlando, FL, 19-21 September 2006.
- Stevens, Jeffrey L., Jeffrey W. Given, Heming Xu, and G. Eli Baker (2007), "Development of Surface Wave Dispersion and Attenuation Maps and Improved Methods for Measuring Surface Waves," Proceedings of the 29<sup>th</sup> Annual Monitoring Research Review, Denver, CO, 25-27 September 2007.
- von Seggern, D. H. (1977), "Amplitude-distance relation for 20-second Rayleigh waves," *Bull. Seism. Soc. Am.* **67**, 405-411.
- Yoshizawa, K., and B. L. N. Kennett (2004), "Multimode surface wave tomography for the Australian region using a three-stage approach incorporating finite frequency effects," *J. Geophys. Res.*, **109**, B02310, doi:10.1029/2002JB002254.
- Zhou, Y., F. A. Dahlen and G. Nolet (2004), "Three-dimensional sensitivity kernels for surface wave observables," *Geophys. J. Int.*, **158**, 142-168.

## Appendix A. Events processed for Q inversion

The following table lists the events that were processed at SAIC for Q inversion. Evid is a sequence number, Date/Time the date and time of the event, Lat, Lon and depth the event hypocenter, Moment is the CMT moment and Rtime the rise time of a triangular source function, also from the CMT catalog.  $m_b$  and  $M_s$  are body and surface wave magnitude and Nsta is the number of stations processed for the event.

**Table A1. List of events processed for Q inversion.**

| EVID | Date/Time           | Lat   | Lon    | Depth | Moment   | Rtime | $m_b$ | $M_s$ | Nsta |
|------|---------------------|-------|--------|-------|----------|-------|-------|-------|------|
| 1    | 1994/01/11 00:51:59 | 25.23 | 97.20  | 33    | 1.60E+18 | 2.7   | 5.9   | 5.9   | 14   |
| 2    | 1994/02/23 08:02:05 | 30.85 | 60.60  | 10    | 1.72E+18 | 2.9   | 6.0   | 6.1   | 15   |
| 3    | 1994/02/24 00:11:12 | 30.78 | 60.50  | 13    | 3.30E+18 | 3.7   | 6.0   | 6.1   | 12   |
| 4    | 1994/02/26 02:31:11 | 30.90 | 60.55  | 12    | 1.39E+18 | 2.5   | 5.8   | 5.9   | 16   |
| 5    | 1994/03/01 03:49:01 | 29.10 | 52.62  | 17    | 1.37E+18 | 2.8   | 5.8   | 6.0   | 13   |
| 6    | 1994/04/06 07:03:27 | 26.19 | 96.87  | 33    | 7.15E+17 | 2.0   | 5.6   | 5.6   | 19   |
| 7    | 1994/04/13 04:00:51 | 22.78 | 123.63 | 36    | 5.76E+17 | 2.1   | 5.7   | 5.6   | 5    |
| 8    | 1994/05/01 12:00:37 | 36.90 | 67.16  | 26    | 1.65E+18 | 2.6   | 5.9   | 6.3   | 14   |
| 9    | 1994/05/23 05:36:03 | 24.17 | 122.54 | 34    | 1.89E+18 | 2.9   | 5.7   | 6.0   | 10   |
| 10   | 1994/05/23 15:16:58 | 24.07 | 122.56 | 33    | 8.13E+17 | 2.2   | 5.9   | 5.7   | 11   |
| 11   | 1994/05/24 04:00:46 | 23.96 | 122.45 | 47    | 6.60E+18 | 4.2   | 6.0   | 6.6   | 9    |
| 12   | 1994/05/29 14:11:51 | 20.56 | 94.16  | 42    | 6.50E+18 | 4.4   | 6.2   | 6.2   | 6    |
| 13   | 1994/06/05 01:09:31 | 24.51 | 121.91 | 16    | 3.80E+18 | 3.8   | 6.0   | 6.5   | 9    |
| 14   | 1994/06/20 09:09:04 | 28.97 | 52.61  | 17    | 8.05E+17 | 2.1   | 5.9   | 5.7   | 7    |
| 15   | 1994/06/29 18:22:36 | 32.57 | 93.67  | 33    | 7.72E+17 | 2.2   | 5.8   | 5.5   | 14   |
| 16   | 1994/08/19 21:02:45 | 17.97 | 96.42  | 12    | 4.81E+17 | 1.8   | 5.5   | 5.6   | 9    |
| 17   | 1994/08/21 15:56:01 | 56.76 | 117.90 | 33    | 1.25E+18 | 2.6   | 5.7   | 5.8   | 19   |
| 18   | 1994/09/16 06:20:18 | 22.55 | 118.74 | 12    | 1.25E+19 | 5.4   | 6.5   | 6.7   | 12   |
| 19   | 1994/11/21 08:16:36 | 25.49 | 96.70  | 33    | 9.25E+17 | 2.4   | 5.6   | 5.9   | 11   |
| 20   | 1995/02/23 21:03:02 | 35.05 | 32.28  | 15    | 8.06E+17 | 2.0   | 5.8   | 5.7   | 19   |
| 21   | 1995/02/23 05:19:02 | 24.14 | 121.61 | 44    | 2.45E+18 | 3.5   | 5.8   | 6.2   | 11   |
| 22   | 1995/05/13 08:47:12 | 40.15 | 21.70  | 13    | 7.64E+18 | 4.3   | 6.2   | 6.5   | 18   |
| 23   | 1995/06/15 00:15:48 | 38.40 | 22.28  | 14    | 6.01E+18 | 4.3   | 6.0   | 6.5   | 12   |
| 24   | 1995/06/25 06:59:05 | 24.60 | 121.71 | 47    | 1.02E+18 | 2.4   | 5.8   | 5.7   | 14   |
| 25   | 1995/06/29 23:02:31 | 51.96 | 103.10 | 33    | 5.20E+17 | 1.8   | 5.6   | 5.5   | 30   |
| 26   | 1995/07/09 20:31:31 | 21.98 | 99.16  | 12    | 7.53E+17 | 2.1   | 5.7   | 5.9   | 11   |
| 27   | 1995/07/11 21:46:39 | 21.97 | 99.20  | 13    | 1.91E+19 | 6.6   | 6.1   | 7.2   | 15   |
| 28   | 1995/10/01 15:57:16 | 38.06 | 30.13  | 33    | 4.72E+18 | 4.0   | 5.7   | 6.1   | 11   |
| 29   | 1995/10/23 22:46:50 | 26.00 | 102.23 | 0     | 2.18E+18 | 3.3   | 5.5   | 0.0   | 17   |
| 30   | 1995/11/13 08:43:14 | 56.10 | 114.50 | 24    | 5.50E+17 | 1.8   | 5.9   | 5.6   | 30   |
| 31   | 1995/11/22 04:15:11 | 28.83 | 34.80  | 10    | 7.21E+19 | 11.0  | 6.2   | 7.3   | 23   |
| 32   | 1995/12/05 18:49:33 | 39.44 | 40.15  | 29.3  | 5.54E+17 | 2.0   | 4.9   | 0.0   | 19   |
| 33   | 1996/02/03 11:14:19 | 27.29 | 100.28 | 10    | 9.94E+18 | 5.2   | 6.3   | 6.5   | 14   |
| 34   | 1996/03/05 14:52:28 | 24.09 | 122.22 | 30    | 3.59E+18 | 3.9   | 6.1   | 6.4   | 17   |
| 35   | 1996/03/05 17:32:10 | 24.03 | 122.24 | 33    | 7.33E+17 | 2.3   | 5.6   | 5.6   | 14   |
| 36   | 1996/03/19 15:00:26 | 39.99 | 76.70  | 28    | 3.60E+18 | 3.9   | 5.7   | 6.0   | 24   |
| 37   | 1996/03/29 03:28:56 | 24.14 | 122.20 | 33    | 5.20E+17 | 1.8   | 5.4   | 5.5   | 14   |
| 38   | 1996/05/03 03:32:47 | 40.77 | 109.66 | 26    | 1.07E+18 | 2.6   | 5.5   | 6.0   | 12   |
| 39   | 1996/06/22 16:47:12 | 75.82 | 134.62 | 10    | 4.95E+17 | 1.6   | 5.6   | 5.5   | 20   |
| 40   | 1996/07/20 00:00:41 | 36.15 | 27.10  | 33    | 2.38E+18 | 3.0   | 5.7   | 6.2   | 13   |
| 41   | 1996/08/14 02:59:41 | 40.75 | 35.34  | 10    | 3.54E+17 | 1.6   | 5.2   | 5.5   | 13   |
| 42   | 1996/09/05 23:42:06 | 21.90 | 121.50 | 20    | 1.91E+19 | 6.4   | 6.4   | 6.6   | 11   |

|    |                     |       |        |      |          |      |     |     |    |
|----|---------------------|-------|--------|------|----------|------|-----|-----|----|
| 43 | 1996/10/09 13:10:52 | 34.56 | 32.13  | 33   | 1.85E+19 | 6.9  | 6.4 | 6.8 | 12 |
| 44 | 1996/11/19 10:44:46 | 35.35 | 78.13  | 33   | 2.37E+19 | 6.9  | 6.1 | 7.1 | 26 |
| 45 | 1996/11/20 18:09:19 | 39.60 | 96.68  | 33   | 5.13E+17 | 1.9  | 5.0 | 0.0 | 2  |
| 46 | 1997/01/09 13:43:31 | 41.03 | 74.28  | 22   | 5.66E+17 | 1.9  | 5.7 | 5.8 | 40 |
| 47 | 1997/01/21 01:48:30 | 39.47 | 77.00  | 33   | 7.74E+17 | 2.1  | 5.3 | 5.8 | 25 |
| 48 | 1997/02/04 10:37:47 | 37.66 | 57.29  | 10   | 6.72E+18 | 4.5  | 5.9 | 6.8 | 29 |
| 49 | 1997/02/27 21:08:02 | 29.98 | 68.21  | 33   | 5.20E+19 | 7.9  | 6.3 | 7.3 | 9  |
| 50 | 1997/02/28 12:57:18 | 38.08 | 48.05  | 10   | 1.73E+18 | 2.8  | 5.5 | 6.1 | 18 |
| 51 | 1997/03/20 08:50:40 | 30.14 | 68.02  | 33   | 8.09E+17 | 2.0  | 5.5 | 5.8 | 34 |
| 52 | 1997/04/05 23:46:19 | 39.51 | 76.87  | 33   | 7.73E+17 | 2.2  | 5.4 | 5.9 | 28 |
| 53 | 1997/04/06 04:36:35 | 39.54 | 77.00  | 33   | 1.05E+18 | 2.3  | 5.6 | 5.8 | 35 |
| 54 | 1997/04/11 05:34:42 | 39.53 | 76.94  | 15   | 2.06E+18 | 3.0  | 5.8 | 6.1 | 35 |
| 55 | 1997/04/15 18:19:10 | 39.63 | 76.99  | 23   | 6.56E+17 | 2.2  | 5.4 | 5.8 | 28 |
| 56 | 1997/05/08 02:53:14 | 24.89 | 92.25  | 35   | 8.57E+17 | 2.3  | 5.6 | 5.6 | 18 |
| 57 | 1997/05/10 07:57:29 | 33.83 | 59.81  | 10   | 7.35E+19 | 1.0  | 6.4 | 7.3 | 24 |
| 58 | 1997/05/21 22:51:28 | 23.08 | 80.04  | 36   | 5.83E+17 | 1.9  | 6.0 | 5.6 | 28 |
| 59 | 1997/06/25 19:38:40 | 33.94 | 59.48  | 10   | 7.40E+17 | 2.2  | 5.5 | 5.8 | 29 |
| 60 | 1997/11/08 10:02:52 | 35.07 | 87.33  | 33   | 2.23E+20 | 14.7 | 6.2 | 7.9 | 43 |
| 61 | 1997/12/30 13:43:18 | 25.38 | 96.61  | 33   | 5.14E+17 | 1.9  | 5.4 | 5.7 | 18 |
| 62 | 1998/01/10 03:50:41 | 41.08 | 114.50 | 30.3 | 4.48E+17 | 1.8  | 5.8 | 5.7 | 29 |
| 63 | 1998/02/04 14:33:21 | 37.08 | 70.09  | 33   | 8.36E+17 | 2.3  | 5.6 | 6.1 | 38 |
| 64 | 1998/03/14 19:40:27 | 30.15 | 57.61  | 9    | 9.43E+18 | 5.0  | 5.9 | 6.9 | 26 |
| 65 | 1998/04/10 15:00:53 | 32.46 | 59.98  | 33   | 5.01E+17 | 1.9  | 5.3 | 5.7 | 38 |
| 66 | 1998/05/03 23:30:21 | 22.31 | 125.31 | 33   | 1.83E+20 | 14.1 | 6.4 | 7.3 | 14 |
| 67 | 1998/05/30 06:22:29 | 37.11 | 70.11  | 33   | 7.89E+18 | 5.0  | 5.9 | 6.9 | 34 |
| 68 | 1998/06/27 13:55:52 | 36.88 | 35.31  | 33   | 2.96E+18 | 3.5  | 5.8 | 6.2 | 34 |
| 69 | 1998/07/20 01:05:58 | 30.13 | 88.17  | 33.2 | 4.77E+17 | 1.8  | 5.4 | 5.4 | 62 |
| 70 | 1998/07/24 18:44:04 | 21.25 | 122.02 | 33   | 1.73E+18 | 2.9  | 5.6 | 5.9 | 23 |
| 71 | 1998/08/25 07:41:40 | 30.08 | 88.11  | 33   | 6.81E+17 | 1.9  | 5.3 | 5.5 | 51 |
| 72 | 1998/08/27 09:03:36 | 39.66 | 77.34  | 33   | 3.89E+18 | 3.9  | 5.6 | 6.4 | 42 |
| 73 | 1998/11/19 15:39:19 | 22.61 | 125.78 | 10   | 3.27E+18 | 3.6  | 5.8 | 6.0 | 15 |
| 74 | 1999/02/11 14:08:51 | 34.26 | 69.36  | 33   | 1.27E+18 | 2.6  | 5.4 | 5.8 | 41 |
| 75 | 1999/02/22 13:49:00 | 24.12 | 122.65 | 42.7 | 8.05E+17 | 2.3  | 5.4 | 5.6 | 27 |
| 76 | 1999/02/25 18:58:29 | 51.60 | 104.86 | 10   | 8.91E+17 | 2.2  | 5.9 | 5.5 | 30 |
| 77 | 1999/03/04 05:38:26 | 28.34 | 57.19  | 33   | 1.01E+19 | 5.5  | 6.2 | 6.5 | 38 |
| 78 | 1999/03/21 16:16:02 | 55.90 | 110.21 | 10   | 8.50E+17 | 2.1  | 5.5 | 5.7 | 39 |
| 79 | 1999/03/28 19:05:11 | 30.51 | 79.40  | 15   | 7.77E+18 | 4.7  | 6.4 | 6.6 | 52 |
| 80 | 1999/05/06 23:00:53 | 29.50 | 51.88  | 33   | 2.47E+18 | 3.5  | 5.9 | 6.3 | 24 |
| 81 | 1999/08/17 00:01:39 | 40.75 | 29.86  | 17   | 2.88E+20 | 20.7 | 6.3 | 7.8 | 18 |
| 82 | 1999/09/07 11:56:49 | 38.12 | 23.61  | 10   | 1.14E+18 | 2.6  | 5.6 | 5.8 | 12 |
| 83 | 1999/09/13 11:55:28 | 40.71 | 30.05  | 13   | 5.96E+17 | 2.0  | 5.8 | 5.8 | 42 |
| 84 | 1999/09/20 17:47:18 | 23.77 | 120.98 | 33   | 3.38E+20 | 19.9 | 6.5 | 7.7 | 40 |
| 85 | 1999/09/20 21:46:42 | 23.39 | 120.96 | 33   | 4.83E+18 | 4.0  | 5.8 | 6.5 | 37 |
| 86 | 1999/09/22 00:14:39 | 23.73 | 121.17 | 26   | 5.03E+18 | 4.0  | 6.2 | 6.4 | 48 |
| 87 | 1999/09/22 00:49:42 | 23.64 | 121.14 | 33   | 6.31E+17 | 2.0  | 5.9 | 5.9 | 38 |
| 88 | 1999/09/25 23:52:48 | 23.74 | 121.16 | 17   | 6.01E+18 | 4.2  | 6.2 | 6.4 | 38 |
| 89 | 1999/10/22 02:18:58 | 23.45 | 120.51 | 33   | 6.95E+17 | 2.1  | 5.7 | 5.6 | 39 |
| 90 | 1999/11/01 17:53:00 | 23.38 | 121.52 | 33   | 3.29E+18 | 3.6  | 6.1 | 6.1 | 49 |
| 91 | 1999/11/12 16:57:19 | 40.76 | 31.16  | 10   | 6.65E+19 | 10.5 | 6.3 | 7.5 | 17 |
| 92 | 1999/12/03 17:06:54 | 40.36 | 42.35  | 19.3 | 3.97E+17 | 1.6  | 5.3 | 5.5 | 24 |
| 93 | 2000/01/14 23:37:07 | 25.61 | 101.06 | 33   | 8.33E+17 | 2.3  | 5.4 | 5.9 | 54 |
| 94 | 2000/01/28 14:21:07 | 43.05 | 146.84 | 61.1 | 1.98E+19 | 6.4  | 6.7 | 6.6 | 28 |

|     |                     |       |        |      |          |      |     |     |    |
|-----|---------------------|-------|--------|------|----------|------|-----|-----|----|
| 95  | 2000/06/06 02:41:49 | 40.69 | 32.99  | 10   | 1.11E+18 | 2.7  | 5.5 | 6.1 | 31 |
| 96  | 2000/06/07 21:46:55 | 26.86 | 97.24  | 33   | 3.74E+18 | 3.7  | 6.3 | 6.5 | 50 |
| 97  | 2000/06/10 18:23:29 | 23.84 | 121.23 | 33   | 5.35E+18 | 4.3  | 6.2 | 6.2 | 32 |
| 98  | 2000/08/04 21:13:02 | 48.79 | 142.25 | 10   | 1.92E+19 | 6.4  | 6.3 | 7.1 | 31 |
| 99  | 2000/08/22 16:55:13 | 38.12 | 57.38  | 10   | 3.62E+17 | 1.7  | 5.2 | 5.8 | 56 |
| 100 | 2000/09/10 08:54:46 | 24.01 | 121.53 | 34.8 | 5.83E+17 | 2.0  | 5.6 | 5.6 | 45 |
| 101 | 2000/09/12 00:27:58 | 35.39 | 99.34  | 10   | 1.76E+18 | 3.1  | 5.7 | 6.3 | 71 |
| 102 | 2000/10/09 02:30:00 | 10.00 | 92.95  | 33   | 3.57E+17 | 2.0  | 5.3 | 5.6 | 32 |
| 103 | 2000/12/06 17:11:06 | 39.57 | 54.80  | 30   | 3.90E+19 | 8.8  | 6.7 | 7.5 | 65 |
| 104 | 2000/12/15 16:44:47 | 38.46 | 31.35  | 10   | 1.21E+18 | 2.7  | 5.1 | 5.8 | 28 |
| 105 | 2001/01/03 14:47:49 | 43.93 | 147.81 | 33   | 7.66E+17 | 2.1  | 5.9 | 5.2 | 20 |
| 106 | 2001/01/26 03:16:40 | 23.42 | 70.23  | 16   | 3.43E+20 | 24.1 | 6.9 | 8.0 | 53 |
| 107 | 2001/01/28 01:02:10 | 23.51 | 70.52  | 10   | 5.22E+17 | 2.0  | 5.9 | 5.5 | 47 |
| 108 | 2001/03/05 15:50:07 | 34.37 | 86.90  | 33   | 8.64E+17 | 2.1  | 5.4 | 5.8 | 60 |
| 109 | 2001/03/15 01:22:43 | 8.66  | 94.01  | 33   | 1.04E+18 | 2.3  | 5.6 | 5.9 | 32 |
| 110 | 2001/03/24 06:27:53 | 34.08 | 132.53 | 50   | 1.97E+19 | 6.2  | 6.4 | 6.5 | 33 |
| 111 | 2001/06/10 01:52:08 | 39.84 | 53.89  | 34.1 | 1.49E+17 | 1.2  | 5.5 | 5.2 | 29 |
| 112 | 2001/06/14 02:35:25 | 24.51 | 122.03 | 32.1 | 7.80E+17 | 2.2  | 5.7 | 5.6 | 30 |
| 113 | 2001/06/25 13:28:46 | 37.20 | 36.17  | 5    | 1.68E+17 | 1.1  | 5.2 | 4.9 | 2  |
| 114 | 2001/07/26 00:21:36 | 39.06 | 24.34  | 10   | 5.61E+18 | 4.0  | 6.0 | 6.6 | 25 |
| 115 | 2001/11/14 09:26:10 | 35.95 | 90.54  | 10   | 5.90E+20 | 25.8 | 6.1 | 8.0 | 32 |
| 116 | 2001/12/18 04:02:58 | 23.95 | 122.73 | 14   | 2.08E+19 | 7.1  | 6.3 | 7.3 | 47 |
| 117 | 2002/02/03 07:11:28 | 38.57 | 31.27  | 5    | 6.00E+18 | 4.4  | 5.7 | 6.4 | 45 |
| 118 | 2002/02/03 09:26:43 | 38.63 | 30.90  | 10   | 6.11E+17 | 1.7  | 5.7 | 5.6 | 32 |
| 119 | 2002/02/12 03:27:25 | 23.70 | 121.57 | 54.8 | 3.79E+17 | 1.8  | 5.8 | 5.4 | 29 |
| 120 | 2002/02/17 13:03:52 | 28.11 | 51.76  | 33   | 1.16E+17 | 1.1  | 5.6 | 5.0 | 19 |
| 121 | 2002/03/25 14:56:33 | 35.97 | 69.17  | 8    | 1.62E+18 | 3.4  | 5.9 | 6.2 | 23 |
| 122 | 2002/03/27 08:52:52 | 35.92 | 69.28  | 10   | 2.83E+17 | 1.5  | 5.9 | 5.4 | 20 |
| 123 | 2002/03/31 06:52:50 | 24.41 | 122.21 | 32.8 | 5.45E+19 | 10.1 | 6.4 | 7.4 | 34 |
| 124 | 2002/04/12 04:00:23 | 35.96 | 69.42  | 10   | 7.24E+17 | 2.4  | 5.8 | 5.9 | 52 |
| 125 | 2002/04/17 08:47:22 | 27.61 | 56.76  | 33   | 9.11E+16 | 1.0  | 5.3 | 4.9 | 10 |
| 126 | 2002/04/24 10:51:50 | 42.43 | 21.51  | 10   | 4.50E+17 | 1.9  | 5.6 | 5.6 | 4  |
| 127 | 2002/05/15 03:46:05 | 24.64 | 121.92 | 10   | 1.91E+18 | 3.0  | 5.5 | 6.2 | 15 |
| 128 | 2002/05/28 16:45:17 | 24.07 | 122.26 | 33   | 1.49E+18 | 2.5  | 5.8 | 5.9 | 15 |
| 129 | 2002/06/04 14:36:05 | 30.54 | 81.44  | 33   | 2.99E+17 | 1.6  | 5.4 | 5.3 | 22 |
| 130 | 2002/06/22 02:58:21 | 35.63 | 49.05  | 10   | 6.97E+18 | 4.6  | 6.2 | 6.4 | 26 |
| 131 | 2002/07/11 07:36:26 | 24.08 | 122.29 | 43.8 | 6.52E+17 | 2.1  | 5.6 | 5.6 | 36 |
| 132 | 2002/07/13 20:06:27 | 30.80 | 69.98  | 33   | 4.78E+17 | 1.9  | 5.4 | 5.7 | 67 |
| 133 | 2002/08/08 11:42:05 | 30.99 | 99.90  | 33   | 9.60E+16 | 1.0  | 5.4 | 4.7 | 15 |
| 134 | 2002/09/06 01:21:28 | 38.38 | 13.70  | 5    | 9.69E+17 | 2.3  | 5.8 | 5.5 | 13 |
| 135 | 2002/09/13 22:28:29 | 13.04 | 93.07  | 21   | 6.35E+18 | 4.5  | 6.2 | 6.7 | 37 |
| 136 | 2002/09/14 19:58:37 | 13.06 | 93.16  | 33   | 4.70E+17 | 1.8  | 5.7 | 5.6 | 33 |
| 137 | 2002/09/25 22:28:11 | 32.09 | 49.23  | 10   | 3.02E+17 | 1.6  | 5.5 | 5.1 | 8  |
| 138 | 2002/11/20 21:32:30 | 35.41 | 74.52  | 33   | 3.54E+18 | 3.5  | 5.7 | 6.5 | 49 |
| 139 | 2002/12/04 11:30:53 | 19.40 | 94.48  | 53.5 | 2.66E+17 | 1.5  | 5.6 | 0.0 | 11 |
| 140 | 2002/12/14 13:27:29 | 39.73 | 97.42  | 22   | 2.31E+17 | 1.5  | 5.6 | 5.3 | 11 |
| 141 | 2002/12/25 12:57:03 | 39.70 | 75.18  | 10   | 3.51E+17 | 1.6  | 5.5 | 5.6 | 24 |
| 142 | 2007/01/08 17:21:49 | 39.80 | 70.31  | 14   | 1.33E+18 | 2.5  | 5.9 | 5.9 | 33 |
| 143 | 2007/01/25 10:59:17 | 22.56 | 121.93 | 36.2 | 1.35E+18 | 2.5  | 5.6 | 6.0 | 21 |
| 144 | 2007/02/02 22:32:18 | 37.71 | 91.81  | 10   | 1.45E+17 | 1.2  | 5.3 | 5.3 | 29 |
| 145 | 2007/02/21 11:05:29 | 38.43 | 39.24  | 10   | 4.65E+17 | 1.8  | 5.7 | 5.7 | 20 |
| 146 | 2007/04/10 13:56:53 | 13.00 | 92.60  | 30   | 1.97E+17 | 1.3  | 5.5 | 5.4 | 16 |

|     |                     |       |        |      |          |     |     |     |    |
|-----|---------------------|-------|--------|------|----------|-----|-----|-----|----|
| 147 | 2007/05/05 08:51:39 | 34.25 | 81.97  | 9    | 1.54E+18 | 2.6 | 5.8 | 6.0 | 4  |
| 148 | 2007/06/02 21:34:58 | 23.03 | 101.02 | 10   | 1.64E+18 | 2.7 | 6.2 | 6.2 | 19 |
| 149 | 2007/06/18 14:29:49 | 34.48 | 50.84  | 10   | 2.36E+17 | 1.4 | 5.5 | 5.5 | 29 |
| 150 | 2007/07/04 01:23:24 | 55.50 | 110.22 | 10   | 1.39E+17 | 1.2 | 5.3 | 5.3 | 12 |
| 151 | 2007/07/20 10:06:52 | 42.93 | 82.31  | 11.8 | 2.76E+17 | 1.5 | 5.5 | 5.5 | 18 |
| 152 | 2007/07/23 13:40:02 | 23.64 | 121.57 | 40.6 | 9.14E+16 | 1.0 | 5.6 | 4.9 | 25 |
| 153 | 2007/07/30 22:42:05 | 19.31 | 95.56  | 14.2 | 3.04E+17 | 1.5 | 6.0 | 5.6 | 8  |
| 154 | 2007/07/31 15:07:35 | 27.31 | 126.83 | 10   | 8.41E+17 | 2.1 | 5.5 | 5.9 | 8  |
| 155 | 2007/08/02 02:37:42 | 47.12 | 141.80 | 5    | 2.35E+18 | 3.0 | 5.3 | 6.2 | 29 |
| 156 | 2007/08/02 05:22:17 | 46.71 | 141.75 | 10   | 5.42E+17 | 1.8 | 5.6 | 5.8 | 23 |
| 157 | 2007/08/29 03:00:18 | 21.73 | 121.37 | 24.5 | 1.72E+17 | 1.3 | 5.7 | 5.5 | 10 |
| 158 | 2007/09/06 17:51:27 | 24.33 | 122.32 | 62.9 | 2.93E+18 | 3.2 | 6.5 | 6.5 | 16 |